Atomic Coherence based Electromagnetic Wave Interferometry

A
Thesis Submitted
in Partial Fulfillment of the Requirements
for the Degree of
DOCTOR OF PHILOSOPHY
By

DANGKA SHYLLA
Under the Supervision of
Dr. KANHAIYA PANDEY

Department of Physics
Indian Institute of Technology Guwahati
October, 2022

DEDICATION

To my grandmother

Declaration

This is to certify that the thesis entitled "**Atomic Coherence based Electromagnetic Wave Interferometry**", submitted by me to the *Indian Institute of Technology Guwahati*, for the award of the degree of Doctor of Philosophy, is a bonafide work carried out by me under the supervision of Dr. Kanhaiya Pandey. The content of this thesis, in full or in parts, have not been submitted to any other University or Institute for the award of any degree or diploma. I also wish to state that to the best of my knowledge and understanding nothing in this report amounts to plagiarism.

Dangka Shylla
Roll no.: 166121009
Department of Physics,
Indian Institute of Technology Guwahati,
Guwahati-781039, Assam, India.

Certificate

This is to certify that the thesis entitled "**Atomic Coherence based Electromagnetic Wave Interferometry**", submitted by Dangka Shylla (166121009), a Ph.D in the *Department of Physics*, *Indian Institute of Technology Guwahati*, for the award of the degree of Doctor of Philosophy, is a record of an original research work carried out by him under my supervision and guidance. The thesis has fulfilled all requirements as per the regulations of the institute and in my opinion has reached the standard needed for submission. The results embodied in this thesis have not been submitted to any other University or Institute for the award of any degree or diploma.

Supervisor: Dr. Kanhaiya Pandey
Department of Physics,
Indian Institute of Technology Guwahati,
Guwahati-781039, Assam, India.

Acknowledgements

Firstly, I would like to express my deepest gratitude to my advisor and research supervisor, Dr. Kanhaiya Pandey, for his unwavering support, invaluable guidance, and constant encouragement throughout my PhD journey. His dynamism, vision, patience, inspiration, and vast knowledge have been of tremendous help to me in conducting my research and writing this thesis. I am truly grateful to have had such an exceptional mentor and advisor.

I am also indebted to the members of my Doctoral Committee, Prof Bosanta Ranjan Boruah, Dr Gagan Kumar, and Dr. Ramesh Kumar Sonkar, for their critical input, insightful comments, and constant support in presenting my work. I am grateful to all the professors in the Department of Physics as well as Prof Anugrah Singh from the Department of Chemical Engineering for their support during my research work period. Additionally, I would like to acknowledge the late Prof Vasant Natarajan from IISc Bangalore for his generous support, which made this endeavour possible.I am grateful to the Indian Institute of Technology Guwahati for providing the PhD scholarship and the Central Workshop, Department of Mechanical Engineering for the fabrication of essential components used in my experimental set-up.

My sincere thanks also go to my research group members Dr Elijah Ogaro Nyakang'o, Rajnandan Choudhury Das, Thilagraj R, Arkapravo Bera, Chirantan Mitra, Heramb Vivek Bhusane, and Samir Khan for their invaluable support and assistance. I want to thank my batch mates from 2016 and all my friends for creating a supportive and healthy environment during my time at the Indian Institute of Technology Guwahati.

Last but not least, I am grateful to my siblings, my parents, and my grandmother, for their love, prayers, care, and sacrifices made to educate and prepare me for the future. Their ongoing support and patience as I undertook my research and wrote my thesis have been invaluable to me. I am deeply grateful for their prayers and support, which have helped me reach this point in my academic journey.

Sincerely
Dangka Shylla

Abstract

This thesis reports on the theoretical and experimental studies of closed loop multi-level systems, where electromagnetically induced transparency (EIT) is dependent on the phase difference between the electromagnetic fields forming the loop. We first theoretically investigate a scheme to develop an atomic-based microwave (MW) interferometry in Rb, based on a six-level loopy ladder system involving the Rydberg states in which two excitation pathways interfere constructively or destructively depending on the phase between the MW electric fields closing the loop. Then we compared the field strength sensitivity to previous demonstrations on MW electrometry employing Rydberg atomic states, this is two orders of magnitude more sensitive to field strength. Because previously investigated atomic systems are only sensitive to field strength but not to phase, this scheme offers a great opportunity to characterize the MW completely, including the propagation direction and wavefront. Currently, we do not have the experimental facility for Rydberg excitation so we cannot conduct the experiment of the above theoretically proposed work. However, we could demonstrate the phase-dependent EIT in the different configurations of a closed loop double-lambda system at 780 nm and 420 nm transitions in ^{87}Rb at room temperature.

For the MW field measurements, the sensitivity can be improved by employing the cold atoms because cold atoms reduce the Doppler mismatch between the 780 nm probe and 480 nm control fields and also minimizes the collisions and transit time dephasing effect. Taking this into consideration, we have also set up the cold atom experiments and so far we have characterized the ^{85}Rb atoms in the MOT using the $5S_{1/2}(F = 3) \rightarrow 5P_{3/2}(F = 4)$ broad cyclic IR transition at 780 nm where we trap around 1.5×10^8 number of atoms at a typical temperature of 500 μK.

In laser cooling and trapping experiments, the temperature of the cold atoms is sensitive to the lock point of the laser fields. The laser locking can have an offset from the line center of the transition which depends upon the linewidth of the transition. In order to determine the laser lock offset on a particular atomic transition, we also present an experimental study on the effect of detuning on a velocity-induced population oscillation (VIPO) dip which is used to precisely determine the lock point with an uncertainty of around 100 kHz.

List of Publications

Publications for the work reported in this thesis

- Dangka Shylla, Elijah Ogaro Nyakang'o and Kanhaiya Pandey, "**Highly sensitive atomic based MW interferometry**," Sci. Rep. 8 8692 (2018) (https://doi.org/10.1038/s41598-018-27011-1)

- Dangka Shylla, Elijah Ogaro Nyakang'o, Rajnandan Choudhury Das, and Kanhaiya Pandey. "**Effect of detuning on velocity induced population oscillation**," Eur. Phys. J. D 76:125 (2022) (https://doi.org/10.1140/epjd/s10053-022-00431-5)

Additional publications

- Elijah Ogaro Nyakang'o, Dangka Shylla, Vasant Natarajan and Kanhaiya Pandey, "**Hyperfine measurement of the $6P_{1/2}$ state in ^{87}Rb using double resonance on blue and IR transition**," J. Phys. B: At. Mol. Opt. Phys. 53 095001 (6pp) (2020) (https://doi.org/10.1088/1361-6155/ab7670)

- Elijah Ogaro Nyakang'o, Dangka Shylla, Kirthanaa Indumathi, and Kanhaiya Pandey, "**Nature of interference between Autler-Townes (AT) peaks in generic multi-level system**," Eur. Phys. J. D 74: 187 (2020) (https://doi.org/10.1140/epid/e2020-10187-3)

- Rajnandan Choudhury Das, Dangka Shylla, Arkapravo Bera and Kanhaiya Pandey, "**Narrow-line cooling of ^{87}Rb using $5S_{1/2} \rightarrow 6P_{3/2}$ open transition at 420 nm**," J. Phys. B: At. Mol. Opt. Phys. 56 025301 (2023) (https://dx.doi.org/10.1088/1361-6455/acabf0)

Papers to be submitted

- Dangka Shylla, Rajnandan Choudhury Das, and Kanhaiya Pandey, "**Atomic coherence based multi lasers interferometry**."

Contents

List of Figures

Chapter 1

Introduction

ATOMIC coherence in multi-level systems, arising by simultaneous driving of the levels with electromagnetic fields is the key for quantum interference effects in the near-resonant electromagnetic field-atom interaction. Atomic coherence can result in a number of interesting phenomena like electromagnetically induced transparency (EIT) [4, 5], coherent population trapping (CPT) [6], lasing without inversion [7–9], storage and retrieval of light [10–12].

In multi-level system, EIT is a phenomenon in which the probe absorption is modified in presence of strong electromagnetic fields known as pump or control fields and has been extensively studied [13–15]. The EIT phenomenon can be explained using two approaches: the bare atomic state picture and dressed states atomic picture. In the bare atomic state picture, EIT takes place due to the coherence induced between the levels which are not directly driven by the electromagnetic fields. In the dressed states atomic picture, the presence of strong pump fields creates dressed states providing different excitation pathways for the weak probe field resulting in quantum interference between the different pathways. For three level system, there are three possible EIT configurations which are Λ, V and Ξ-type systems [16–18]. One of the striking features of EIT is the narrow linewidth that it offers which is the reason for many fundamental and key

applications in high-resolution spectroscopy [19–21], polarization control [22–24], magnetometry [25–31], atomic clocks [32], Raman velocimetry [33], slow light [34–36], laser cooling [37], etc.

Further, EIT involving Rydberg atomic states is an important spectroscopic tool for many interesting phenomena and applications such as dipole blockade [38], photon-photon interaction [39], optical nonlinearity [40], quantum information [41], nonlinear optics [42], microwave [43, 44] and radio-frequency measurements [45–47], etc. Rydberg states are atomic states with high principal quantum number n and possesses large polarizability. The above-mentioned applications are made possible by the properties of the Rydberg states.

1.1 Motivation

One of the interesting properties of the Rydberg states is its large electric polarizability which makes the Rydberg atoms to be highly sensitive to the electromagnetic fields. The frequency range of the electromagnetic fields can span from the radiofrequency (RF), microwave (MW) to terahertz due to the availability of the Rydberg states separated at the frequencies that can be driven by these fields by choosing the appropriate principal quantum number n. Electromagnetic fields are characterized by their strength, frequency, polarization and phase. Recently the atom based electrometry for electromagnetic field measurements has been investigated using the Rydberg atoms [48–53]. The atom based electrometry has been used to measure the strength of MW electromagnetic fields with a high sensitivity up to $30\ \mu\text{V cm}^{-1}\ \text{Hz}^{-1/2}$, minimum detectable field up to $8\ \mu\text{V cm}^{-1}$ [49] and the polarization with an angular resolution of 0.5° [50]. The phase has also been measured using the atom based MW electrometry by heterodyne technique where there is interference between the two MW fields in space leading to a phase resolution of 0.6° [54].

In comparison to the above atom based MW electrometry, the minimum detectable field using the traditional antenna method for the MW field is only up to 10 mVcm^{-1} [55, 56]. Using the optical method for the electromagnetic fields converted by the dipole antenna

the minimum detectable field is improved up to 30 μVcm^{-1} [57] with sensitivity upto 1 mVcm^{-1} Hz$^{-1/2}$ [56]. So, the strength sensitivity achieved by the atom based MW electrometry is three orders of magnitude better than the traditional antenna method. Further, the spatial resolution of the atom based MW electrometry is sub-wavelength ($\lambda_{MW}/650$) [58] which is difficult to achieve with traditional antenna method as the dimension of the antenna itself happens to be $\lambda_{MW}/2$. The atom based MW electrometry is carried out using a four level ladder system and a very basic experimental set-up with a Rb cell operating at room temperature [49]. But it is not sensitive to the phase of the electromagnetic field because in steady state EIT is not sensitive to the phase of the electromagnetic fields for open loop system which limits the phase determination. This limitation can be overcome by using the closed loop multi-level system.

In steady state regime for closed loop multi-level systems, phase-dependent EIT has been observed and has been rigorously studied [59–62]. These studies show that in the closed loop multi-level systems coupled by multiple pump fields, there can be different excitation pathways provided by the pump fields that can interfere constructively or destructively depending upon the relative phases of the electromagnetic fields forming the loop. The different paths of excitation can also be due to oppositely polarized electromagnetic fields and hence the interference is observed between them which is in contrast to the interference in space. Hence, this provides us the opportunity to characterize the electromagnetic field completely which includes the phase. In this thesis we present a theoretical study of the atom based MW interferometry using a six level loopy ladder system involving the Rydberg states which is phase sensitive and is two orders of magnitude more sensitive to field strength as compared to previous demonstrations. In a similar line to our theoretical study, an experimental work has also been done using a loopy system for the phase measurement of RF field which is measured over a range of π, and a sensitivity of 0.1° is achieved [63].

In order to experimentally realise the principle of phase-dependent EIT (i.e., atomic coherence based interferometry) in closed loop systems, we present a double Λ-type system to study the phase sensitivity and frequency response of the system. We have chosen two configurations of the double Λ-type system. The first configuration involves the excited states with same decay rates at the 780 nm transition and the second configuration

involves the excited states with different decay rates at the 780 nm and 420 nm transitions. Previous demonstration for the phase-sensitivity in the double Λ-type system, has also been reported but involving states with same decay rates at 780 nm transition [64]. The double Λ-type system has also be demonstrated using artificial atoms for the phase detection where the interference between the fields can have a large frequency difference [65].

The sensitivity of the MW field measurement at room temperature is also limited by the transit time broadening, Doppler mismatch between the probe and the control fields, collisions, etc. These effects can be reduced by employing a cold gas cloud of atoms, which will also increase the sensitivity of the MW field measurement. In light of this, we also present the laser cooling and trapping experiments for Rb atoms at 780 nm transition using magneto-optical trap (MOT) where we determine the temperature of the atoms. The cold gas cloud of Rb atoms is also a starting point for many experimental studies in high precision spectroscopy [66], atom interferometry [67, 68], Bose-Einstein condensation (BEC) [69], atomic clocks [70], etc.

In laser cooling and trapping experiments, the temperature of the cold atoms is sensitive to the lock point of the laser fields. The laser locking can have an offset from the line center of the transition which depends upon the linewidth of the transition. In order to determine of the laser lock offset on a particular atomic transition, we present an experimental study on the effect of detuning on a velocity-induced population oscillation (VIPO) dip and utilize the effect to precisely determine the lock point. VIPO is a phenomenon of temporal modulation of population difference between two levels induced by the beating of the two laser fields with same polarization driving the same transition [71–73]. The VIPO phenomenon has also been rigorously studied for the saturated fluorescence spectrum in two-level system and is a very useful spectroscopic technique for weak transitions [74]. It has also been utilized for the removal of crossover peaks and broadening due to mismatch of the wavelength for probe and control lasers [75, 76] and hence resolve the closely spaced hyperfine levels in Rb for Doppler mismatched double resonance [77].

In summary, the thesis aims to establish a connection between microwave field measurements, laser cooling and trapping experiments, and the VIPO phenomenon in order to improve the sensitivity of the microwave field measurements and advance our understanding of atomic physics. As the sensitivity of MW field measurement at room temperature can be limited by various factors, including transit time broadening, Doppler mismatch between the probe and control fields, and collisions. However, using laser cooling and trapping of atoms enable the production of a cold gas cloud of atoms, which can reduce these limitations. The temperature of the cold atoms in these experiments is sensitive to the lock point of the laser fields. The lock point of the laser fields can have an offset from the line center of the atomic transition. The VIPO phenomenon is a useful spectroscopic technique that can be used to determine the laser locking offset. By precisely determining the laser lock point using the VIPO phenomenon, we can improve the accuracy of measurements, and the use of cold atoms can further reduce the limitations caused by transit time broadening, Doppler mismatch, and collisions, leading to an improvement in the sensitivity of field measurements.

1.2 Thesis outline

This thesis presents the study of the electromagnetic wave interferometry in closed loop multi-level systems based on atomic coherence. The thesis is divided into seven chapters, each of which is explained in the following sections.

Chapter 1 titled as "**Introduction**" discusses the background on atomic based sensors involving the atomic coherence effects, as well as the motivation for the research and a general summary of the thesis.

Chapter 2 titled as "**Theoretical framework**" discusses the theoretical basis of the electromagnetic field-atom interaction using the semi-classical approach. The chapter begins with the simplest system, a two-level atom interacting with an electromagnetic field. The density matrix formalism is used to determine the polarization of the medium,

susceptibility, atomic coherence, and population of the distinct atomic states. The chapter then moves on to the generalization of the density matrix formalism for multi-level atom. The mechanism for Doppler cooling, as well as laser cooling and trapping of atoms, are briefly discussed. The atomic structure of Rb and some relevant information, such as the theory of fine, hyperfine interaction and Zeeman splitting are discussed at the end of the chapter.

Chapter 3 titled as "**Highly sensitive atomic based MW interferometry**" presents the theoretically study of a scheme to develop an atomic based microwave (MW) interferometry in Rb. This scheme is based on the phase-dependent EIT where we employed a six-level loopy ladder system involving the Rydberg states in which two excitation pathways interfere constructively or destructively depending on the phase between the MW fields forming the loop. We compared the MW field strength sensitivity to previous demonstrations on MW electrometry using Rydberg atomic states, and found that this is two orders of magnitude more sensitive to field strength. As the previous demonstrations are only sensitive to field strength and not to the phase, this scheme offers a great opportunity to characterize the MW completely, including the propagation direction and wavefront.

Chapter 4 titled as "**Atomic coherence based multi lasers interferometry**" presents the experimental study of an atomic coherence based multi laser interferometry in a closed loop double Λ-type system using a Rb vapour cell at room temperature. This scheme is based upon the principle of phase-dependent electromagnetically induced transparency (EIT). EIT in closed loop systems is dependent on the phase difference between the electromagnetic fields forming the loop. The phase dependence arises from the fact that there are two paths of excitation which can interfere constructively or destructively depending on the phase difference between them. These two paths can be due to two oppositely polarized electromagnetic fields and hence the interference is observed between them which is in contrast to the interference in space. In order to experimentally realise the principle of phase-dependent EIT (i.e., atomic coherence based interferometry) in closed loop systems, we explore this effect in two different configuration of a closed

loop double Λ-type system. The first configuration involves the excited states with same decay rates at the 780 nm transition and the second configuration involves the excited states with different decay rates at the 780 nm and 420 nm transitions.

Chapter 5 titled as "**Characterization of ^{85}Rb MOT with 780 nm laser**" presents the characterization of the cold Rb atoms in the magneto-optical trap (MOT). We set up the cold atom experiments and performed the cold atom characterization for ^{85}Rb atoms in the MOT using the $5S_{1/2}(F = 3) \rightarrow 5P_{3/2}(F = 4)$ broad cyclic IR transition at 780 nm. We studied the behaviour of the cold ^{85}Rb atoms in the MOT with various parameters such as hold time, power of cooling beam as well as the repumping beam. We also measured the optical density, the number of atoms and the temperature using absorption imaging.

Chapter 6 titled as "**Effect of detuning on velocity induced coherent population oscillation**" presents an experimental study on the effect of detuning on the velocity induced coherent population oscillation (VIPO) for a Doppler mismatched double resonance conducted on 780 nm at IR transition and at 421 nm at blue transition in ^{87}Rb at room temperature. We measured the shift of the VIPO dip from the line center of the transparency or enhanced absorption (EA) peaks as a result of the lock offset point of the resonantly driving laser i.e., the IR laser in this case. This effect is used to precisely determine the locking point of the IR laser on the $5S_{1/2}(F = 2) \rightarrow 5P_{3/2}(F = 3)$ transition.

Chapter 7 titled as "**Conclusions**" outlines the thesis conclusions as well as future study.

Chapter 2

Theoretical framework

THIS chapter outlines the theoretical framework required in describing the research works involved in this thesis which is the electromagnetic field-atom interaction. We begin with the simplest system, a two-level atom interacting with an electromagnetic field, and using a semi-classical technique where the atom is depicted as a quantum mechanical object that interacts with the classical field to model the interaction Hamiltonian. The density matrix formalism is used to determine the polarization of the medium, susceptibility, atomic coherence, and population of the distinct atomic states. The chapter then moves on to the generalization of the density matrix formalism for multi-level atom. The mechanism for Doppler cooling, as well as laser cooling and trapping of atoms, are briefly discussed. As this thesis involves the experiments in the Rb atomic medium, the atomic structure of Rb and some relevant information, such as the theory of fine, hyperfine interaction and Zeeman splitting are discussed at the end of the chapter.

2.1 Electromagnetic field-atom interaction

The electromagnetic field-atom interaction has produced many amazing phenomena and has received significant interest in the research areas of Atomic, Molecular, and Optical (AMO) physics. Depending on the phenomenon we would like to explore, we have a variety of approaches for describing them [78]. These can be classified into the classical, semi-classical and full quantum approach.

In the classical approach, the atom is considered to be a classical harmonic oscillator with an electron bound to a nucleus by a linear spring. If a classical electromagnetic field interacts with such an atom, it begins to oscillate. This approach allows us to explain a wide range of phenomena, including the refractive index (absorption and dispersion) of an atomic medium, laser cooling and trapping of atoms, however it does not take into consideration fundamental concepts like the energy levels and size of atom. It is not able to account for phenomena such as black body radiation, photoelectric effect, etc. The quest to find solutions to these problems gave rise to other approaches. In the semi-classical approach, the atom is considered to be a quantum mechanical object with its discrete energy levels and the electromagnetic field to be a classical field. The two-level atom is the simplest scenario utilized in this approach to represent the electromagnetic field-atom interaction. This approach allows us to describe numerous quantum phenomena by solving the time-dependent Schrödinger equation using the density matrix formalism, but it is unable to take into account the different types of quantum statistics that exist in the electric field. In the full quantum approach, both the atom and the electromagnetic field are considered as quantum mechanical objects, i.e, each mode of the electric field is associated with a quantized simple harmonic oscillator. This approach is superior because it can now account for everything that the classical and semi-classical approach could not account for.

We will focus on the semi-classical approach of the electromagnetic field-atom interaction since it is sufficient to explain the research work presented in this thesis.

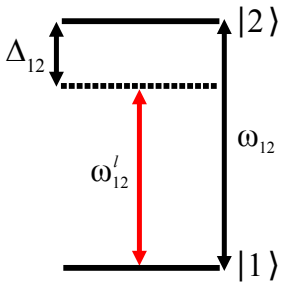

FIGURE 2.1: The energy level diagram for a two-level atom with states $|1\rangle$ and $|2\rangle$ separated in energy by $\hbar\omega_{12}$ interacting with an electromagnetic wave of frequency ω_{12}^l and detuned from the atomic resonance by Δ_{12}.

2.2 Two-level atom

We consider a two-level atom with a ground state $|1\rangle$ and an excited state $|2\rangle$ with energies $\hbar\omega_1$ and $\hbar\omega_2$ respectively, interacting with an electromagnetic field of frequency ω_{12}^l as shown in Fig. 2.1. We can write the Hamiltonian for such a system as

$$H = H_0 + H_I, \tag{2.1}$$

where $H_0 = \hbar\omega_1|1\rangle\langle 1| + \hbar\omega_2|2\rangle\langle 2|$ is the bare atomic Hamiltonian such that $H_0|1\rangle = \hbar\omega_1|1\rangle$ and $H_0|2\rangle = \hbar\omega_2|2\rangle$. $H_I = -\vec{d}\cdot\vec{E}$ is the Hamiltonian describing the electromagnetic-field interaction, with the electric dipole $\vec{d} = -e\vec{r}$ and the electromagnetic field $\vec{E} = \hat{\epsilon}E_0\cos(\omega_{12}^l t)$ in the dipole approximation. In the dipole approximation, we have neglected the spatial dependence of the field since the wavelength of electromagnetic field is much larger than the size of the atom.

The atomic wavefunction $|\psi\rangle$ as a function of time t can be expressed as a linear combinaton of the states basis $|1\rangle$ and $|2\rangle$ given by

$$|\psi(t)\rangle = c_1(t)e^{-i\omega_1 t}|1\rangle + c_2(t)e^{-i\omega_2 t}|2\rangle, \tag{2.2}$$

where $c_1(t)$ and $c_2(t)$ are the complex co-efficients. The evolution of the system is governed by the time-dependent Schrödinger equation given by

$$i\hbar|\dot{\psi}\rangle = H|\psi(t)\rangle. \tag{2.3}$$

In order to obtain the dynamics of the system, we solve the time-dependent Schrödinger equation by substituting 2.1 and 2.2 into 2.3 and we obtain a set of coupled differential equations

$$\begin{aligned} i\hbar\dot{c_1}(t) =& c_2(t)\langle 1|\vec{d}\cdot\vec{E}|2\rangle e^{-i(\omega_2-\omega_1)t}, \\ i\hbar\dot{c_2}(t) =& c_1(t)\langle 2|\vec{d}\cdot\vec{E}|1\rangle e^{i(\omega_2-\omega_1)t}. \end{aligned} \tag{2.4}$$

We then introduce the Rabi frequency $\Omega_{12} = -\dfrac{eE_0\langle 2|r|1\rangle}{\hbar}$ which describes the coupling strength between the electromagnetic field and atom. Using the exponential form of $\cos(\omega_{12}^l t)$, the above coupled equations can now be written as

$$\begin{aligned} i\hbar\dot{c_1}(t) =& \frac{\hbar\Omega_{12}}{2}\left[e^{i(\omega_{12}^l-(\omega_2-\omega_1))t} + e^{-i(\omega_{12}^l+(\omega_2-\omega_1))t}\right]c_2(t), \\ i\hbar\dot{c_2}(t) =& \frac{\hbar\Omega_{12}}{2}\left[e^{i(\omega_{12}^l+(\omega_2-\omega_1))t} + e^{-i(\omega_{12}^l-(\omega_2-\omega_1))t}\right]c_1(t). \end{aligned} \tag{2.5}$$

We now employ the rotating wave approximation (RWA) to eliminate the counter-rotating terms like $\omega_{12}^l + (\omega_2 - \omega_1)$ which oscillates at about twice the frequency of the interacting electromagnetic field, as their time dependence averages out to zero. It is a good approximation close to resonance $|\omega_{12}^l - (\omega_2 - \omega_1)| \ll (\omega_2 - \omega_1)$, and when the Rabi frequency is sufficiently small ($\Omega \ll \omega_{12}^l$) [79]. The above coupled equations reduced to

$$\begin{aligned} i\hbar\dot{c_1}(t) =& \frac{\hbar\Omega_{12}}{2}e^{i\Delta_{12}t}c_2(t), \\ i\hbar\dot{c_2}(t) =& \frac{\hbar\Omega_{12}}{2}e^{-i\Delta_{12}t}c_1(t), \end{aligned} \tag{2.6}$$

where $\Delta_{12} = \omega_{12} - (\omega_2 - \omega_1)$ is defined as the detuning of the electomagnetic field. To remove the explicit time dependence from the above equations, we define the transformations given by

$$\begin{aligned} \tilde{c_1}(t) =& c_1(t), \\ \tilde{c_2}(t) =& e^{-i\Delta_{12}t}c_2(t). \end{aligned} \tag{2.7}$$

In terms of these new coefficients, the above coupled equations become

$$\begin{aligned} i\hbar\dot{\tilde{c_1}}(t) =& \frac{\hbar\Omega_{12}}{2}\tilde{c_2}(t), \\ i\hbar\dot{\tilde{c_2}}(t) =& \frac{\hbar\Omega_{12}}{2}\tilde{c_1}(t) - \hbar\Delta_{12}c_2(t), \end{aligned} \tag{2.8}$$

and the Hamiltonian can be written in matrix form as

$$H = \hbar \begin{bmatrix} -\Delta_{12} & \frac{\Omega_{12}}{2} \\ \frac{\Omega_{12}}{2} & 0 \end{bmatrix}. \tag{2.9}$$

Assuming at $t = 0$, the total population is in the ground state $|1\rangle$ such that $c_1 = 1$ and $c_2 = 0$, then on solving Eqs. 2.8 we obtain the expression

$$|c_2(t)|^2 = \frac{\Omega_{12}^2}{\Omega_{12}'^2} \sin^2\Big(\frac{\Omega_{12}' t}{2}\Big), \tag{2.10}$$

where $\Omega_{12}' = \sqrt{|\Omega_{12}|^2 + \Delta_{12}^2}$. $|c_2(t)|^2$ is the probability of finding the population in the excited state $|2\rangle$ at time t. At resonance $\Delta_{12} = 0$, the above expression of probability reduces to

$$|c_2(t)|^2 = \sin^2\Big(\frac{\Omega_{12} t}{2}\Big), \tag{2.11}$$

where we can see that the probability to be in the excited state $|2\rangle$ undergoes Rabi oscillations between $|1\rangle$ and $|2\rangle$ at frequency Ω_{12} which is known as the Rabi frequency.

The Hamiltonian given in Eq. 2.9 is diagonalized to find the eigenvalues and eigen vectors. The eigen values are

$$E_{1,2} = \frac{\hbar}{2}(-\Delta_{12} \mp \Omega_{12}'). \tag{2.12}$$

For large detunings $\Omega_{12} \ll |\Delta_{12}|$, the energy shift of the ground $|1\rangle$ and excited $|2\rangle$ states are given by

$$\Delta E_{1,2} = \pm \frac{\hbar \Omega_{12}^2}{4\Delta_{12}}, \tag{2.13}$$

which is known as light or AC Stark shift. The corresponding eigenvectors are

$$\begin{aligned} |+\rangle &= \cos\theta\,|1\rangle - \sin\theta\,|2\rangle\,, \\ |-\rangle &= \sin\theta\,|1\rangle + \cos\theta\,|2\rangle\,, \end{aligned} \tag{2.14}$$

where $\cos 2\theta = -\frac{\Delta_{12}}{\Omega_{12}'}$. $|\pm\rangle$ are called the dressed states of the atoms. At resonance $\Delta_{12} = 0$, the eigenstates become $|\pm\rangle = \frac{|1\rangle + |2\rangle}{\sqrt{2}}$. The energies $E_{1,2} = \pm\frac{\hbar\Omega}{2}$ are unperturbed and this energy splitting is called the Autler-Townes splitting [80].

2.2.1 Density matrix formalism

The evolution of the system has been characterized in terms of state vector $|\psi\rangle$ which gives complete information about a system in a pure state. Although we cannot measure $|\psi\rangle$ directly in experiments, we can measure the expectation values of any Hermitian operator $\hat{A}$ defined as $< \hat{A} >= \langle\psi| \hat{A} |\psi\rangle$. We alternatively define a density operator ρ which we can express in terms of $|\psi\rangle$ given by

$$\rho = |\psi\rangle \langle\psi| , \tag{2.15}$$

which can be written in matrix form for a two-level system as

$$\rho = \begin{bmatrix} \rho_{11} & \rho_{12} \\ \rho_{21} & \rho_{22} \end{bmatrix} = \begin{bmatrix} c_1(t)c_1(t)^* & c_1(t)c_2(t)^* \\ c_2(t)c_1(t)^* & c_2(t)c_2(t)^* \end{bmatrix} . \tag{2.16}$$

The diagonal elements are called populations and the off-diagonal elements are called coherences and has the property $\rho_{11} + \rho_{22} = 1$ and $\rho_{21} = \rho_{12}^*$. The system changes its state from original state to final state as a result of the incoherent processes like spontaneous emission, the collisional and transit relaxation, which also transforms a pure state into a statistical mixture. For a statistical mixture of states $|\psi_i\rangle$ the density matrix operator of the system is given by

$$\rho = \sum_{i=1} P_i |\psi_i\rangle \langle\psi_i| , \tag{2.17}$$

where P_i is the probability of the system being in state $|\psi_i\rangle$. The time evolution of the density matrix operator is obtained from the time-dependent Schrödinger equation Eq. 2.3 and is expressed as

$$\dot{\rho} = -\frac{i}{\hbar}[H, \rho]. \tag{2.18}$$

This equation is called the Liouville's equation and describes only the coherent process. To include the incoherent processes such as spontaneous emission, the decay rates are added phenomenologically in Eq. 2.18. In the two-level system, the time evolution of

the population due to spontaneous emission with a decay rate of Γ_2 [81] is given by

$$\dot{\rho}_{22} = -\dot{\rho}_{22} = -\Gamma_2\rho_{22}, \tag{2.19}$$

and that of the coherences

$$\dot{\rho}_{21} = -\dot{\rho}_{12} = -\frac{\Gamma_2}{2}\rho_{21}. \tag{2.20}$$

The full equation governing the evolution of the density matrix in two-level system is now given by

$$\dot{\rho} = -\frac{i}{\hbar}[H,\rho] - \begin{bmatrix} -\Gamma_2\rho_{22} & \frac{\Gamma_2}{2}\rho_{12} \\ \frac{\Gamma_2}{2}\rho_{21} & \Gamma_2\rho_{22} \end{bmatrix}. \tag{2.21}$$

Using the Hamiltonian given by Eq. 2.9 in Eq. 2.21, we obtain the coupled equations for two-level atom

$$\begin{aligned} \dot{\rho}_{11} =& \frac{i}{2}(\Omega^*\rho_{21} - \Omega\rho_{12}) + \Gamma_2\rho_{22}, \\ \dot{\rho}_{12} =& \frac{i}{2}\Omega^*(\rho_{22} - \rho_{11}) - \Big(\frac{\Gamma_2}{2} + i\Delta_{12}\Big)\rho_{12}, \\ \dot{\rho}_{21} =& \frac{i}{2}\Omega(\rho_{11} - \rho_{22}) - \Big(\frac{\Gamma_2}{2} - i\Delta_{12}\Big)\rho_{21}, \\ \dot{\rho}_{22} =& \frac{i}{2}(\Omega\rho_{12} - \Omega^*\rho_{21}) - \Gamma_2\rho_{22}. \end{aligned} \tag{2.22}$$

These equations are called the optical Bloch equations (OBE). On solving, the coherence terms gives us the probe absorption and the population terms gives us the scattering rates.

2.2.2 Multi-level atom

The density matrix formalism can be extended to multi-level atom excited by several lasers. The generalized Hamiltonian for a multi-level atom can be written as

$$H = H_0 + H_I = \sum_i^n \hbar\omega_i \left|i\right\rangle\left\langle i\right| + \Big[\sum_i^n \frac{\hbar\Omega_{i,i+1}}{2}(e^{i\omega_i^l,i+1} + e^{-i\omega_i^l,i+1})\left|i\right\rangle\left\langle i+1\right| + h.c.\Big], \tag{2.23}$$

where, $h.c.$ is the Hermitian conjugate and $\Omega_{ij} = d_{ij}E_{ij}e^{i\phi_{ij}}$ is the generalized Rabi frequency for the transition $|i\rangle \rightarrow \langle j|$ having dipole matrix d_{ij}. For simplicity of calculation, the Hamiltonian is transformed to the interaction picture using a time evolution operator U defined as

$$U = e^{iH_0t/\hbar} = \sum_i e^{i\omega_i t} |i\rangle \langle i| . \tag{2.24}$$

The transformation of Hamiltonian is given by

$$UHU^+ = \sum_i^n \hbar\omega_i |i\rangle \langle i| + \Big[\sum_i^n \frac{\hbar\Omega_{i,i+1}}{2}(e^{i\omega_i^{l},i+1} + e^{-i\omega_i^{l},i+1})e^{-i(\omega_{i+1}-\omega_i)} |i\rangle \langle i+1| + h.c.\Big]. \tag{2.25}$$

Under the assumption that $|\omega_{i,i+1}^l - (\omega_{i+1} - \omega_i)| \ll 0$ which is the resonance condition, the terms like $e^{\pm\omega_{i,i+1}^l + (\omega_{i+1}-\omega_i)}$ oscillating with twice the frequency of $\omega_{i,i+1}^l$ are eliminated as their time dependence averages out to zero by RWA. The general detuning of the electromagnetic field is defined as $\Delta_{i,i+1} = \omega_{i,i+1}^l + (\omega_{i+1} + \omega_i)$. The transformed Hamiltonian after RWA is given by

$$\begin{aligned} H = \sum_i^n \hbar\omega_i |i\rangle \langle i| + \frac{\hbar}{2}\Big[&\Omega_{12}e^{i\Delta_{12}t} |1\rangle \langle 2| + \Omega_{13}e^{i\Delta_{13}t} |1\rangle \langle 3| + ... + \Omega_{23}e^{\pm i\Delta_{23}t} |2\rangle \langle 3| \\ &+\Omega_{24}e^{\pm i\Delta_{24}t} |2\rangle \langle 4| + ... + \Omega_{n-1n}e^{\pm i\Delta_{n-1n}t} |n-1\rangle \langle n| + h.c.\Big]. \end{aligned} \tag{2.26}$$

In order to remove the time dependence, the Hamiltonian needs to be transformed in corotating frame and the new basis is known as rotating basis. The unitary matrix $\tilde{U}$ which transforms the Hamiltonian is defined as

$$\tilde{U} = 1 |1\rangle \langle 2| + e^{i\Delta_{12}t} |2\rangle \langle 2| + e^{i(\Delta_{23}\pm\Delta_{12})t} |3\rangle \langle 3| + ..., \tag{2.27}$$

for atomic systems such as Ξ-type and Λ-type systems and

$$\tilde{U} = 1 |1\rangle \langle 2| + e^{i\Delta_{12}t} |2\rangle \langle 2| + e^{i\Delta_{23}t} |3\rangle \langle 3| + ..., \tag{2.28}$$

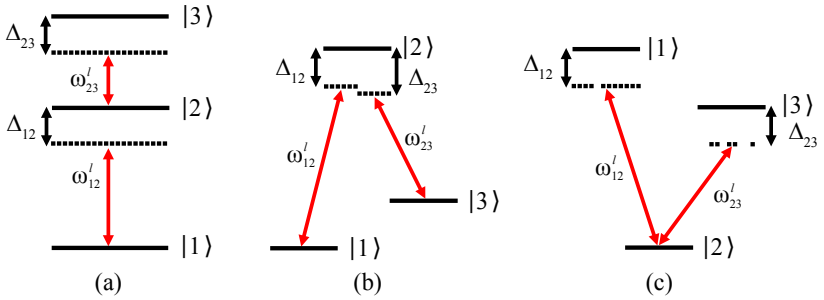

FIGURE 2.2: The energy level diagram for the (a) Ξ-type, (b) Λ-type, and (b) V-type configuration with states $|1\rangle$, $|2\rangle$ and $|3\rangle$ interacting with electromagnetic fields of frequencies ω_{12}^{l} coupling the states $|1\rangle$ and $|2\rangle$ and ω_{23}^{l} coupling the states $|2\rangle$ and $|3\rangle$ with Δ_{12} and Δ_{23} as the respective detunings.

for V-type. The new basis is related to old basis by $\left|\tilde{\psi}\right\rangle = \tilde{U}\left|\psi\right\rangle$. The Hamiltonian in corotating frame should satisfy the Schrödinger equation as

$$\begin{aligned}\tilde{H}\left|\tilde{\psi}\right\rangle &= i\hbar\left|\dot{\tilde{\psi}}\right\rangle \\ &= i\hbar\left[\dot{\tilde{U}}\left|\psi\right\rangle + \tilde{U}\dot{\psi}\right]\tilde{H}\left|\tilde{\psi}\right\rangle \\ &= \left[i\hbar\dot{\tilde{U}}\tilde{U}^{\dagger} + \tilde{U}H\tilde{U}^{\dagger}\right]\tilde{U}\left|\psi\right\rangle \\ &= \left[i\hbar\dot{\tilde{U}}\tilde{U}^{\dagger} + \tilde{U}H\tilde{U}^{\dagger}\right]\left|\tilde{\psi}\right\rangle.\end{aligned} \tag{2.29}$$

Finally, the dynamics of the system can be studied in density matrix formalism using the Liouville master equation given by,

$$\dot{\rho} = -\frac{i}{\hbar}[H,\rho] - \frac{1}{2}\{\Gamma,\rho\}, \tag{2.30}$$

which on solving we obtain a linear set of n^2 coupled differential equations. The components ρ_{ii} correspond to the population terms of the levels $|i\rangle$ and the non-diagonal elements ρ_{ij} describe the coherences between levels $|i\rangle$ and $|j\rangle$.

The two-level atom is an ideal representation of the real atom, in reality the atom is multi-level. The presence of a third level in system such as Λ, Ξ and V type shown in Fig. 2.2 reveals many other quantum phenomena such as optical pumping, electromagnetically induced transparency (EIT), etc. Optical pumping is an important incoherent effect that

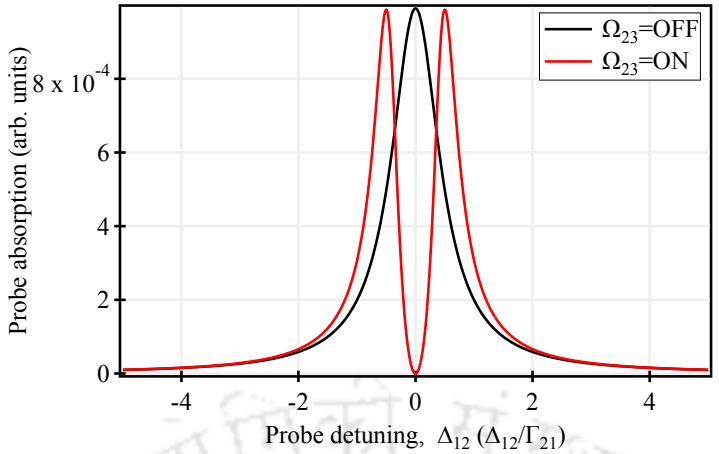

FIGURE 2.3: The probe absorption, ρ_{12} vs probe detuning, Δ_{12}. The black curve shows the probe absorption in absence of coupling field, $\Omega_{23} = 0$ which is a Lorentzian and red curve shows the modified probe absorption in presence of coupling field $\Omega_{23} \neq 0$ which is the effect of EIT.

arises from the availability of more than one decay channels where as EIT is a coherent phenomenon that occurs when more than one lasers are involved.

Electromagnetically induced transparency

In this section we discuss the phenomenon of EIT using the Λ-type configuration shown in Fig. 2.2b where states $|1\rangle$ and $|2\rangle$ are coupled by a probe field Ω_{12} and states $|2\rangle$ and $|3\rangle$ by a control field Ω_{23}. The Hamiltonian for the Λ-type configuration under RWA and in rotating frame can be written as

$$H = \hbar \begin{bmatrix} 0 & \frac{\Omega_{12}}{2} & 0 \\ \frac{\Omega_{12}}{2} & -2\Delta_{12} & \frac{\Omega_{23}}{2} \\ 0 & \frac{\Omega_{23}}{2} & -2(\Delta_{12} - \Delta_{23}) \end{bmatrix}, \tag{2.31}$$

where Δ_{12} and Δ_{23} are the detuning of the probe and coupling fields respectively.

In the bare atomic state picture, the absorption of the probe field in a Λ system is analysed between bare states $|1\rangle$ and $|2\rangle$ using density matrix formalism and is given by

ρ_{12}. The expression for ρ_{12} is given by

$$\rho_{12} = \frac{\frac{i}{2}\frac{\Omega_{12}}{\Gamma_{12}}}{1 + \frac{1}{4}\frac{|\Omega_{23}|^2}{\Gamma_{12}\Gamma_{23}}}. \tag{2.32}$$

The probe absorption as a function of probe detuning Δ_{12} is plotted in Fig. 2.3. When the coupling field is off, the probe absorption is shown by a black line which is an absorption peak. When the coupling field is on, the probe absorption is shown by a red curve which shows the EIT resonance at line center.

In the dressed state atomic picture, assuming the case for two-photon resonance condition $\Delta_{12} = \Delta_{23} = \Delta$ and then diagonalizing the above Hamiltonian we obtain the eigenvalues

$$E_1 = 0 \text{ and } E_{2,3} = \Delta \pm \sqrt{\Omega_{12}^2 + \Omega_{23}^2 + \Delta^2}, \tag{2.33}$$

with corresponding eigenstates known as the dresses states

$$\begin{aligned} |D\rangle &= \cos\theta\,|1\rangle - \sin\theta\,|3\rangle\,, \\ |+\rangle &= \sin\theta\sin\phi\,|1\rangle + \cos\theta\,|2\rangle + \cos\theta\cos\phi\,|3\rangle\,, \\ |-\rangle &= \cos\theta\sin\phi\,|1\rangle - \sin\theta\,|2\rangle + \cos\theta\cos\phi\,|3\rangle\,, \end{aligned} \tag{2.34}$$

and the mixing angles

$$\tan\theta = \frac{\Omega_{12}}{\Omega_{23}} \text{ and } \phi = \frac{\sqrt{\Omega_{12}^2 + \Omega_{23}^2}}{\Delta}. \tag{2.35}$$

We can infer from Eqs. 2.34 that the zero energy eigenstate $|D\rangle$ has no contribution from state $|2\rangle$ and is called a dark state since there is no possibility of excitation to state $|2\rangle$. However, the states $|\pm\rangle$ contains all the bare atomic states $|1\rangle$, $|2\rangle$ and $|3\rangle$ are known as bright states. These pairs of states are shifted in energy by

$$\Delta E_{2,3} = \frac{\hbar}{2}\Big(\Delta \pm \sqrt{\Delta^2 + \Omega_{12}^2 + \Omega_{23}^2}\Big), \tag{2.36}$$

which is known as Autler-Townes splitting. In the weak probe limit $\Omega_{12} \ll \Omega_{23}$ and for $\Delta = 0$, the dark state becomes identical to the ground state $|1\rangle$, $|D\rangle = 0$. The bright states $|\pm\rangle = \dfrac{|1\rangle \pm |0\rangle}{\sqrt{2}}$ have excitation probability amplitudes that are equal but opposite

in signs leading to destructive interference of the two excitation pathways. In other words, the probe beam is transmitted rather than being absorbed, an effect commonly known as EIT.

2.2.3 Microscopic and Macroscopic relation

The density matrix formalism determines the state of a two-level system that is interacting with an electromagnetic field. Relating this microscopic theory for a single atom to laboratory observations like absorption spectra is our objective. In order to relate the microscopic and macroscopic properties we begin with polarizability which completely characterizes the response of the atom to the electromagnetic field and is written as

$$\vec{P} = \epsilon_0 \chi(\omega_{12}^l)\vec{E}, \tag{2.37}$$

where ϵ_0 is the permittivity of free space and $\chi(\omega_{12}^l)$ is called the susceptibility of the medium which is a key parameter that describes the absorptive and dispersive properties of the medium. For simplicity we have assumed that the electric polarization $\vec{P}$ is linearly proportional to the electromagnetic field.

We know that the dipole moment of a single atom can be calculated using the density matrix operator as

$$\langle d \rangle = Tr(\rho d) = d_{12}(\rho_{12} e^{-i\omega_{12}^l t} + \rho_{21} e^{i\omega_{12}^l t}). \tag{2.38}$$

By definition the polarization $\vec{P}$ of the atomic medium is dipole moment per unit volume and is given by

$$P = n \langle d \rangle , \tag{2.39}$$

where $n = \dfrac{N}{V}$ is the atomic number density. Substituting Eq. 2.38 in 2.37 and equating 2.37 and 2.39

$$n d_{12}(\rho_{12} e^{-i\omega_{12}^l t} + \rho_{21} e^{i\omega_{12}^l t}) = \frac{1}{2}\epsilon_0 E_0(\chi(\omega_{12}^l) e^{-i\omega_{12}^l t} + \chi^*(\omega_{12}^l) e^{i\omega_{12}^l t}), \tag{2.40}$$

we obtain the expression

$$\chi(\omega_{12}^{l}) = -\frac{2nd_{12}}{\epsilon_0}\rho_{12}, \tag{2.41}$$

which is a relation between susceptibility and the induced dipole moment of the atom and it establishes the link between the macroscopic and microscopic properties of the medium. This result can be generalized in a very straightforward way to establish the susceptibility in a multi-level atom.

2.3 Laser cooling: Doppler cooling

Laser cooling and trapping [79] of atoms is an essential experimental method that is widely used in AMO physics. It depends on the electromagnetic field-atom interaction, in which the laser light radiation force causes atoms to slow down. As temperature is a measure of kinetic energy which is the average speed of an ensemble of atoms (average thermal motion per atom), so slowing will result in cooling. Cold atoms have many benefits, including the elimination of the Doppler effect, an effective reduction in the collisional dephasing rate and offers low interaction of an atom with its environment leading to long coherence time. This section discusses the fundamental principles involved in laser cooling and trapping of atoms with regards to the magneto-optical trap (MOT).

The concept of laser cooling is based on the idea that when a resonant photon is absorbed by an atom then by conservation of momentum, its momentum is transferred to the atom. When a photon with momentum $p_r = \hbar k$ and frequency ω_{12}^{l} that is red detuned by Δ_{12} from the atomic resonance ω_{12} counter-propagates with an atom of momentum p, due to Doppler effect, the counter-propagating photon becomes closer to the atomic resonance ω_{12} and the photon is absorbed by the atom. The small momentum transfer due to absorption of a single photon changes the momentum of the atom by a recoil momentum given by p_r. The absorption is followed by a spontaneous emission process giving the atom another momentum transfer $p_r' = \hbar k'$ but in a completely random direction leading to no average momentum gain i.e., $< p_r' >= 0$. Therefore, the only reason the atom experiences a resultant momentum transfer is due to the absorption of photons. The sketch depicting Doppler cooling is presented in Fig. 2.4.

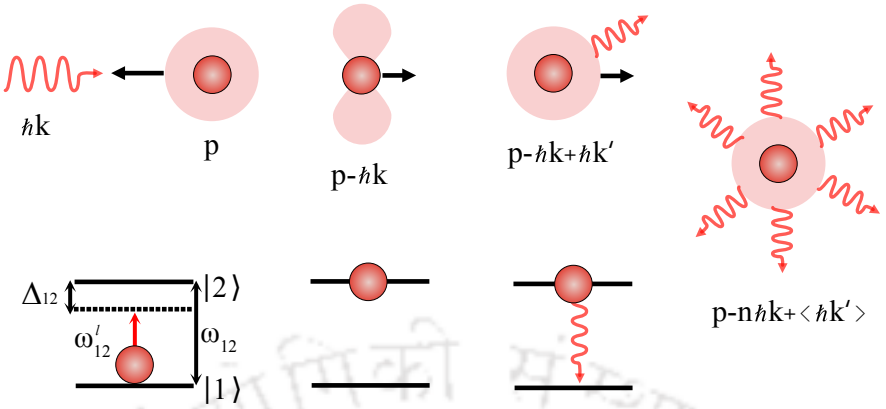

FIGURE 2.4: A sketch depicting a simplified Doppler cooling mechanism. p is the initial momentum of the atom, ω_{12} is atomic resonance, ω_{12}^{l} is the photon frequency, Δ_{12} is the detuning and n is the number of absorption and emission cycles.

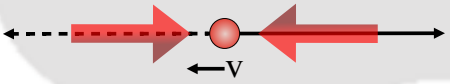

FIGURE 2.5: Schematic showing radiation force acting on the atom is directed along the laser beam.

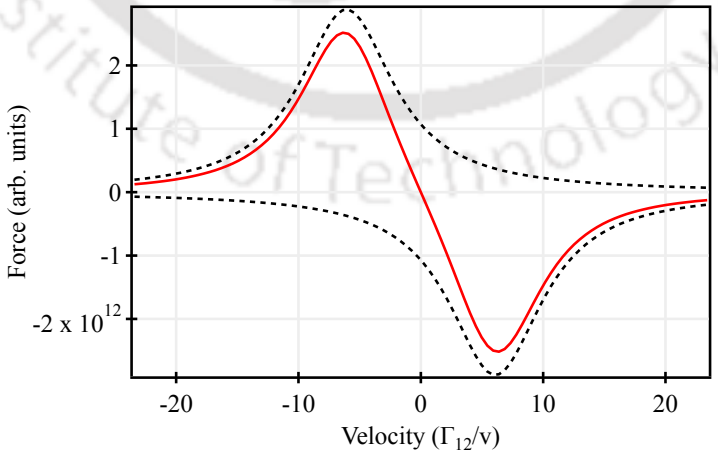

FIGURE 2.6: Radiation force vs velocity.

Consider a two-level atom moving with a velocity $\vec{v}$ counter-propagating with a laser beam of frequency ω_{12}^{l} detuned slightly below the atomic resonance ω_{12}, the radiation force exerted by a laser beam depends on the photon scattering rate $\Gamma_{\rm sc}$ given by

$$\vec{F} = \hbar\vec{k}\Gamma_{\rm sc}, \tag{2.42}$$

where

$$\Gamma_{\rm sc} = \frac{\Gamma_{12}S/2}{1+S+[2(\Delta_{12}-kv)/\Gamma_{12}]^2}. \tag{2.43}$$

Here, $S = I/I_s$ is the saturation parameter, I is the intensity of the laser, $I_s = \pi hc\Gamma/3\lambda^3$ is defined as the saturation intensity of the transition and $\Delta_{12} = (\omega_{12}^{l} - \omega_{12})$ is the detuning of the laser beam. Now, we introduce another laser beam but co-propagating with respect to the atom as shown in Fig. 2.5. Then the total radiation force exerted on the atom from the two beams is given by

$$\vec{F} = \vec{F}_{+} - \vec{F}_{-}, \tag{2.44}$$

where

$$\vec{F}_{\pm} = \pm\frac{\hbar\vec{k}\Gamma_{12}}{2}\frac{S}{1+S+[2(\Delta_{12}\mp kv)/\Gamma_{12}]^2}. \tag{2.45}$$

The forces exerted by the laser beams on the atom with respect to velocity is plotted in Fig. 2.6. The dashed lines are individual forces exerted by the laser beams and solid line is the resultant sum. It can be seen that the force acting on an atom is damping its movement for all velocities and it is linear around $v = 0$. For small velocities when $|kv| \ll \Gamma$ the above equation reduces to

$$\vec{F} \simeq \frac{8\hbar k^2\delta\vec{v}}{\Gamma[1+S+(2\delta/\Gamma)^2]^2}, \tag{2.46}$$

and in short it can be written as

$$\vec{F} \simeq -\beta\vec{v}, \tag{2.47}$$

which has the form of a damping force where $\beta = \dfrac{8\hbar k^2\delta}{\Gamma[1+S+(2\delta/\Gamma)^2]^2}$ is a damping constant and is responsible for cooling the atoms. Keeping in mind that the force can be either attractive or repulsive depending on the sign of detuning, cooling is possible for

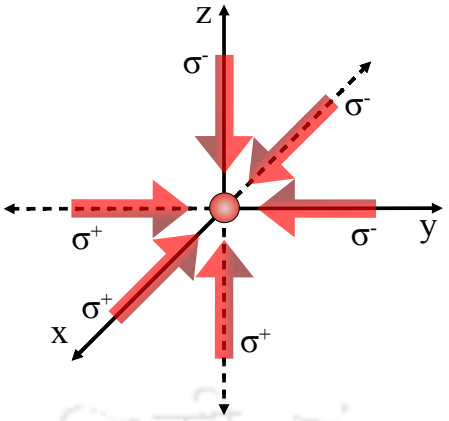

FIGURE 2.7: Schematic of optical molasses.

negative values of detuning, and in the opposite case, heating occurs and the atom gains energy. This effect can be extended to 3D, by using three orthogonal pairs of intersecting counter-propagating laser beams along three cartesian axes, causing cooling in all three directions as shown in Fig. 2.7. This configuration is often referred to as optical molasses (OM).

2.3.1 Doppler cooling limit

Each time an atom undergoes an absorption and emission cycle, it randomly gains momentum from photon recoil which leads to heating. This can be imagined as a random walk problem in momentum space. Although the mean momentum still averages to zero $< p_r >= 0$ but the mean square momentum which enters the kinetic energy is non-zero $< p_r'^2 >= 0$. The lowest kinetic energy is called the Doppler temperature or Doppler limit which results from an equilibrium between the cooling and heating processes. Using Eq. 2.47, the cooling rate at which the kinetic energy is lost due to the radiation force is given by

$$\left(\frac{dE}{dt}\right)_{\text{cooling}} = \vec{F}\vec{v} = -\beta v^2. \tag{2.48}$$

Now, the heating rate due to the random motion of atoms as a result of spontaneous emission of photons is given by

$$\left(\frac{dE}{dt}\right)_{\text{heating}} = \frac{1}{M}\frac{d}{dt} < p_r'^2 >= \frac{1}{M}\hbar^2 k^2 \Gamma_{\text{sc}}, \tag{2.49}$$

which depends on the total photon scattering rate given in Eq. 2.43 where we have considered for small velocities i.e., $|kv| \ll \Gamma_{12}$. At equilibrium, equating the heating and cooling rates

$$\left(\frac{dE}{dt}\right)_{\text{cooling}} = \left(\frac{dE}{dt}\right)_{\text{heating}}. \tag{2.50}$$

The expression for temperature is obtained and is expressed as

$$T = \frac{Mv^2}{3k_{\text{B}}} = \frac{\hbar\Gamma_{12}^2(1 + S + 4\Delta_{12}^2/\Gamma_{12}^2)}{8k_{\text{B}}\Delta_{12}}. \tag{2.51}$$

In the low intensity limit i.e., $S \ll 1$ and taking $\Delta_{12} = \Gamma_{12}/2$, the minimum temperature is given by

$$T_D \simeq \frac{\hbar\Gamma_{12}}{2k_{\text{B}}}, \tag{2.52}$$

where T_D is called the Doppler temperature. According to this limit the lowest temperature than can be achieved for Rb at 780 nm transition is 145.58 μK. However, temperatures below the Doppler limit have also been achieved in laboratories, and these results can be explained by sub-Doppler mechanisms like Sisyphus cooling [82, 83], grey molasses [84, 85] and evaporative cooling [86] which are outside the purview of this thesis.

2.3.2 Magneto optical trap

The mechanisms of Doppler cooling can reduce the temperature of the atoms but in order to trap the atoms, a position dependent force is needed. The configuration that can cool as well as trap the atoms is known as a Magneto-optical trap (MOT). The MOT is the most common tool to trap and cool neutral atoms. It employs three orthogonal pairs of intersecting counter-propagating laser beams for pushing the atoms into the center where they are subsequently trapped in a potential minimum created by a magnetic field as a result of the Zeeman shift.

To understand this mechanism, we will consider atoms in 1D MOT with two laser beams of opposite circular polarization (σ^+ and σ^-) detuned below resonance and counterpropagating along the z-axis in an inhomogeneous magnetic field of quadrupole symmetry B as shown in 2.8. For atomic transitions with a ground state F = 0 and excited state F

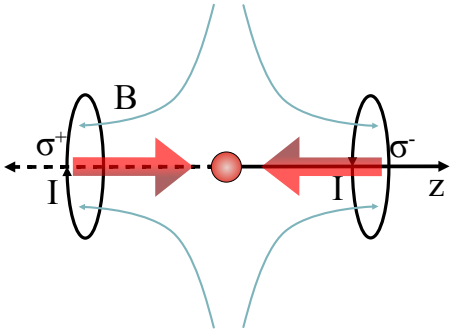

FIGURE 2.8: Schematic of MOT in 1D. Atoms in a magnetic field with quadrupole symmetry and two counterpropagating laser beams

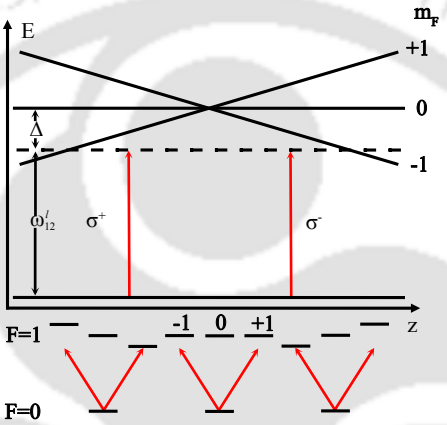

FIGURE 2.9: Schematic of the energy level shift in presence of a magnetic field gradient.

= 1, the excited state splits into three Zeeman components in presence of an inhomogeneous magnetic field and the sublevels splitting is linear with z as $B = B(z) = \frac{dB}{dz} \cdot z$ with zero at the center as shown in Fig. 2.9. For an atom on the left side of the trap, the magnetic field is negative and the beam from the left is σ^+ polarized, the sublevel $m_F = -1$ increases in energy, and the σ^+ light becomes resonant with the atomic resonance. As a result, momentum is transferred along the σ^+ beam towards the center of the trap. In this region, the counterpropagating σ^- beam is more detuned from the atomic resonance. This beam pushes the atom away from the center of the trap, but the momentum transfer is very small. For an atom on the right side of the trap, opposite happens where the sublevel $m_F = +1$ increases in energy. Thus, the total force acting on the atom is the sum of the forces exerted by both the beams. The above equation of

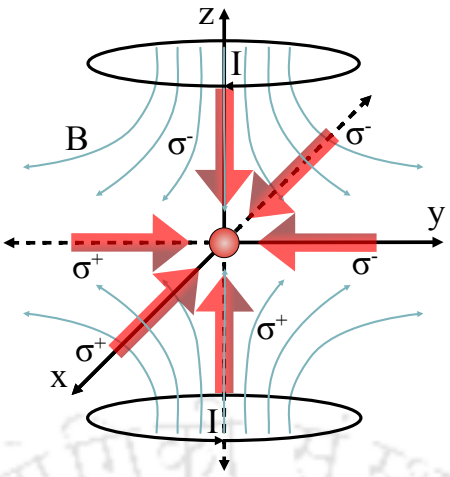

FIGURE 2.10: Schematic of a 3D MOT showing the six laser beams and current I flowing in opposite directions generate magnetic field of spherical quadrupole symmetry.

force in 2.45 can be modified by including position dependent detuning term as

$$\vec{F}_{\pm} = \pm\frac{\hbar\vec{k}\Gamma_{12}}{2}\frac{S}{1+S+[2(\Delta_{12}\mp kv\mp\mu B/\hbar)/\Gamma_{12}]^2}, \tag{2.53}$$

where $\mu = g_F m_F \mu_B$ is the magnetic moment, g_F is the Landé factor and $\mu B/\hbar$ is the Zeeman shift. With the assumption that the Doppler shift and the Zeeman shift are very small compared to Γ_{12} i.e, $|kv| \ll \Gamma_{12}$ and $\mu B/\hbar \ll \Gamma_{12}$, the above equation can be approximated as

$$\vec{F}_{\text{MOT}} \simeq -\beta\vec{v} - \alpha\vec{z}, \tag{2.54}$$

where $\alpha = \dfrac{\partial B}{\partial z}\dfrac{\mu'\beta}{\hbar k}$ is a damping constant. The coefficient of $\vec{v}$ shows a dissipative force and coefficient of z shows a restoring force which trap the atoms. The 1D MOT can be generalized to 3D as shown in the Fig. 2.10 where the atoms are subjected to three pairs of counterpropagating laser beams along three Cartesian axes under a magnetic field with a spherical quadrupole symmetry with gradient along the z-axis.

2.4 Rubidium structure

In this section, we provide a brief discussion on the Rb structure as the work in this thesis is based on the Rb atomic medium. The relevant energy level diagram is as shown in the Fig. 2.11 with fine and hyperfine structures. Rb has two stable isotopes with a natural abundance of 72% for ^{85}Rb and 28% for ^{87}Rb, respectively. It is one of the atomic species that is most commonly used in experiments in atomic physics laser cooling and trapping experiments for its requirement of relatively low temperatures to produce high vapour pressures and easily available inexpensive diode laser at the required wavelength.

2.4.1 Fine structure

The fine structure results from the coupling of the orbital angular momentum **L** of the outermost electron with its spin angular momentum **S** and is characterized by the total electron angular momentum **J** which is expressed as

$$\mathbf{J} = \mathbf{L} + \mathbf{S}, \tag{2.55}$$

where **J** can take values between $|L-S| \leq J \leq |L+S|$, the magnitude of **J** is $\sqrt{J(J+1)}\hbar$ and the eigen value of J_z is $m_J\hbar$. For the case of ^{87}Rb, S=1/2 and at ground state L=0 so J=1/2; at excited state L=1 so J=1/2, 3/2. Therefore, the shift in the energy level is according to the value of J, such that the D line at L=0 $\rightarrow$ L=1 transition split into two components i.e., the D_1 and D_2 lines. The $5^2S_{1/2} \rightarrow 5^2P_{1/2}$ at 794.760 nm and $5^2S_{1/2} \rightarrow 5^2P_{3/2}$ at 780.027 nm transitions are the components of a fine-structure doublet, D1 and D2 respectively [1, 2]. The $5^2S_{1/2} \rightarrow 6^2P_{1/2}$ at 421.673 nm and $6^2S_{1/2} \rightarrow 5^2P_{3/2}$ at 420.298 nm transitions are the components of another fine-structure doublet, D1 and D2 respectively [3] as shown in the Fig. 2.11.

2.4.2 Hyperfine structure

The hyperfine structure results from the coupling of the total electron angular momentum **J** with the total nuclear angular momentum **I** and is characterized by the total atomic

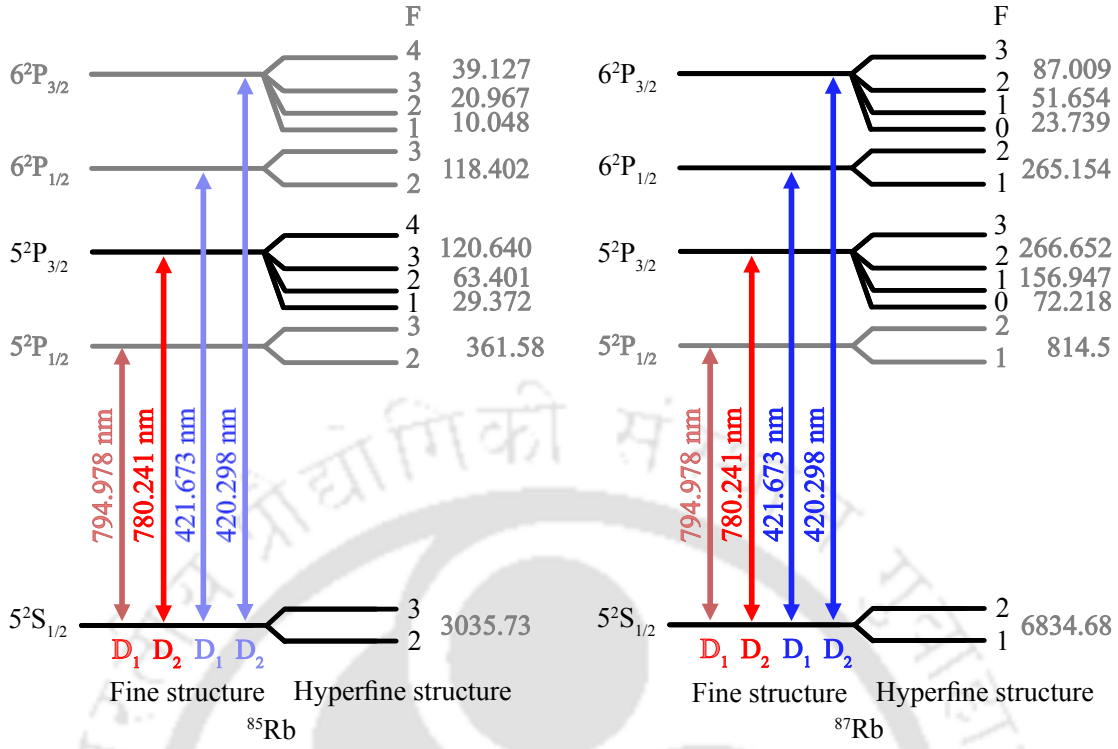

FIGURE 2.11: The relevant energy level diagram of ^{85}Rb and ^{87}Rb with the Fine and Hyperfine structures[1–3].

angular momentum **F** which is expressed as

$$\mathbf{F} = \mathbf{I} + \mathbf{J}. \tag{2.56}$$

where F can take values between $|I - J| \leq F \leq |I + J|$. For the case of ^{87}Rb, ground state J=1/2 and I=3/2, so F=1,2; at excited state of D_1 line ($5^2P_{1/2}$) F=1,2 and D_2 ($5^2P_{3/2}$) line F=0, 1, 2, 3. Again, the shift in the energy level is according to the value of F. The Hamiltonian which describes the hyperfine structure is

$$H_{\text{hfs}} = A_{\text{hfs}}\mathbf{I}\cdot\mathbf{J} + B_{\text{hfs}}\frac{3(\mathbf{I}\cdot\mathbf{J})^2 + \frac{3}{2}I\cdot J - I(I+1)J(J+1)}{2I(2I+1)J(2J-1)}, \tag{2.57}$$

which gives us the hyperfine energy level shift as

$$\Delta E_{\text{hfs}} = \frac{1}{2}A_{\text{hfs}}K + B\frac{\frac{3}{2}K(K+1) - 2I(I+1)J(J+1)}{2I(2I+1)2J(2J-1)}, \tag{2.58}$$

where

$$K = F(F+1) - I(I+1) - J(J+1). \tag{2.59}$$

where $A_{\rm hfs}$ is the magnetic dipole coupling constant and B_{hfs} is the electric quadrupole coupling constant which applies only to the excited manifold of the D_2 transition and not to the levels with J=1/2. The hyperfine energy level diagram of ^{85}Rb and ^{85}Rb is shown in Fig. 2.11.

2.4.3 Zeeman Splitting

The hyperfine energy levels break into Zeeman components under magnetic fields, and each hyperfine level contains $2F+1$ magnetic sublevels. The Hamiltonian which describes the atomic interactions in presence of a magnetic field is given by

$$\begin{aligned} H_B =& \frac{\mu_{\rm B}}{\hbar}(g_S\mathbf{S} + g_L\mathbf{L} + g_I\mathbf{I})\cdot\mathbf{B} \\ =& \frac{\mu_{\rm B}}{\hbar}(g_S S_z + g_L L_z + g_I I_z)B_z, \end{aligned}$$

where $\mu_{\rm B}$ is the Bohr magneton, g_S, g_L and g_I are the g-factors of the electron spin, electron orbital angular momentum and nuclear spin respectively. Here, the magnetic field is taken along z which is the quantization axis.

If the energy level shift is small compared to the fine structure splitting then J will be a good quantum number and the above interaction Hamiltonian reduces to

$$H_B = \frac{\mu_{\rm B}}{\hbar}(g_J J_z + g_I I_z)B_z \tag{2.60}$$

where g_J the Landé g-factor is given by

$$\begin{aligned} g_J =& g_L\frac{J(J+1) - S(S+1) + L(L+1)}{2J(J+1)} + g_S\frac{J(J+1) + S(S+1) - L(L+1)}{2J(J+1)} \\ \simeq& 1 + g_S\frac{J(J+1) + S(S+1) - L(L+1)}{2J(J+1)} \end{aligned} \tag{2.61}$$

Similarly, if energy level shift due to the magnetic field is small compared to the hyperfine splitting, then F will be a good quantum number so the above interaction Hamiltonian

now becomes

$$H_B = \mu_B g_F F_z B_z, \tag{2.62}$$

where the hyperfine Landé g-factor is defined as,

$$g_F = g_J \frac{F(F+1) - I(I+1) + J(J+1)}{2F(F+1)} + g_I \frac{F(F+1) + I(I+1) - I(I+1)}{2F(F+1)} \tag{2.63}$$

$$= g_J \frac{F(F+1) - I(I+1) + J(J+1)}{2F(F+1)}. \tag{2.64}$$

The nuclear term g_I is neglected as it much smaller than the g_J. For small fields the interaction Hamiltonian in described by Eq. 2.62 and the energy shift in this regime is called the anomalous Zeeman effect. For sufficiently strong fields the hyperfine Hamiltonian is negligible compared to the interaction Hamiltonian, then the effect is termed as Normal Zeeman effect for hyperfine structure. For even stronger fields the interaction is described by Eq. 2.60 and the energy shift in this regime is called the Paschen-Back effect [87].

Chapter 3

Highly sensitive atomic based MW interferometry

THIS chapter outlines the theoretically study of a scheme to develop an atomic based micro-wave (MW) interferometry using the Rydberg states in Rb. This system has great advantage due to its much higher frequency range in comparison to the electrical circuit, ranging from radio frequency (RF), MW to terahertz regime. In addition, this is two **orders of magnitude** more sensitive to field strength as compared to the prior demonstrations on the MW electrometry using the Rydberg atomic states. Further, previously studied atomic systems are only sensitive to the field strength but not to the phase and hence this scheme provides a great opportunity to characterize the MW completely including the propagation direction and the wavefront. The atomic based MW interferometry is based upon a six-level loopy ladder system involving the Rydberg states in which two sub-systems interfere constructively or destructively depending upon the phase between the MW electric fields closing the loop. This work opens up a new field i.e. atomic based MW interferometry replacing the conventional electrical circuit in much superior fashion.

3.1 Introduction

Atomic based standards such as time and length is already adopted and established due to their high reproducibility, accuracy, resolution and stability [88]. Atoms have also been successfully used for DC and AC (MW and RF) magnetometry, reaching impressive sensitivity and spatial resolutions [28–31]. Inspired by these successes recently, the atom based MW and RF electrometry has been investigated using the Rydberg states of the atoms [48–53]. The success of these experiments for high sensitive electrometry is due to property of the Rydberg states i.e. availability of closely spaced levels (in the range of MW and RF region) with very high electric polarizability. The traditional antenna method can detect MW fields as low as 10 mVcm^{-1} [55, 56]. However, by utilizing the optical method for the electro-magnetic fields converted by dipole antenna, the sensitivity increases significantly, allowing for a minimum detectable field of up to 30 $\mu\mathrm{Vcm}^{-1}$ and sensitivity of 1 $\mu\mathrm{Vcm}^{-1}\mathrm{Hz}^{-1/2}$ [49, 57]. The atomic-based MW sensor improves the sensitivity further up to 30 $\mu\mathrm{Vcm}^{-1}\mathrm{Hz}^{-1/2}$ with a minimum detectable field of 8 $\mu\mathrm{Vcm}^{-1}$ [49] which is limited by the natural decay rate of the ground and the Rydberg states, lasers linewidth, the transit time broadening, and Doppler mismatch between probe and the control lasers. The transit time broadening can be removed completely using the cold atomic cloud, cold atomic beam [89], or nano cell [90]. The Doppler mismatch between probe and the control laser can be removed using the cold atom, nano cell or collimated atomic beam. However, with very simple experimental set-up with Rb cell at room temperature, the strength sensitivity of experimentally demonstrated four level system [49] is already three orders of magnitude better than the electrical circuit based MW sensor. Further the frequency range of the atomic based MW sensor is from radio frequency (RF), MW to terahertz regime. Next, the spatial resolution of the atomic based MW sensor is sub-wavelength ($\lambda_{MW}/650$) [58] which is difficult to achieve with traditional antenna method as the dimension of the antenna itself happens to be $\lambda_{MW}/2$.

The atomic based electrometry is based upon the phenomenon of electromagnetically induced transparency (EIT) in which the absorption property of a probe laser is altered

in the presence of control lasers and MW (or RF) field in a four level system. EIT is sensitive to the field's strength, frequency and the polarization and so the electrometry.

An oscillating electro-magnetic field i.e. MW electric field is characterized by its strength-/amplitude, frequency, polarization and the phase. The previously studied atomic based MW electrometry is not phase sensitive as EIT in a simple multi-level system, happens to be insensitive to the absolute phase of probe and the control fields but only it's robustness depends upon the phase stability [91].

Phase of the MW fields is detected using traditional MW interferometry which is based upon the electrical circuit [92–94]. Here, we explore a six-level loopy ladder system which replaces the traditional electrical circuits based MW interferometry by the atomic MW interferometry, as the absorption property of the probe laser has phase dependency on the MW fields. This is based upon the interference between two sub-systems driven by the MW fields forming the loop. The limitation of the atomic based MW interferometry is again same as in case of the atomic based MW sensor studied with four-level system [48, 49]. But this system is two orders of magnitude more sensitive to field strength (up to 80 nV/cm) in comparison to the previously explored system [48, 49] due to its loopy nature. There are loopy system which has been studied previously and has phase sensitivity but loop is completed using the weak magnetic dipole transition [95]. In contrast to the previous system this six-level loopy system involves allowed electric dipole transition.

This chapter is organized as follows. In the section 3.2, we describe the method of realizing the six-level loopy ladder system in Rb and possible experimental set-up. In subsequent sub-section we present the semi-classical model and solution for the relevant density matrix element. Further we provide the physical interpretation of the obtained mathematical solution in terms of the interference between the two sub-systems and in terms of the dressed state picture. In the next section 3.3, we present various results including the lineshape of the probe absorption, the phase dependency of it, the comparison of the amplitude/strength sensitivity of this system with the previously studied four-level system and the frequency range. Finally in section 3.4, we give our conclusion for this study.

3.2 Method

3.2.1 Realization of the system

The considered six-level loopy ladder system is shown in Fig. 3.1a. The probe laser at 780 nm is at the D_2 line i.e. driving the $5S_{1/2} \rightarrow 5P_{3/2}$ transition in the Rb. The control laser at 480 nm is driving the $5P_{3/2} \rightarrow n^1_{ryd}S$ and the three reference MW fields are driving the transition, $n^1_{ryd}S \rightarrow n^2_{ryd}P$, $n^2_{ryd}P \rightarrow n^3_{ryd}S$ and $n^3_{ryd}S \rightarrow n^4_{ryd}P$. The unknown MW field is driving the $n^1_{ryd}S \rightarrow n^4_{ryd}P$. The n^1_{ryd}, n^2_{ryd}, n^3_{ryd} and n^4_{ryd} are Rydberg states which are chosen according to the frequency range of the MW field.

The typical experimental set-up for phase dependent MW electrometry is shown in Fig.3.1(c) in which a probe laser at 780 nm and a control laser at 480 nm are counter-propagating inside the Rb cell. The four MW control fields are generated by a single frequency synthesizer having arrangements of controlling the frequency, phase and the amplitude or the four different MW field frequencies combined using a frequency combiner (e.g. ZN4PD-02183-S+ from minicircuit company can be operated between 2 GHz-18 GHz). The output of the frequency synthesizer or combiner is amplified and fed to MW horn. All four MW fields are propagating perpendicular to the probe and the control lasers with a uniform phase inside the Rb cell.

3.2.2 Semi-classical analysis

The electric field, associated with the transition $|i\rangle \rightarrow |j\rangle$ is $E_{ij}e^{i(\omega_{ij}t+\phi_{ij})}$, where E_{ij} is amplitude, ω_{ij} is the frequency and ϕ_{ij} is the phase. We define Rabi frequency $\Omega_{ij} = d_{ij}E_{ij}e^{i\phi_{ij}}/\hbar$ for the transition $|i\rangle \rightarrow |j\rangle$ having the dipole moment matrix element d_{ij}. Please note that Ω_{ij} is a complex quantity which can be written as $|\Omega_{ij}|\ e^{i\phi_{ij}}$, where ϕ_{ij} is due to the phase of the electric field associated with it. The Rabi frequencies of the probe and the control lasers are Ω_{12} and Ω_{23} respectively, whereas Ω^{ref}_{34}, Ω^{ref}_{45}, Ω^{ref}_{56} and Ω^{unk}_{36} are the Rabi frequencies of the MW fields. It is important to note here that the phase of Ω^{unk}_{36} is to be characterized w.r.t to the reference MW fields Ω^{ref}_{34}, Ω^{ref}_{45} and Ω^{ref}_{56}. The superscript ref or unk denotes the reference and unknown MW field respectively.

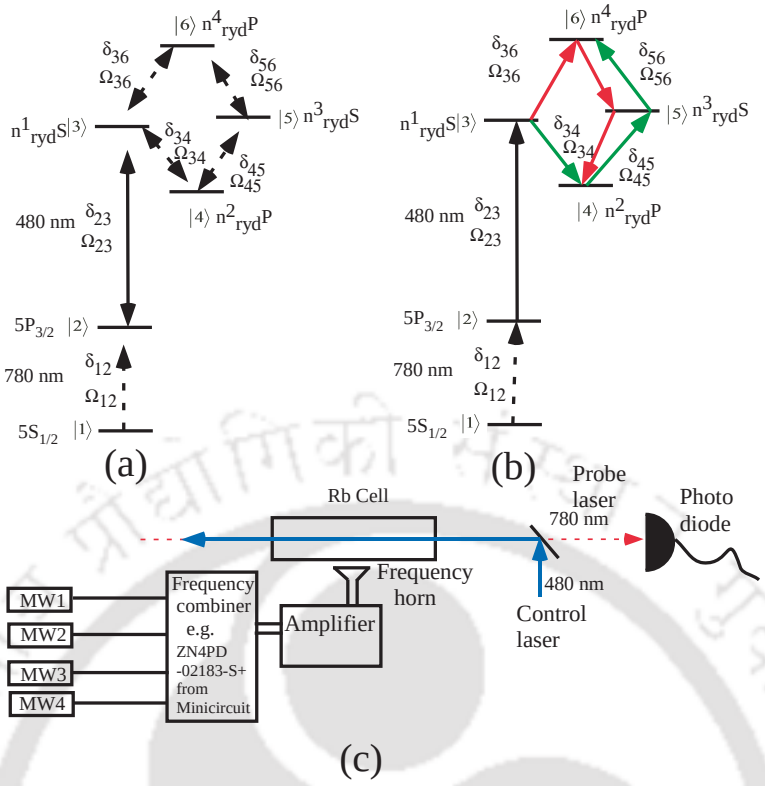

FIGURE 3.1: (a) The energy level diagram for loopy ladder system. (b) Transitions shown by the red and green arrow lines are the two sub-system to close the loop. The probe laser (dotted red arrow line) and the control laser (solid blue arrow line) are part of both the sub-system. (c) The typical experimental set up for the phase dependent MW electrometry.

The total Hamiltonian for this system is given as

$$
\begin{aligned}
H = \Bigg[& \sum_{i=1}^{2} \frac{\hbar\Omega_{i,i+1}}{2} \left(e^{i\omega_{i,i+1}t} + e^{-i\omega_{i,i+1}t}\right) |i\rangle \langle i+1| \\
& + \sum_{i=3}^{5} \frac{\hbar\Omega^{\text{ref}}_{i,i+1}}{2} \left(e^{i\omega_{i,i+1}t} + e^{-i\omega_{i,i+1}t}\right) |i\rangle \langle i+1| \\
& + \frac{\hbar\Omega^{\text{unk}}_{36}}{2} \left(e^{i\omega_{36}t} + e^{-i\omega_{36}t}\right) |3\rangle \langle 6| + h.c. \Bigg] + \sum_{j=1}^{6} \hbar\omega_j |j\rangle \langle j|
\end{aligned} \tag{3.1}
$$

If the energy of the state $|i\rangle$ is $\hbar\omega_i$ then the general quantum mechanical state of the system is

$$
|\Psi\rangle = \sum_{i-1}^{6} c_i(t) |i\rangle e^{-i\omega_i t} \tag{3.2}
$$

We define $\delta_{12} = \omega_{12} - (\omega_2 - \omega_1)$ and $\delta_{23} = \omega_{23} - (\omega_3 - \omega_2)$ i.e. the detunings of the probe and control lasers from their respective resonance. Similarly, $\delta_{34} = \omega_{34} - (\omega_3 - \omega_4)$, $\delta_{45} = \omega_{45} - (\omega_5 - \omega_4)$, $\delta_{56} = \omega_{56} - (\omega_6 - \omega_5)$ and $\delta_{36} = \omega_{36} - (\omega_6 - \omega_3)$ are the detunings for the MW fields for the respective transitions. In the rotating frame (i.e with a unitary transformation $c_1 = c_1; c_2' = c_2 e^{i\delta_{12}t}; c_3' = c_3 e^{i(\delta_{12}+\delta_{23})t}; c_4' = c_4 e^{i(\delta_{12}+\delta_{23}-\delta_{34})t}; c_5' = c_5 e^{i(\delta_{12}+\delta_{23}-\delta_{34}+\delta_{45})t}; c_6' = c_6 e^{i(\delta_{12}+\delta_{23}-\delta_{34}+\delta_{45}+\delta_{56})t}$) and using the rotating wave approximation, (where the terms with $e^{i[\omega_{ij}+(\omega_j-\omega_i)]}$ is dropped out for the transition $|i\rangle \rightarrow |j\rangle$ if $\omega_j > \omega_i$) we get following Hamiltonian

$$\begin{aligned} H = \hbar\Big[& 0\,|1\rangle\langle 1| - \delta_{12}\,|2\rangle\langle 2| - (\delta_{12}+\delta_{23})\,|3\rangle\langle 3| - (\delta_{12}+\delta_{23}-\delta_{34})\,|4\rangle\langle 4| \\ & - (\delta_{12}+\delta_{23}-\delta_{34}+\delta_{45})\,|5\rangle\langle 5| - (\delta_{12}+\delta_{23}-\delta_{34}+\delta_{45}+\delta_{56})\,|6\rangle\langle 6| \\ & + \frac{\Omega_{12}}{2}\,|1\rangle\langle 2| + \frac{\Omega_{23}}{2}\,|2\rangle\langle 3| + \frac{\Omega_{34}^{\text{ref}}}{2}\,|3\rangle\langle 4| + \frac{\Omega_{45}^{\text{ref}}}{2}\,|4\rangle\langle 5| + \frac{\Omega_{56}^{\text{ref}}}{2}\,|5\rangle\langle 6| \\ & + \frac{\Omega_{36}^{\text{unk}}}{2} e^{i(\delta_{34}-\delta_{45}-\delta_{56}+\delta_{36})t}\,|3\rangle\langle 6| + h.c.\Big] \end{aligned} \tag{3.3}$$

In general, the Hamilitonian H is time dependent except for a particular condition when $\delta_{34} - \delta_{45} - \delta_{56} + \delta_{36} = 0$.

The time evolution of the density matrix, ρ is given by Linblad master equation as

$$\dot{\rho} = -\frac{i}{\hbar}[H, \rho] + L[\rho(t)] \tag{3.4}$$

where, $L[\rho(t)]$ is Linblad matrix and defined as below. $L[\rho(t)] =$

$$\begin{bmatrix} \Gamma_{21}\rho_{22} & -\frac{\gamma_{12}^{dec}}{2}\rho_{12} & -\frac{\gamma_{13}^{dec}}{2}\rho_{13} & -\frac{\gamma_{14}^{dec}}{2}\rho_{14} & -\frac{\gamma_{15}^{dec}}{2}\rho_{15} & -\frac{\gamma_{16}^{dec}}{2}\rho_{16} \\ -\frac{\gamma_{12}^{dec}}{2}\rho_{21} & -\Gamma_{21}\rho_{22} + \Gamma_{32}\rho_{33} & -\frac{\gamma_{23}^{dec}}{2}\rho_{23} & -\frac{\gamma_{24}^{dec}}{2}\rho_{24} & -\frac{\gamma_{25}^{dec}}{2}\rho_{25} & -\frac{\gamma_{26}^{dec}}{2}\rho_{26} \\ -\frac{\gamma_{13}^{dec}}{2}\rho_{31} & -\frac{\gamma_{23}^{dec}}{2}\rho_{32} & -\Gamma_{32}\rho_{33} - \Gamma_{34}\rho_{33} + \Gamma_{63}\rho_{66} & -\frac{\gamma_{34}^{dec}}{2}\rho_{34} & -\frac{\gamma_{35}^{dec}}{2}\rho_{35} & -\frac{\gamma_{36}^{dec}}{2}\rho_{36} \\ -\frac{\gamma_{14}^{dec}}{2}\rho_{41} & -\frac{\gamma_{24}^{dec}}{2}\rho_{42} & -\frac{\gamma_{34}^{dec}}{2}\rho_{43} & \Gamma_{34}\rho_{33} - \Gamma_4\rho_{44} & -\frac{\gamma_{45}^{dec}}{2}\rho_{45} & -\frac{\gamma_{46}^{dec}}{2}\rho_{46} \\ -\frac{\gamma_{15}^{dec}}{2}\rho_{51} & -\frac{\gamma_{25}^{dec}}{2}\rho_{52} & -\frac{\gamma_{35}^{dec}}{2}\rho_{53} & -\frac{\gamma_{45}^{dec}}{2}\rho_{54} & -\Gamma_5\rho_{55} & -\frac{\gamma_{56}^{dec}}{2}\rho_{56} \\ -\frac{\gamma_{16}^{dec}}{2}\rho_{61} & -\frac{\gamma_{26}^{dec}}{2}\rho_{62} & -\frac{\gamma_{36}^{dec}}{2}\rho_{63} & -\frac{\gamma_{46}^{dec}}{2}\rho_{64} & -\frac{\gamma_{56}^{dec}}{2}\rho_{65} & -\Gamma_6\rho_{66} \end{bmatrix} \tag{3.5}$$

Where, Γ_{ij} is the decay of the population from state $|i\rangle$ ($i = 1, 2,..$ to 6) to state $|j\rangle$ ($j = 1, 2,..$ 6) and Γ_i is the total population decay rate of state $|i\rangle$. In the case of the weak probe, the population transfer does not take place and it is completely irrelevant to

know the population dynamics between different levels. The only important parameter is Γ_i and Γ_j, i.e.the total decay rate of states, which governs the decoherence rate (γ_{ij}^{dec}) between the two levels $|i\rangle$ and $|j\rangle$ as $\gamma_{ij}^{dec} = \frac{\Gamma_i+\Gamma_j}{2}$. In addition to the total decay rate of states, the linewidth of lasers driving the transition has to be also included for γ_{ij}^{dec}. For example, in this study we take the value of $\gamma_{12}^{dec} = 2\pi\times3.05$ MHz, which includes natural radiative decay of excited state, $\Gamma_2 = 2\pi\times6$MHz [96] and the 780nm laser linewidth of $2\pi\times50$kHz. We also take $\gamma_{13}^{dec} = \gamma_{14}^{dec} = \gamma_{15}^{dec} = \gamma_{16}^{dec} = \gamma^{dec} = 2\pi\times100$kHz mainly dominated by the laser linewidths of 780nm and the 480nm as compared to the radiative decay rate (=$2\pi\times1$kHz) of the Rydberg states $|3\rangle$, $|4\rangle$, $|5\rangle$ and $|6\rangle$ [50]. We also take $\gamma^{dec} = 2\pi\times500$kHz in some cases in order to check it's stringency.

From Eq. 4.1, 4.2 and 3.5 we get 36 coupled differential equations with the property $\rho_{ij} = \rho_{ji}^*$. In order to solve these set of coupled equation we adapt similar method as in the case of previously studied multi-level systems [97].

In the case of weak probe approximation, there will be no population transfer and hence the time evolution of the population i.e. the diagonal terms of the density matrix such as ρ_{11}, ρ_{22}, ρ_{33}, ρ_{44}, ρ_{55}, and ρ_{66} can be ignored. Similarly, the time evolution of the off-diagonal terms ρ_{ij} for $i = 2; j = 3,4,5,6$ and $i = 3; j = 4,5,6$ and $i = 4; j = 5,6$ and $i = 5; j = 6$ can be also ignored. The time evolution of the relevant density matrix element is given below.

$$
\begin{aligned}
\dot{\rho}_{12} &= i\frac{\Omega_{12}}{2}(\rho_{11}-\rho_{22}) + i\frac{\Omega_{23}^*}{2}\rho_{13} - \gamma_{12}\rho_{12} \qquad (3.6)\\
\dot{\rho}_{13} &= -i\frac{\Omega_{12}}{2}\rho_{23} + i\frac{\Omega_{23}}{2}\rho_{12} + i\frac{\Omega_{34}^{\mathrm{ref}*}}{2}\rho_{14} + i\frac{\Omega_{36}^{\mathrm{unk}*}}{2}e^{-i(\delta_{34}-\delta_{45}-\delta_{56}+\delta_{36})t}\rho_{16} - \gamma_{13}\rho_{13}\\
\dot{\rho}_{14} &= -i\frac{\Omega_{12}}{2}\rho_{24} + i\frac{\Omega_{34}^{\mathrm{ref}}}{2}\rho_{13} + i\frac{\Omega_{45}^{\mathrm{ref}*}}{2}\rho_{15} - \gamma_{14}\rho_{14}\\
\dot{\rho}_{15} &= -i\frac{\Omega_{12}}{2}\rho_{25} + i\frac{\Omega_{45}^{\mathrm{ref}}}{2}\rho_{14} + i\frac{\Omega_{56}^{\mathrm{ref}*}}{2}\rho_{16} - \gamma_{15}\rho_{15}\\
\dot{\rho}_{16} &= -i\frac{\Omega_{12}}{2}\rho_{26} + i\frac{\Omega_{36}^{\mathrm{unk}}}{2}e^{i(\delta_{34}-\delta_{45}-\delta_{56}+\delta_{36})t}\rho_{13} + i\frac{\Omega_{56}^{\mathrm{ref}}}{2}\rho_{15} - \gamma_{16}\rho_{16}
\end{aligned}
$$

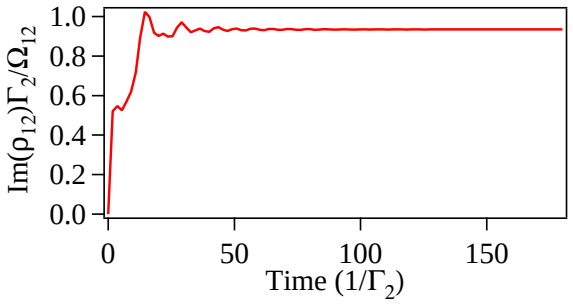

FIGURE 3.2: The normalized absorption, $\rho_{12}\Gamma_2/\Omega_{12}$ vs Time for $\Omega_{23} = \Omega_{34}^{\text{ref}} = \Omega_{45}^{\text{ref}} = \Omega_{56}^{\text{ref}} = \Gamma_2$, $\Omega_{36}^{\text{ukn}} = 0.5\Gamma_2$ and $\delta_{12} = \delta_{23} = \delta_{34} = \delta_{45} = \delta_{56} = \delta_{36} = 0$.

Where, $\gamma_{12} = \left[\gamma_{12}^{dec} + i\delta_{12}\right]$,

$\gamma_{13} = \left[\gamma_{13}^{dec} + i\left(\delta_{12} + \delta_{23}\right)\right]$,

$\gamma_{14} = \left[\gamma_{14}^{dec} + i\left(\delta_{12} + \delta_{23} - \delta_{34}\right)\right]$,

$\gamma_{15} = \left[\gamma_{15}^{dec} + i\left(\delta_{12} + \delta_{23} - \delta_{34} + \delta_{45}\right)\right]$,

$\gamma_{16} = \left[\gamma_{16}^{dec} + i\left(\delta_{12} + \delta_{23} - \delta_{34} + \delta_{45} + \delta_{56}\right)\right]$.

Now, we apply the four-photon resonance condition for the MW fields i.e. $\delta_{34} - \delta_{45} - \delta_{56} + \delta_{36} = 0$. In this case the system will reach steady state i.e. $\dot{\rho_{ij}} = 0$, for all the elements on the time scale of few tens of $1/\Gamma_2$ as shown in Fig. 3.2. In the weak probe condition and in the steady state, $\rho_{11} \approx 1$, $\rho_{22} \approx \rho_{33} \approx \rho_{44} \approx \rho_{55} \approx \rho_{66} \approx 0$ and $\rho_{ij}{=}\rho_{ji} \approx 0$ for $i = 2; j = 3, 4, 5, 6$ and $i = 3; j = 4, 5, 6$ and $i = 4; j = 5, 6$ and $i = 5; j = 6$. Finally, we get the following set of equations

$$
\begin{aligned}
\rho_{12} &= \frac{i}{2}\frac{\Omega_{12}}{\gamma_{12}} + \frac{i}{2}\frac{\Omega_{23}^{*}}{\gamma_{12}}\rho_{13} \\
\rho_{13} &= \frac{i}{2}\frac{\Omega_{23}}{\gamma_{13}}\rho_{12} + \frac{i}{2}\frac{\Omega_{34}^{\text{ref}*}}{\gamma_{13}}\rho_{14} + \frac{i}{2}\frac{\Omega_{36}^{\text{unk}*}}{\gamma_{13}}\rho_{16} \\
\rho_{14} &= \frac{i}{2}\frac{\Omega_{34}^{\text{ref}}}{\gamma_{14}}\rho_{13} + \frac{i}{2}\frac{\Omega_{45}^{\text{ref}*}}{\gamma_{14}}\rho_{15} \\
\rho_{15} &= \frac{i}{2}\frac{\Omega_{45}^{\text{ref}}}{\gamma_{15}}\rho_{14} + \frac{i}{2}\frac{\Omega_{56}^{\text{ref}*}}{\gamma_{15}}\rho_{16} \\
\rho_{16} &= \frac{i}{2}\frac{\Omega_{36}^{\text{unk}}}{\gamma_{16}}\rho_{13} + \frac{i}{2}\frac{\Omega_{56}^{\text{ref}}}{\gamma_{16}}\rho_{15}
\end{aligned}
\tag{3.7}
$$

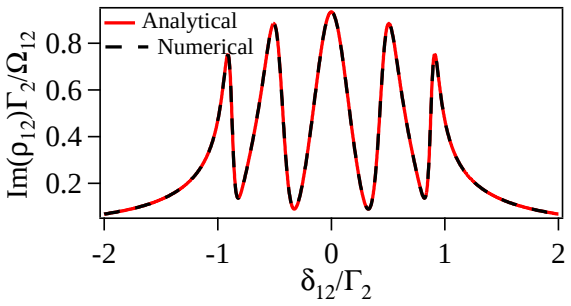

FIGURE 3.3: Comparison of complete numerical solution with the analytical solution for the normalized absorption ($\mathrm{Im}(\rho_{12})\Gamma_2/\Omega_{12}$) vs δ_{12}/Γ_2 of the probe laser with $|\Omega_{23}| = |\Omega_{34}^{\mathrm{ref}}| = |\Omega_{45}^{\mathrm{ref}}| = |\Omega_{56}^{\mathrm{ref}}| = \Gamma_2$, $|\Omega_{36}^{\mathrm{unk}}| = 0.5\Gamma_2$, $\phi = 0$ and $\delta_{23} = \delta_{34} = \delta_{45} = \delta_{56} = \delta_{36} = 0$.

The above equation gives solution for ρ_{12} as

$$\rho_{12} = \frac{\frac{i}{2}\frac{\Omega_{12}}{\gamma_{12}}}{1 + \frac{\frac{1}{4}\frac{|\Omega_{23}|^2}{\gamma_{12}\gamma_{13}}}{1+\mathrm{EITATA1}+\mathrm{EITATA2}+\mathrm{Int}}}$$

Where,

$$\mathrm{EITATA1} = \frac{\frac{1}{4}\frac{|\Omega_{34}^{\mathrm{ref}}|^2}{\gamma_{13}\gamma_{14}}}{1 + \frac{\frac{1}{4}\frac{|\Omega_{45}^{\mathrm{ref}}|^2}{\gamma_{14}\gamma_{15}}}{1+\frac{1}{4}\frac{|\Omega_{56}^{\mathrm{ref}}|^2}{\gamma_{15}\gamma_{16}}}}; \mathrm{EITATA2} = \frac{\frac{1}{4}\frac{|\Omega_{36}^{\mathrm{unk}}|^2}{\gamma_{13}\gamma_{16}}}{1 + \frac{\frac{1}{4}\frac{|\Omega_{56}^{\mathrm{ref}}|^2}{\gamma_{15}\gamma_{16}}}{1+\frac{1}{4}\frac{|\Omega_{45}^{\mathrm{ref}}|^2}{\gamma_{14}\gamma_{15}}}};$$

$$\mathrm{Int} = -\frac{\frac{1}{8}\frac{|\Omega_{34}^{\mathrm{ref}}||\Omega_{45}^{\mathrm{ref}}||\Omega_{56}^{\mathrm{ref}}||\Omega_{36}^{\mathrm{unk}}|cos(\phi)}{\gamma_{13}\gamma_{14}\gamma_{15}\gamma_{16}}}{1 + \frac{1}{4}\frac{|\Omega_{45}^{\mathrm{ref}}|^2}{\gamma_{14}\gamma_{15}} + \frac{1}{4}\frac{|\Omega_{56}^{\mathrm{ref}}|^2}{\gamma_{15}\gamma_{16}}}; \phi = \phi_{36}^{\mathrm{unk}} - \phi_{34}^{\mathrm{ref}} - \phi_{45}^{\mathrm{ref}} - \phi_{56}^{\mathrm{ref}} \quad (3.8)$$

The refractive index, n of the probe laser is related with the density matrix element, ρ_{12} as $n = 1 + 3\lambda_p^2 N/(2\pi)(\Gamma_2/\Omega_{12})\rho_{12}$, where λ_p(=780 nm) is the wavelength of the probe laser and N is atomic number density [98, 99]. The imaginary part of n is related with the absorption and real part with dispersion. We define the normalized absorption $[(\Gamma_2/\Omega_{12})\mathrm{Im}(\rho_{12})]$ i.e. for the stationary atoms, the absorption of the probe laser at resonance in the absence of all the control lasers is 1.

In order to verify the approximation made above, we have checked the analytical solution of ρ_{12} given by the Eq. 3.8 and the complete numerical solution in the steady state for various values of control fields and detunings. It has excellent agreement between complete numerical and approximated analytical solution as shown in Fig. 3.3. The solution for ρ_{12} in Eq. 3.8 has the following interpretation.

3.2.3 Interpretation

Interference between two sub-system

Eq. 3.8 looks very complicated but it can be interpreted in the following simple way. The closed loop system can be realized by two open loop sub-systems $|3\rangle\rightarrow|4\rangle\rightarrow|5\rangle\rightarrow|6\rangle$ and $|3\rangle\rightarrow|6\rangle\rightarrow|5\rangle\rightarrow|4\rangle$ shown with red and green arrows respectively as shown in Fig. 3.1b. These two sub-system shares a common $|1\rangle\rightarrow|2\rangle\rightarrow|3\rangle$ ladder system. In order to understand the absorption property of the probe laser Ω_{12}, we switch on the control fields one by one and in the sequence for the two sub-systems. Firstly, the control laser Ω_{23} causes transparency for the probe laser Ω_{12} and known as EIT. For path shown with the red color, the control field Ω_{34}^{ref} recovers the absorption against the EIT created by Ω_{23} and known as EITA. Again the control fields Ω_{45}^{ref} causes transparency against the EITA created by the Ω_{23} and Ω_{34}^{ref}, and known as EITAT. Finally the Ω_{56}^{ref} causes absorption against the EITAT created by the Ω_{23}, Ω_{34}^{ref} and Ω_{45}^{ref}, and known as EITATA [97] and expressed by EITATA1 in Eq. 3.8. (In order to understand the transparency and absorption in the sequence, we strongly advice the readers to see the paper [97].) The other path shown with green color will also cause EITATA by sequence of the control fields Ω_{36}^{unk}, Ω_{56}^{ref} and Ω_{45}^{ref} which is expressed by EITATA2. Further, these two sub-system causing EITATA1 and EITATA2, interferes with each other and expressed by the Int term in the Eq. 3.8, which is phase(ϕ) dependent.

In the other words, the closed loop $|3\rangle \rightarrow |4\rangle \rightarrow |5\rangle \rightarrow |6\rangle \rightarrow |3\rangle$ causes absorption against EIT created by the control laser Ω_{23}. The closed loop has two-open loop sub-systems which interfere destructively (for $\phi = 0$) and constructively (for $\phi = \pi$) with each other. As shown in Fig. 3.4 a, for $|\Omega_{34}^{\text{ref}}|=|\Omega_{45}^{\text{ref}}|=|\Omega_{56}^{\text{ref}}|=|\Omega_{36}^{\text{unk}}| =\Gamma_2$ ($>> \gamma^{dec}$), there is a complete transparency at the line center for $\phi = 0$. This is due to perfect destructive interference between the two-subsystems as the strength is same for both, i.e. EITATA1 = EITATA2. There is maximum absorption at the line center for $\phi = \pi$ as the two sub-systems are interfering constructively. For $|\Omega_{34}^{\text{ref}}|=|\Omega_{45}^{\text{ref}}|=|\Omega_{56}^{\text{ref}}| \neq |\Omega_{36}^{\text{unk}}| >>\gamma^{dec}$, there is a absorption peak at the line center for $\phi = 0$, as shown in Fig. 3.4 b. This is due to unequal strength of the individual system (EITATA1>EITATA2), hence the destructive interference between them is not perfect.

Dressed state approach

At high Rabi frequencies (much greater than the absorption peaks linewidths) of the control lasers and MW fields, the linewidth of the absorption peak can be explained using dressed state picture. In this condition there is no interference between the absorption peaks as they are well separated from each other. The position of the absorption peak is determined by the eigenvalues of the Hamiltonian associated to the control fields as given below

$$H_c = \begin{bmatrix} 0 & \frac{\Omega_{23}}{2} & 0 & 0 & 0 \\ \frac{\Omega_{23}^*}{2} & \delta_{23} & \frac{|\Omega_{34}^{\text{ref}}|}{2}e^{i\phi_{34}} & 0 & \frac{|\Omega_{36}^{\text{unk}}|}{2}e^{i\phi_{36}} \\ 0 & \frac{|\Omega_{34}^{\text{ref}}|}{2}e^{-i\phi_{34}} & \delta_{23}-\delta_{34} & \frac{|\Omega_{45}^{\text{ref}}|}{2}e^{i\phi_{45}} & 0 \\ 0 & 0 & \frac{|\Omega_{45}^{\text{ref}}|}{2}e^{-i\phi_{45}} & \delta_{23}-\delta_{34}+\delta_{45} & \frac{|\Omega_{56}^{\text{ref}}|}{2}e^{i\phi_{56}} \\ 0 & \frac{|\Omega_{36}^{\text{unk}}|}{2}e^{-i\phi_{36}} & 0 & \frac{|\Omega_{56}^{\text{ref}}|}{2}e^{-i\phi_{56}} & \delta_{23}-\delta_{34}+\delta_{45}+\delta_{56} \end{bmatrix} \quad (3.9)$$

For general control fields detunings and Rabi frequencies, the position of the absorption peaks will be complicated. However, the expression becomes simpler for zero detuning of control fields and with $|\Omega_{23}| = |\Omega_{34}^{\text{ref}}| = |\Omega_{45}^{\text{ref}}| = |\Omega_{56}^{\text{ref}}| = \Omega$, but with arbitrary values of $|\Omega_{36}^{\text{unk}}|$. In this condition the positions of the absorption peaks (i.e. eigenvalues of the H_c) are

$$-\frac{1}{\sqrt{8}}\sqrt{4\Omega^2+|\Omega_{36}^{\text{unk}}|^2+\sqrt{(2\Omega^2+|\Omega_{36}^{\text{unk}}|^2)^2+8\Omega^3|\Omega_{36}^{\text{unk}}|cos\phi}},$$

$$-\frac{1}{\sqrt{8}}\sqrt{4\Omega^2+|\Omega_{36}^{\text{unk}}|^2-\sqrt{(2\Omega^2+|\Omega_{36}^{\text{unk}}|^2)^2+8\Omega^3|\Omega_{36}^{\text{unk}}|cos\phi}}, 0,$$

$$\frac{1}{\sqrt{8}}\sqrt{4\Omega^2+|\Omega_{36}^{\text{unk}}|^2-\sqrt{(2\Omega^2+|\Omega_{36}^{\text{unk}}|^2)^2+8\Omega^3|\Omega_{36}^{\text{unk}}|cos\phi}}, \text{ and}$$

$$\frac{1}{\sqrt{8}}\sqrt{4\Omega^2+|\Omega_{36}^{\text{unk}}|^2+\sqrt{(2\Omega^2+|\Omega_{36}^{\text{unk}}|^2)^2+8\Omega^3|\Omega_{36}^{\text{unk}}|cos\phi}}.$$

The eigenvectors determines the dressed state in terms of the bare atomic states. For example the normalized eigenvector corresponding to eigenvalue 0 is

$$\frac{1}{[(1+\frac{|\Omega_{36}^{\rm unk}|^2}{\Omega^2}-2\frac{|\Omega_{36}^{\rm unk}|}{\Omega}cos\phi)+2]^{1/2}}\begin{bmatrix}1-\frac{|\Omega_{36}^{\rm unk}|}{\Omega}e^{i\phi}\\0\\-1\\0\\1\end{bmatrix} \tag{3.10}$$

This is the central dressed state (or the central absorption peak) and is expressed as $[(1-\frac{|\Omega_{36}^{\rm unk}|e^{i\phi}}{\Omega})\,|2\rangle-|4\rangle+|6\rangle]/[(1+\frac{|\Omega_{36}^{\rm unk}|^2}{\Omega^2}-2\frac{|\Omega_{36}^{\rm unk}|}{\Omega}cos\phi)+2]^{1/2}$. The linewidth of the dressed state or the absorption peak is given in terms of the bare atomic states decay rate. For example, if dressed state is written as $C_2\,|2\rangle+C_3\,|3\rangle+C_4\,|4\rangle+C_5\,|5\rangle$ then the linewidth of it will be $|C_2|^2\Gamma_2+|C_3|^2\Gamma_3+|C_4|^2\Gamma_4+|C_5|^2\Gamma_5$ Hence the linewidth of the cenetral absorption peak is given by $[(1+\frac{|\Omega_{36}^{\rm unk}|^2}{\Omega^2}-2\frac{\Omega_{36}^{\rm unk}}{\Omega}cos\phi)\Gamma_2+\Gamma_4+\Gamma_6]/[(1+\frac{|\Omega_{36}^{\rm unk}|}{\Omega^2}-2\frac{\Omega_{36}^{\rm unk}}{\Omega}cos\phi)+2]$ which is phase dependent. In order to crosscheck the expression for the linewidth, we fit (shown with black solid line) the central peak of the normalized absorption obtained by Eq. 3.8 with Lorentzian profile to find the linewidth for three different phases as shown in Fig. 3.4. The fitted linewidths for $\phi=0$, $\phi=\pi/2$ and $\phi=\pi$ are $0.13\Gamma_2$, $0.47\Gamma_2$ and $0.64\Gamma_2$ respectively, while the calculated linewidths are $0.13\Gamma_2$, $0.39\Gamma_2$ and $0.54\Gamma_2$ respectively. There is a small mismatch between the fitted and the calculated linewidths by the dressed state approach for $\phi=\pi/2$ and $\phi=\pi$. This is because, as we see in Fig. 3.4, the central absorption peak is broadened for $\phi=\pi/2$ and $\phi=\pi$ and the interference between peaks starts playing a role in the modification of the linewidth similar to three level system [100].

3.3 Results

3.3.1 Probe laser absorption

The normalized absorption ($\mathrm{Im}(\rho_{12})\Gamma_2/\Omega_{12}$) vs probe detuning ($\delta_{12}$) for three different phases, $\phi=0,\pi/2$ and π is shown in Fig. 3.4. For the central absorption peak i.e. at

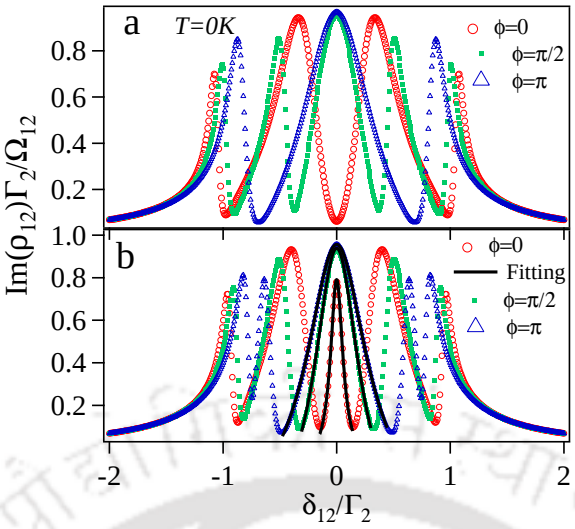

FIGURE 3.4: Normalized absorption ($\mathrm{Im}(\rho_{12})\Gamma_2/\Omega_{12}$) vs δ_{12}/Γ_2 of the probe laser with $|\Omega_{23}| = |\Omega_{34}^{\mathrm{ref}}| = |\Omega_{45}^{\mathrm{ref}}| = |\Omega_{56}^{\mathrm{ref}}| = \Gamma_2$, $\delta_{23} = \delta_{34} = \delta_{45} = \delta_{56} = \delta_{36} = 0$ and (a) $|\Omega_{36}^{\mathrm{unk}}| = \Gamma_2$ (b) $|\Omega_{36}^{\mathrm{unk}}| = 0.5\Gamma_2$.

$\delta_{12} = 0$, only the linewidth depends upon the phase but not the position, while both the position and the linewidth depends upon the phase(ϕ) for the other four absorption peaks. This has been explained in the previous section.

Now, we consider the effect of the temperature as lineshape of EIT is significantly changed by the thermal averaging [21, 23, 101–104]. The thermal averaging of ρ_{12} is done numerically for the room temperature (T =300 K) for the counter-propagating configuration of the probe (Ω_{12}) and the control laser (Ω_{23}) with wave-vectors k_{780} and k_{480} respectively by replacing δ_{12} with $\delta_{12} + k_{780}v$ and δ_{23} with $\delta_{23} - k_{480}v$ for moving atoms with velocity v, while the Doppler shift for the MW fields are ignored. Further the ρ_{12} is weighted by the Maxwell Boltzmann velocity distribution function and integrated over the velocity as $\rho_{12}^{\mathrm{Thermal}} = \sqrt{\frac{m}{2\pi k_B T}} \int \rho_{12}(v) e^{-\frac{mv^2}{2k_B T}} dv$, where k_B is Boltzmann constant and m is atomic mass of Rb. The integration is done over velocity range which is three times of $\sqrt{\frac{k_B T}{m}}$. The Doppler averaging changes the absorption profile significantly as shown in Fig. 3.5. One of the interesting modifications is the phase dependency of the probe laser absorption at the zero detunings of the probe. The probe laser absorption is minimum for $\phi = 0$ and maximum for $\phi = \pi$ as shown with red and blue curve respectively in Fig. 3.5. This modification is due to mismatch of Doppler shift for probe at 780 nm and the control at 480 nm for moving atom. Please note that without thermal averaging at

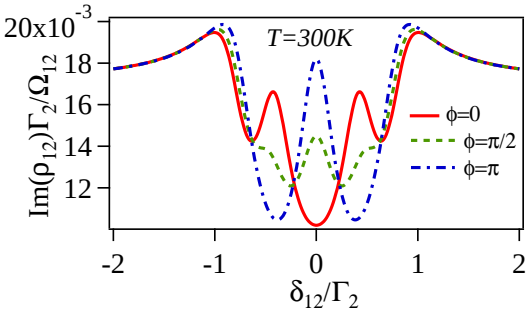

FIGURE 3.5: Normalized absorption of the probe laser with thermal averaging (Im $(\rho_{12}^{\text{Thermal}})\Gamma_2/\Omega_{12}$) vs δ_{12}/Γ_2 with $|\Omega_{23}| = |\Omega_{34}^{\text{ref}}| = |\Omega_{45}^{\text{ref}}| = |\Omega_{56}^{\text{ref}}| = \Gamma_2$, $|\Omega_{36}^{\text{unk}}| = 0.5\Gamma_2$ and $\delta_{23} = \delta_{34} = \delta_{45} = \delta_{56} = \delta_{36} = 0$.

zero detunings of the probe, control laser and MW fields, probe laser absorption has no significant difference between $\phi = \pi/2$ and π.

3.3.2 Phase sensitivity

Sinusoidal behaviour

As seen in the previous section that the absorption profile of the probe laser depends upon the phase, ϕ. Please note that the previously studied (i.e. four-level) system [48–53] were insensitive to the phase of the MW field. This is also clear from Eq. 3.8 in the special case with $|\Omega_{34}^{\text{ref}}|=|\Omega_{45}^{\text{ref}}|=|\Omega_{56}^{\text{ref}}| = 0$, which reduces the six-level loopy ladder system to four-level system and will have no phase dependency.

The probe absorption at room temperature vs the phase ϕ with all the detunings to be zero is shown in Fig. 3.6. From the plot shown with red open circle in Fig. 3.6a we observe more than 15% change in the probe absorption for the change of the phase from 0 to π for the chosen combinations of the control Rabi frequencies. In particular, we have chosen low value of $|\Omega_{36}^{\text{unk}}| = 0.1\Gamma_2$ and the optimized control fields Rabi frequencies i.e. $|\Omega_{23}| = 2\Gamma_2$, $|\Omega_{34}^{\text{ref}}| = 1.5\Gamma_2$, and $|\Omega_{45}^{\text{ref}}| = |\Omega_{56}^{\text{ref}}| = 4\Gamma_2$. The numerical data points (red open circle) are fitted by a function A+Bsin(fϕ+θ), where A, B, f and θ are kept as free parameters that yields f=1 and the fitting is shown with black curve in Fig. 3.6a. Now, choosing a high value of $|\Omega_{36}^{\text{unk}}| = 2.5\Gamma_2$ and keeping the other parameters unchanged, we observe more than 80% change in the probe absorption for the change of the phase from 0

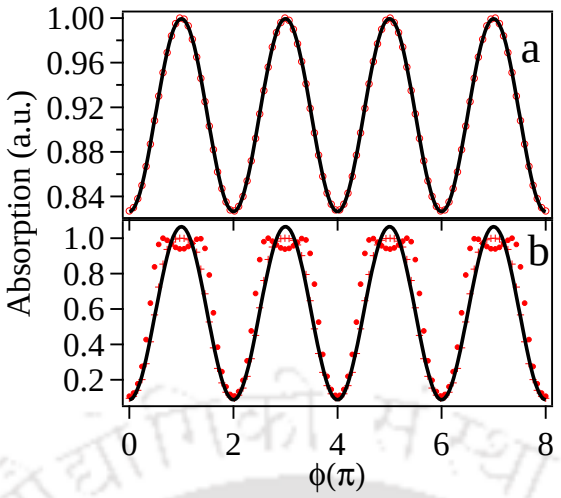

FIGURE 3.6: Absorption of the probe laser after thermal averaging in arbitrary scale obtained as $(\mathrm{Im}(\rho_{12}^{\mathrm{Thermal}}))/\max(\mathrm{Im}(\rho_{12}^{\mathrm{Thermal}}))$ vs phase ϕ with $\delta_{12} = \delta_{23} = \delta_{34} = \delta_{45} = \delta_{56} = \delta_{36} = 0$ and (a) $|\Omega_{36}^{\mathrm{unk}}| = 0.1\Gamma_2$, $|\Omega_{23}| = 2\Gamma_2$, $|\Omega_{34}^{\mathrm{ref}}| = 1.5\Gamma_2$, and $|\Omega_{45}^{\mathrm{ref}}| = |\Omega_{56}^{\mathrm{ref}}| = 4\Gamma_2$. (b) crossed points $|\Omega_{36}^{\mathrm{unk}}| = 2.5\Gamma_2$, $|\Omega_{23}| = 3\Gamma_2$, $|\Omega_{34}^{\mathrm{ref}}| = 2\Gamma_2$, and $|\Omega_{45}^{\mathrm{ref}}| = |\Omega_{56}^{\mathrm{ref}}| = 4\Gamma_2$, solid circled points $|\Omega_{36}^{\mathrm{unk}}| = 2.5\Gamma_2$, $|\Omega_{23}| = 3\Gamma_2$, $|\Omega_{34}^{\mathrm{ref}}| = 3\Gamma_2$, and $|\Omega_{45}^{\mathrm{ref}}| = |\Omega_{56}^{\mathrm{ref}}| = 4\Gamma_2$.

to π as shown crossed red points, but there is a deviation from sinusoidal behavior. This deviation is compared with the fitted black curve as shown in Fig. 3.6b. On increasing the value of $|\Omega_{34}^{\mathrm{ref}}|$ to $3\Gamma_2$ and keeping the other parameters unchanged, there is a splitting of the absorption at $\phi = \pi$ as shown by the solid circled points in this figure.

Optimization of sensitivity

Now, we maximize the phase sensitivity for this system for given value of $|\Omega_{36}^{\mathrm{unk}}|$ by using the parameters, Ω_{23}, $|\Omega_{34}^{\mathrm{ref}}|$, $|\Omega_{45}^{\mathrm{ref}}|$, and $|\Omega_{56}^{\mathrm{ref}}|$. In order to do this we define a quantity called sensitivity as $S = \mathrm{Im}[\rho_{12}^{\mathrm{Thermal}}(\phi = 0) - \rho_{12}^{\mathrm{Thermal}}(\phi = \pi)]/\mathrm{Im}[\rho_{12}^{\mathrm{Thermal}}(\phi = 0) + \rho_{12}^{\mathrm{Thermal}}(\phi = \pi)]$, which is a measure of the phase/strength sensitivity of the system and is to be maximized. For given value of $|\Omega_{36}^{\mathrm{unk}}|$, we maximize the S by minimizing $1/S$ or -S using matlab inbuilt function "fmincon" treating Ω_{23}, $|\Omega_{34}^{\mathrm{ref}}|$, $|\Omega_{45}^{\mathrm{ref}}|$, and $|\Omega_{56}^{\mathrm{ref}}|$ as free parameters but bounded in the region from 0 to $5\Gamma_2$. Please note that the values $5\Gamma_2$ for Ω_{23} $|\Omega_{34}^{\mathrm{ref}}|$, $|\Omega_{45}^{\mathrm{ref}}|$, and $|\Omega_{56}^{\mathrm{ref}}|$ is well in the experimental reach.

We first consider the case without thermal averaging i.e. $T = 0$. The maximized sensitivity, S_{max} vs $|\Omega_{36}^{\mathrm{unk}}|$ is plotted in Fig. 3.7(a). The S_{max} increases with $\Omega_{36}^{\mathrm{unk}}$ and

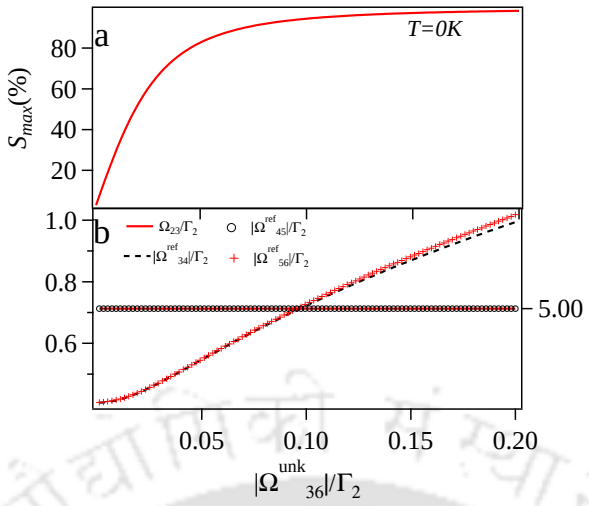

FIGURE 3.7: (a) The maximum sensitivity S_{max} (%) vs $|\Omega^{\text{unk}}_{36}|/\Gamma_2$ (b) The optimum value of $|\Omega^{\text{ref}}_{34}|/\Gamma_2$ and $|\Omega^{\text{ref}}_{56}|/\Gamma_2$ for S_{max} (shown by left scale), Ω_{23}/Γ_2 and $|\Omega^{\text{ref}}_{45}|/\Gamma_2$ (shown by right scale) vs $|\Omega^{\text{unk}}_{36}|$ for $\delta_{12} = \delta_{23} = \delta_{34} = \delta_{45} = \delta_{56} = \delta_{36} = 0$ and $T = 0$.

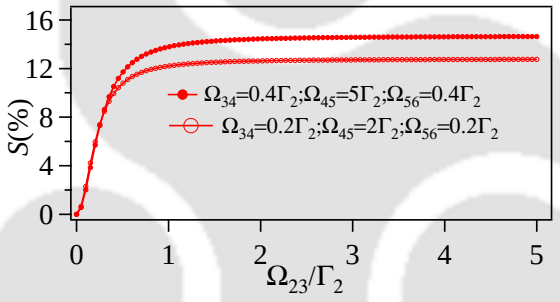

FIGURE 3.8: S_{max} (%) = $\text{Im}[\rho_{12}(\phi = 0) - \rho_{12}(\phi = \pi)]/\text{Im}[\rho_{12}(\phi = 0) + \rho_{12}(\phi = \pi)] \times 100$ vs Ω_{23}/Γ_2 for $\delta_{12} = \delta_{23} = \delta_{34} = \delta_{45} = \delta_{56} = \delta_{36} = 0$, $|\Omega^{\text{unk}}_{36}| = 0.005\Gamma_2$ and $T = 0$.

starts saturating around $0.05\Gamma_2$. The corresponding maximizing values of Ω_{23}, $|\Omega^{\text{ref}}_{34}|$, $|\Omega^{\text{ref}}_{45}|$, and $|\Omega^{\text{ref}}_{56}|$ are also plotted in Fig. 3.7(b). The optimum value of the Ω_{23} is as high as possible which is $5\Gamma_2$ in this case as it is bounded by this limit. This is more clear from the Fig. 3.8, where S_{max} increases with Ω_{23} and then saturates around Γ_2 for any given values of $|\Omega^{\text{ref}}_{34}|$, $|\Omega^{\text{ref}}_{45}|$, $|\Omega^{\text{ref}}_{56}|$, and $|\Omega^{\text{unk}}_{36}|$.

Next, we consider the room temperature case ($T = 300\ K$), which makes the problem a bit more complicated, as the lineshape of the absorption gets modified significantly as described previously. The maximum sensitivity (S_{max}) vs $|\Omega^{\text{unk}}_{36}|$ is plotted in the Fig. 3.9(a). The S_{max} at $T = 300K$ is much lower than the case at $T = 0$ as the saturation point is around $|\Omega^{\text{unk}}_{36}| = 1.5\ \Gamma_2$ as compared to $0.05\Gamma_2$ and hence at $T = 0$ the system

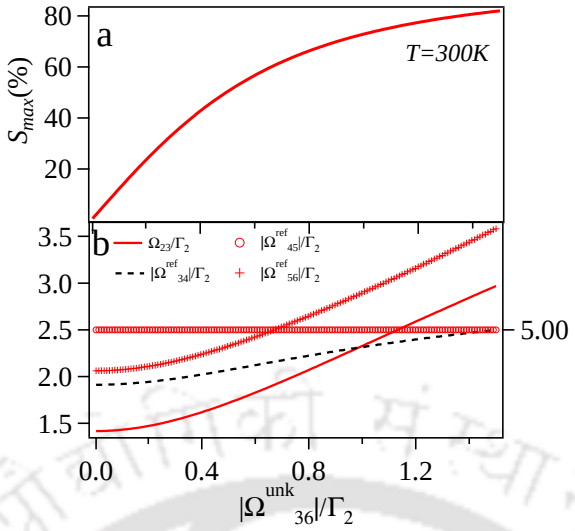

FIGURE 3.9: (a) S_{max} (%) vs $|\Omega^{\text{unk}}_{36}|/\Gamma_2$ (b) The optimum value of Ω_{23}/Γ_2, $|\Omega^{\text{ref}}_{34}|/\Gamma_2$, and $|\Omega^{\text{ref}}_{56}|/\Gamma_2$ shown by left scale and $|\Omega^{\text{ref}}_{45}|/\Gamma_2$ shown by right scale vs $|\Omega^{\text{unk}}_{36}|/\Gamma_2$ for $\delta_{12} = \delta_{23} = \delta_{34} = \delta_{45} = \delta_{56} = \delta_{36} = 0$ and $T = 300K$.

can detect the phase of lower values of $|\Omega^{\text{unk}}_{36}|$. Unlike the case of $T = 0$, in this case for S_{max} the value of $\Omega_{23} \neq 5\Gamma_2$ but has optimum values as shown in Fig. 3.9(b).

3.3.3 Strength sensitivity

The quantity, S defined above can also be used as a measure of the strength/amplitude sensitivity for $|\Omega^{\text{unk}}_{36}|$ for the six-level loopy ladder system. The strength sensitivity parameter is useful as it provides a measure of the change in absorption of a system due to a change in the strength or amplitude of the unknown field. Now we compare the strength sensitivity of the six-level loopy ladder system with the previously studied four-level system [48–53]. The solution of ρ_{12} for the four-level system can be obtained from the six-level loopy ladder system by setting $|\Omega^{\text{ref}}_{34}|=|\Omega^{\text{ref}}_{45}|=|\Omega^{\text{ref}}_{56}|=0$ in Eq. 3.8 and is given by Eq. 3.11.

$$\rho_{12(4l)} = \frac{\frac{i}{2}\frac{\Omega_{12}}{\gamma_{12}}}{1 + \frac{\frac{1}{4}\frac{|\Omega_{23}|^2}{\gamma_{12}\gamma_{13}}}{1+\frac{1}{4}\frac{|\Omega^{\text{unk}}_{36}|^2}{\gamma_{13}\gamma_{16}}}} \tag{3.11}$$

The subscript $(4l)$ indicates for four-level system. Further the thermal averaging can be done in a similar fashion as in the case of the six-level system i.e. $\rho_{12(4l)}^{\text{Thermal}} = \sqrt{\frac{m}{2\pi k_B T}} \int \rho_{12(4l)}(v) e^{-\frac{mv^2}{2k_B T}} dv$. We define the strength sensitivity for the four-level system for unknown $|\Omega_{36}^{\text{unk}}|$ as change in the absorption in the presence and the absence of the $|\Omega_{36}^{\text{unk}}|$ normalized by the sum of the two conditions which is mathematically expressed as $S = \left[\rho_{12(4l)}^{\text{Thermal}}(|\Omega_{36}^{\text{unk}}| \neq 0) - \rho_{12(4l)}^{\text{Thermal}}(|\Omega_{36}^{\text{unk}}| = 0)\right] / \left[\rho_{12(4l)}^{\text{Thermal}}(|\Omega_{36}^{\text{unk}}| \neq 0) + \rho_{12(4l)}^{\text{Thermal}}(|\Omega_{36}^{\text{unk}}| = 0)\right]$. We maximize the sensitivity of the four-level system adapting similar method as for the six-level system but with only one optimizing parameter i.e. Ω_{23}.

First, we consider $T = 0$ case. The maximized strength sensitivity for the six-level loopy ladder system and the four-level system is compared in Fig. 3.10. From this figure it is clear that the six-level system has more sensitivity as compared to the four-level system as shown in Fig. 3.10 (a). In order to quantify this comparison, we plot the ratio of the sensitivities of the six-level to four-level system in Fig.3.10 (b). The ratio is more for the low values of the $|\Omega_{36}^{\text{unk}}|$. The increased sensitivity for the six-level loopy system is due to the interferometric nature of the system where the effect of small $|\Omega_{36}^{\text{unk}}|$ is enhanced by the large values of the $|\Omega_{34}^{\text{ref}}|$, $|\Omega_{45}^{\text{ref}}|$ and $|\Omega_{56}^{\text{ref}}|$ as the **int** term in Eq. 3.8 involves multiplication of these quantities. The strength sensitivity of both the systems decreases with increased γ_{dec} (from $2\pi \times 100$kHz to $2\pi \times 500$kHz) but the effect is more for the four-level system in comparison to the six-level system as shown Fig. 3.10b.

Now, we consider the case at the room temperature. The strength sensitivity for the six-level and previously studied four-level is plotted in Fig. 3.11(a). Form this plot it is clear that the six-level system has much superior strength sensitivity as compared to the four-level system. Further we quantify the comparison by plotting the ratio (R) of the sensitivities of the six-level to the four-level for different values of $|\Omega_{36}^{\text{unk}}|$ in Fig.3.11(b). In order to check the stringency of γ_{dec} on the sensitivity, we also plot S_{max} for these two systems taking $\gamma_{dec} = 2\pi \times 500$kHz.

We also plot the R vs maximum sensitivity (S_{max}) of the six-level system which gives the information about the possibility of the detection of $|\Omega_{36}^{\text{unk}}|$. This is an important plot because there is a possibility that the R might be huge but cannot be detected by the six-level system as well. The detection of S_{max} up to 1% is very much feasible using

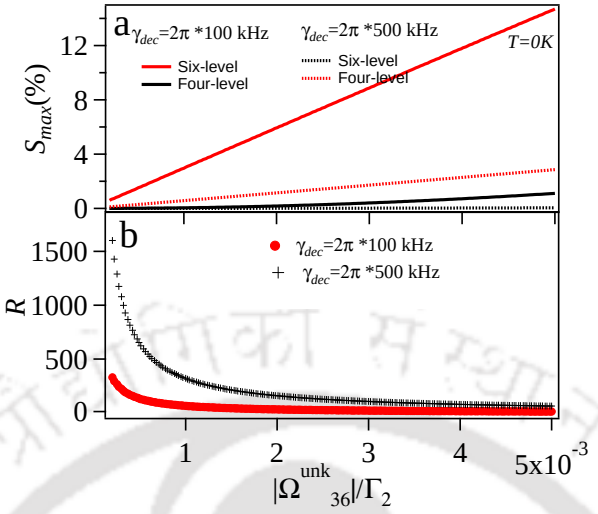

FIGURE 3.10: (a) $S_{max}(\%)$ vs $|\Omega^{\text{unk}}_{36}|/\Gamma_2$ for six-level loopy and four-level ladder system (b) ratio (R) of the sensitivity between six-level and four-level system vs $|\Omega^{\text{unk}}_{36}|/\Gamma_2$ at $T = 0$ with all the detunings to be zero and for $\gamma_{dec} = 2\pi \times 100$kHz and $\gamma_{dec} = 2\pi \times 500$kHz.

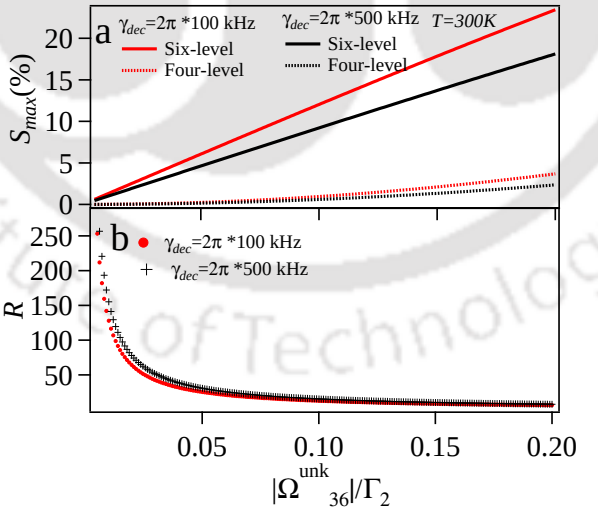

FIGURE 3.11: (Color online). (a) $S_{max}(\%)$ vs $|\Omega^{\text{unk}}_{36}|/\Gamma_2$ for six-level loopy and four-level ladder system (b) ratio (R) of the sensitivity between six-level and four-level system vs $|\Omega^{\text{unk}}_{36}|/\Gamma_2$ at $T = 300K$ with all the detunings to be zero and for $\gamma_{dec} = 2\pi \times 100$kHz and $\gamma_{dec} = 2\pi \times 500$kHz.

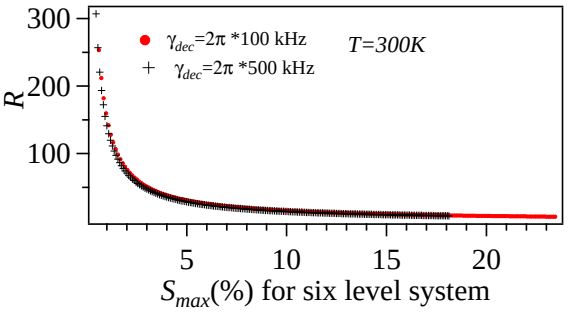

FIGURE 3.12: Ratio (R) of the sensitivity between six-level and four-level system vs S_{max} (%) of the six-level system at $T = 300K$. The variation of S_{max} (%) corresponds to range of $|\Omega_{36}^{\text{unk}}|$ from $0.005\Gamma_2$ to $0.02\Gamma_2$.

locking detection. At this value of sensitivity for the six-level system, the sensitivity of the four-level system will be around $\frac{1}{150}\%$ as shown in Fig. 3.12.

Finally one more important point is that, for the six-level loopy ladder system the MW field Ω_{36}^{unk} can be detected by just varying the phase of the reference MW fields, while in the case of the four-level system we need to insert and remove MW mechanical shield.

3.3.4 Frequency range

The frequency range of the atomic based MW interferometry can be anywhere from the range of the few tens of MHz, GHz and THz. The Rydberg states can be chosen depending upon the interest of the frequency region of MW field. For example, for frequency in the range of few tens of GHz n_{ryd}'s should around 54 [50] while for tens of MHz it should be higher number and it is around 57 in case of Cs [51]. For THz regime this should be around 20 [105].

3.4 Discussion

In conclusion we theoretically study a six-level loopy ladder system using Rydberg states for the phase sensitive MW or RF electrometry. This is based upon the interference between the two sub-systems of EITATA. In counter-propagating configuration of the probe and control laser there is a change of the lineshape of the probe absorption due

to Doppler averaging. The limitation of the proposed system is the decoherence rate between the ground state and the Rydberg states. The previously explored four- level atomic system has the same limitation and is already much superior than the electrical circuit for the strength sensitivity, frequency range and spatial resolution. This proposed system further improves the sensitivity by two orders of magnitude, removes the drawback of the phase insensitivity of the previous atomic four level-system and retains the advantages of the large frequency range of operation and spatial resolution. This system provides a great possibility to characterize the MW or RF electric fields completely including the propagation direction and the wavefront. This work will be quite useful for MW and RF engineering hence in the communications specially in active radar technologies and synthetic aperture radar interferometry.

This chapter has been published as:
Highly sensitive atomic based MW interferometry
Dangka Shylla, Elijah Nyakang'o Ogaro and Kanhaiya Pandey
Sci Rep 8, 8692 (2018). https://doi.org/10.1038/s41598-018-27011-1

Chapter 4

Atomic coherence based multi lasers interferometry

THIS chapter outlines the experimental study of an atomic coherence based multi laser interferometry in a closed loop double Λ-type system using a Rb vapour cell at room temperature. This scheme is based upon the principle of phase-dependent electromagnetically induced transparency (EIT). EIT in closed loop systems is dependent on the phase difference between the electromagnetic fields forming the loop. In order to experimentally realise the principle of phase-dependent EIT (i.e., atomic coherence based interferometry) in closed loop systems, we explore this effect in two different configuration of a closed loop double Λ-type system. The first configuration involves the excited states with same decay rates at the 780 nm transition and the second configuration involves the excited states with different decay rates at the 780 nm and 420 nm transitions.

4.1 Introduction

Atomic coherence is the reason for the modification of the absorption of the probe laser in the presence of a control laser, also known as electromagnetically induced transparency (EIT) [4, 5]. The atomic coherence is caused by the simultaneous driving of the levels by probe and control laser sharing the common levels. The phenomenon of EIT has a wide applications in the field of atomic and optical physics such as slowing of light [34–36], precision spectroscopy [66], precise atomic clocks [70], magnetometry [25–31], radiofrequency (RF) [45–47] and microwave (MW) [43, 44] electrometry, etc. In the steady state, EIT is insensitive to the phase of the electromagnetic fields for the open loop multi-level systems which limits the phase determination of electromagnetic field [49, 97]. However, in the closed loop multi-level systems, EIT is dependent on the phase difference between the electromagnetic fields forming the loop [59–62, 64, 106]. The phase dependence arises from the fact that there are two path of excitation which can interfere constructively or destructively depending on the phase difference between them. These two paths can be due to two oppositely polarized electromagnetic fields and hence the interference is observed between them which is in contrast to the interference in space.

The atomic coherence based multi laser interferometry is based upon the principle of phase-dependent electromagnetically induced transparency (EIT). In this work, we demonstrate the atomic coherence based multi laser interferometry in two different configuration of a closed loop double Λ-type system. The first configuration involves the excited states ($5P_{3/2}(F = 0, 1)$) with same decay rates ($2\pi \times 6$ MHz) at the 780 nm transition and the second configuration involves the excited states ($5P_{3/2}(F = 0, 1)$ and $6P_{3/2}(F = 0)$) with different decay rates ($2\pi \times 6$ MHz and $2\pi \times 1.4$ MHz) at the 780 nm and 420 nm transitions. Here, we study the phase sensitivity and the frequency response of the two different systems in order to compare them.

This chapter is organized as follows. In section 4.2, we describe the relevant energy levels for the different experimental configurations and the experimental set-up. In section 4.3, we describe the density matrix formalism for the double Λ-type and the numerically simulated absorption profile of the probe. In section 4.4, we present the experimental

results of the phase sensitivity and the frequency response of the two different systems. Finally in section 4.5, we give the conclusion on this work.

4.2 The energy level schemes and set-up

4.2.1 Michelson interferometer

The Michelson interferometer is a well-known and widely used type of interferometer in the field of optics and is shown in Fig. 4.1a. A laser beam from the 780 nm source is split into two parts by the beamsplitter. The two laser beams are then retro-reflected back to the same beamsplitter where they are combined and then directed to a photodetector. The two laser beams will interfere constructively or destructively depending upon the phase difference between the two arms of the interferometer. This change in phase is achieved by employing a mirror actuated by a piezoelectric transducer (PZT) in one of the arms of the interferometer.

4.2.2 Double Λ-type system at 780 nm transition

The energy level diagram of the double Λ-type system in ^{87}Rb which involves the excited states with same decay rates at 780 nm transitions that contains the hyperfine magnetic sublevels is given in Fig. 4.1b. The decay rates of the two excited states, $5P_{3/2}(F = 0)$ and $5P_{3/2}(F = 1)$ are given by Γ_4 and Γ_2 respectively, where $\Gamma_4 = \Gamma_2 = 2\pi\times6$ MHz. The 780 nm probe laser is locked to resonance on the $5S_{1/2}(F = 1) \rightarrow 5P_{3/2}(F = 1)$ transition and the control laser is locked to the $5S_{1/2}(F = 1) \rightarrow 5P_{3/2}(F = 0)$ transition. These two lasers differ in frequency by the hyperfine separation of 72 MHz between the $(F = 0)$ and $(F = 1)$ of the $5P_{3/2}$ state.

4.2.3 Double Λ-type system at 780 nm transition and 420 nm transition

The energy level diagram of the double Λ-type systems in ^{87}Rb which involves the excited states with different decay rates at 780 nm and 420 nm transition that also contains the

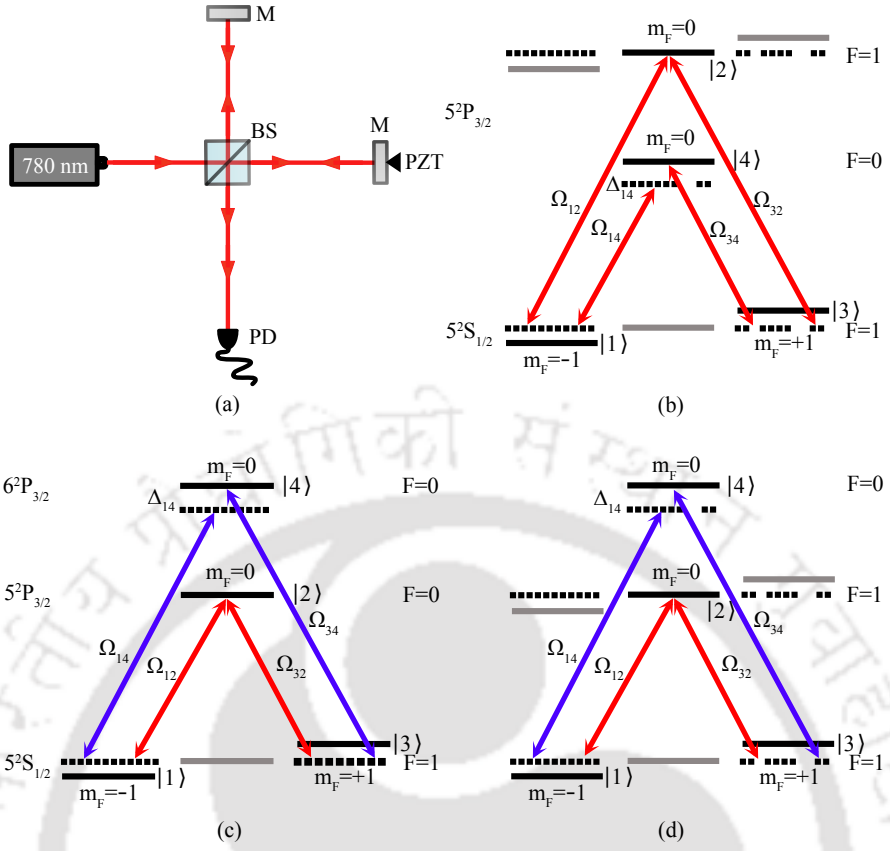

FIGURE 4.1: (a) The Michelson interferometer. (b) Energy level diagram of the double Λ-type system in ^{87}Rb which involves the excited states with same decay rates using transitions at 780 nm that contains the hyperfine magnetic sublevels. Energy level diagram of the double Λ-type systems in ^{87}Rb which involves the excited states with different decay rates at 780 nm and 420 nm transitions that also contains the hyperfine magnetic sublevels when probe is locked to (c) $5S_{1/2}(F = 1) \rightarrow 5P_{3/2}(F = 0)$ and (d) $5S_{1/2}(F = 1) \rightarrow 5P_{3/2}(F = 1)$ transition. The control laser is locked to the $5S_{1/2}(F = 1) \rightarrow 6P_{3/2}(F = 0)$ for both (c) and (d). M: mirror; PZT: piezoelectric transducer; BS: beamsplitter; PD: photodetector.

hyperfine magnetic sublevels is given in Fig. 4.1c and Fig. 4.1d. The decay rates of the two excited states, $5P_{3/2}(F = 0)(5P_{3/2}(F = 1))$ and $6P_{3/2}(F = 0)$ are given by Γ_4 and Γ_2 respectively, where $\Gamma_4 = 2\pi\times6$ MHz and $\Gamma_2 = 2\pi\times1.4$ MHz. The 780 nm probe laser is locked to resonance on $5S_{1/2}(F = 1) \rightarrow 5P_{3/2}(F = 0)$ transition for the double Λ-type system in Fig. 4.1c. While the 780 nm probe laser is locked to resonance on $5S_{1/2}(F = 1) \rightarrow 5P_{3/2}(F = 1)$ transition for the double Λ-type system in Fig. 4.1d. The 420 nm control laser beam is locked to the transition $5S_{3/2}(F = 1) \rightarrow 6P_{3/2}(F = 0)$ for both the cases.

4.2.4 Set-up I: Double Λ-type system at 780 nm transition

The experimental set-up of the double Λ-type system in ^{87}Rb at 780 nm transitions is as shown in Fig. 4.2a. The 780 nm probe and control lasers are generated from two different laser diodes (Thorlabs L785H1) which are home-assembled extended cavity diode lasers (ECDLs) with typical linewidth of 500 kHz [107]. The probe laser beam is split in two main parts. The first beam is sent to the interferometry set-up while the second is sent to the saturated absorption spectroscopy (SAS) set-up for laser locking and stabilization. It should be noted that, in this particular case, we have two closed transitions: $5S_{1/2}(F = 2) \rightarrow 5P_{3/2}(F = 3)$ and $5S_{1/2}(F = 1) \rightarrow 5P_{3/2}(F = 0)$. The appearance of these two peaks can be attributed to saturation effects. In addition, the peaks from other transitions are a result of subDoppler hyperfine pumping [108].

In the interferometry set-up, the probe beam is directed to the Rb vapour cell at room temperature and into the photodetector. The photodetector (Thorlabs APD430A2) employed has a sufficient bandwidth from DC to 400 MHz. The probe beam is linearly polarized which can be decomposed into the superposition of two circularly polarized components (left and right-handed) with equal amplitudes that couples the different magnetic sublevels according to the selection rule $\Delta m_F = \pm 1$ leading to the formation of a Λ-type system with ground state $5S_{3/2}(F = 1)$ and excited state $5P_{3/2}(F = 1)$. Next, the control laser beam is also split into two main parts. The first beam is again sent to the SAS set-up for laser locking and stabilization while the second beam is directed to the interferometry set-up. In the interferometry set-up, the second beam is further split into two beams using a PBS and then recombined in another PBS forming the two arms of the interferometer, but their polarizations are orthogonal to each other. The two beams are then made circularly polarized before entering the cell by using a $\lambda/4$ waveplate at 45° to the optic axis and counter-propagated with the probe beam from the first laser in the cell. The two circularly polarized beams couples the different magnetic sublevels according to the selection rule $\Delta m_F = \pm 1$ which leads to the formation of another Λ-type system. This second Λ-type system has the same ground states $5S_{3/2}(F = 1)$ as the first Λ-type system but with different excited state $5P_{3/2}(F = 0)$. Thus, we obtain a closed loop double Λ-type system as shown in Fig. 4.1b. A mirror actuated by a

piezoelectric transducer (PZT) (Thorlabs AE0203D04F) is installed in one of the arms of the interferometer to vary the phase in order to monitor the phase sensitivity of the system.

Since the bandwidth of the PZT is only up to few KHz, so in order to have phase variation at high frequency we introduce the frequency difference between the two arms using AOMs. The frequency of the laser can be tuned in one of the arms of the interferometer by using the AOM arrangement given in figure. This is done by sending one of the control beams through two AOMs, one of which is downshifted by 72 MHz and the other is upshifted to around 72 MHz. It is worth noting that we selected 72 MHz for the AOM frequency based on the availability of RF signal sources and the bandwidth of the AOM. The vapour cell is kept inside a double layer mu-metal magnetic shield. The vapour cell also has a solenoid arrangement for the magnetic field variation along the direction of the probe beam. The solenoid has 80 turns, a diameter of 4.5 cm and length of 11 cm.

4.2.5 Set-up II: Double Λ-type system at 780 nm and 420 nm transition

The experimental set-up of the double Λ-type systems in ^{87}Rb at 780 nm and 420 nm transition is given in Fig. 4.2b. The 780 nm beam is generated from the same home-assembled ECDL used above and is used as the probe. The probe laser beam is again split into two main parts: one part is sent to the SAS set-up for locking and the other is sent to the interferometry set-up. The 420 nm control laser beam is generated from a commercially available ECDL (Toptica DL PRO HP) with a typical linewidth of less than 200 kHz and output power of 70 mW. The 420 nm control beam is also aligned in a similar fashion as above where it is split into two parts. The first part is used for the frequency locking and stabilization to the $5S_{3/2}(F = 1) \rightarrow 6P_{3/2}(F = 2)$ transition. The second part is further split using a PBS and recombined in another PBS forming the two arms of the interferometer but with polarizations that are orthogonal to each other. The two beams are then made circularly polarized before entering the cell by using a $\lambda/4$ waveplate at 45° to the optic axis and co-propagated with the probe beam from the first laser in the cell. Each of the two arms are passed through an AOM where they are downshifted by 75 MHz such that they are both resonant to the $5S_{3/2}(F = 1) \rightarrow 6P_{3/2}(F = 0)$ transition.

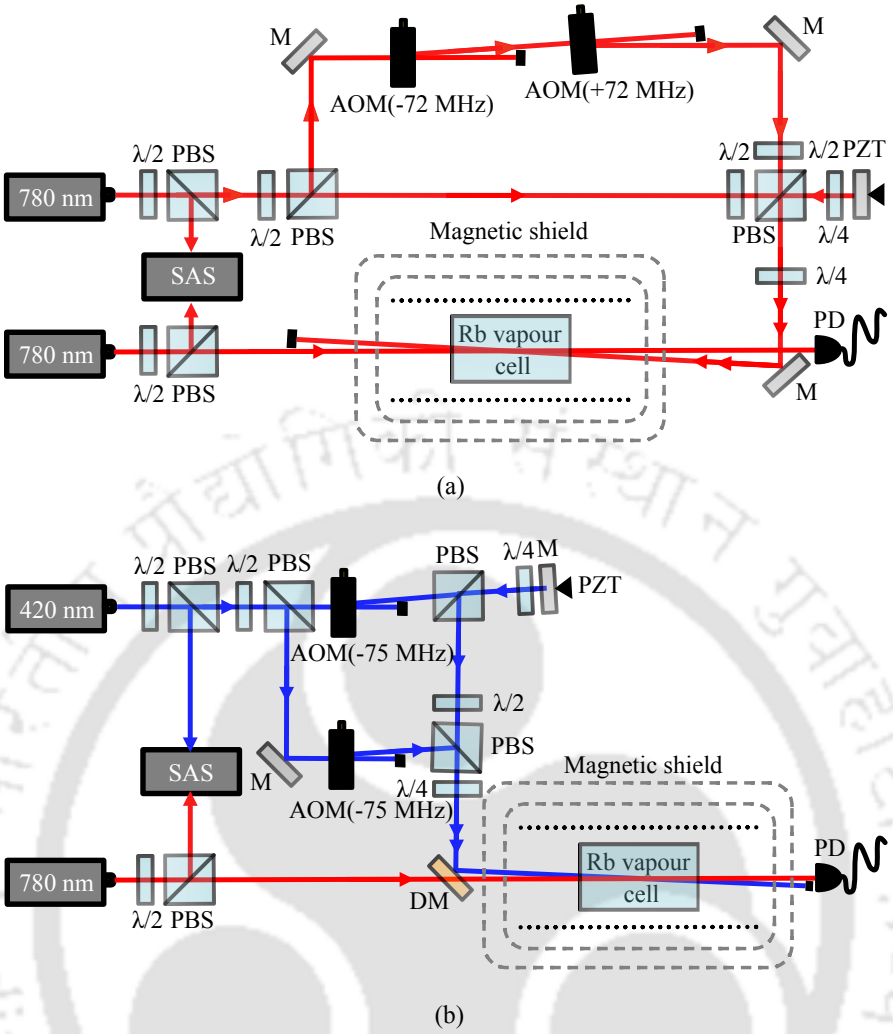

FIGURE 4.2: (a) Schematic of the experimental set-up for the double Λ-type system in ^{87}Rb at 780nm (b) Schematic of the experimental set-up for the double Λ-type system in ^{87}Rb at 780nm and 420nm transitions. M: mirror; DM: dichroic Mirror; PZT: piezoelectric transducer; $\lambda/2$: half waveplate; $\lambda/4$: quarter waveplate; PBS: polarizing beamsplitter; AOM: acousto-optic modulator; PD: photodetector; SAS: saturated absorption spectroscopy of rubidium for probe beam and control beam.

Any of the AOMs in either arms can be employed for the frequency variation of the laser for the study of phase sensitivity and the frequency response of the system.

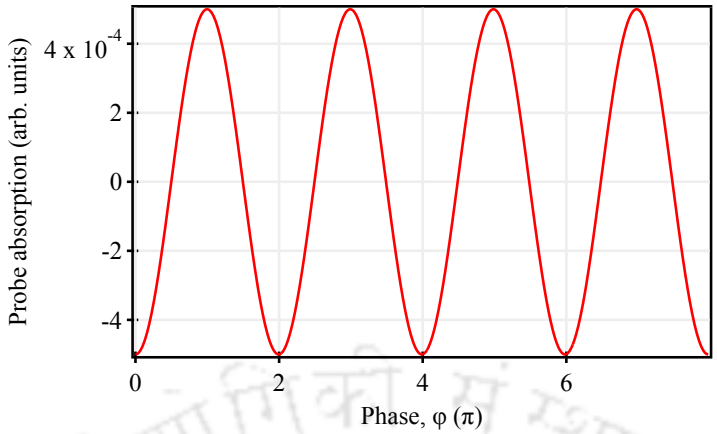

FIGURE 4.3: Theoretical plot of $\mathrm{Im}(\rho_{12}) + \mathrm{Im}(\rho_{32})$ vs change in phase, ϕ with $\Omega_{12} = \Omega_{32} = 0.01\Gamma_2$, $\Omega_{14} = \Omega_{34} = \Gamma_2$ and $\Delta_{12} = \Delta_{23} = \Delta_{34} = \Delta_{14} = 0$.

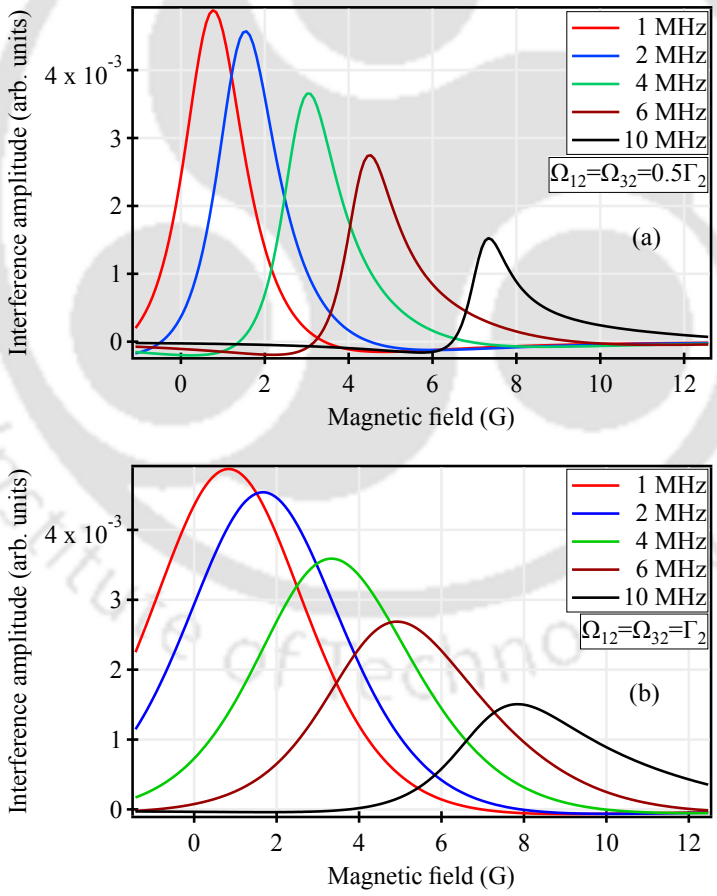

FIGURE 4.4: Theoretical plot of the interference amplitude of $\mathrm{Im}(\rho_{12}^{+1})$+$\mathrm{Im}(\rho_{32}^{+1})$ vs the magnetic field B in Gauss at five different detuning of the control laser, Δ_{14} =1, 2, 4, 6, 10 ($2\pi\times$ MHz) with $\Gamma_1 = \Gamma_2 = 2\pi\times 6$ MHz for (a) $\Omega_{14} = \Omega_{34} = 0.01\Gamma_2$ and $\Omega_{12} = \Omega_{32} = 0.5\Gamma_2$, and (b) $\Omega_{14} = \Omega_{34} = 0.01\Gamma_2$ and $\Omega_{12} = \Omega_{32} = \Gamma_2$.

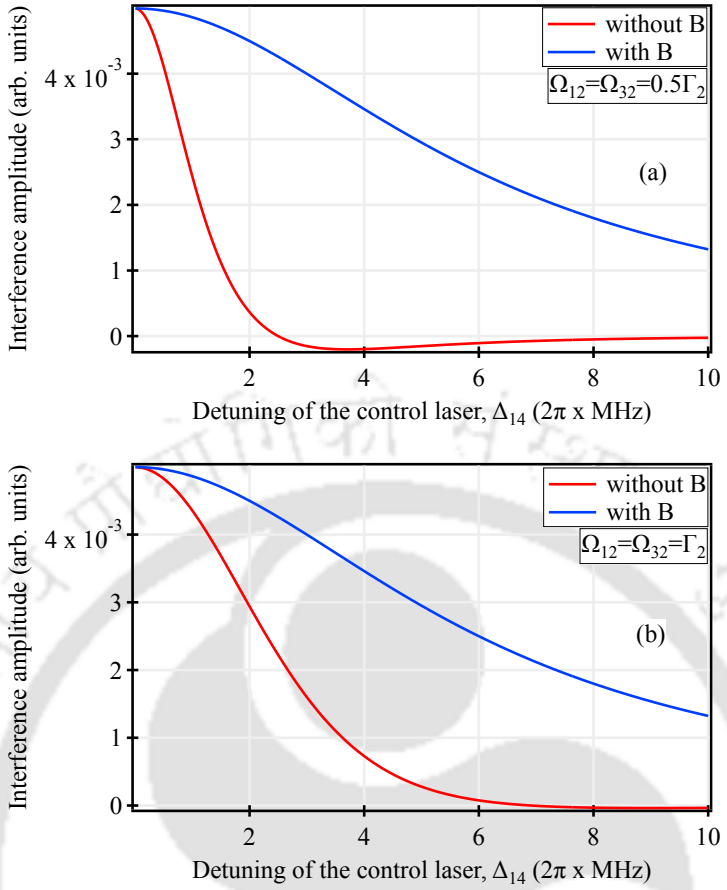

FIGURE 4.5: Theoretical plot of the interference amplitude of $\mathrm{Im}(\rho_{12}^{+1})$+$\mathrm{Im}(\rho_{32}^{+1})$ vs the detuning of the control laser, Δ_{14} in absence and in presence of the magnetic field B with $\Gamma_2 = \Gamma_4 = 2\pi\times6$ MHz for (a) $\Omega_{14} = \Omega_{34} = 0.01\Gamma_2$ and $\Omega_{12} = \Omega_{32} = 0.5\Gamma_2$, and (b) $\Omega_{14} = \Omega_{34} = 0.01\Gamma_2$ and $\Omega_{12} = \Omega_{32} = \Gamma_2$.

4.3 Theoretical formulation

The Hamiltonian, H of the double Λ-type system as shown in Fig. 4.1 under the electric-dipole and rotating-wave approximation and in rotating frame is expressed as

$$H = \hbar\big[0\,|1\rangle\langle 1| - \Delta_{12}\,|2\rangle\langle 2| - (\Delta_{12}-\Delta_{23})\,|3\rangle\langle 3| - (\Delta_{12}-\Delta_{23}+\Delta_{34})\,|4\rangle\langle 4|\,\big] + \left[\frac{\Omega_{12}}{2}\,|1\rangle\langle 2| + \frac{\Omega_{23}}{2}\,|2\rangle\langle 3| + \frac{\Omega_{34}}{2}\,|3\rangle\langle 4| + \frac{\Omega_{14}}{2}e^{-i(\Delta_{12}-\Delta_{23}+\Delta_{34}-\Delta_{14})t}\,|1\rangle\langle 4| + h.c.\right] \tag{4.1}$$

where Ω_{12}, Ω_{23}, Ω_{34} and Ω_{14} are the Rabi frequencies with corresponding detunings Δ_{12}, Δ_{23}, Δ_{34} and Δ_{14} driving the transitions $|1\rangle \rightarrow |2\rangle$, $|3\rangle \rightarrow |2\rangle$, $|1\rangle \rightarrow |4\rangle$ and $|3\rangle \rightarrow |4\rangle$ respectively. The Rabi frequency is defined as $\Omega_{ij} = d_{ij}E_{ij}e^{i\phi_{ij}}/\hbar$ for the $|i\rangle \rightarrow |j\rangle$

transition with d_{ij} as the dipole moment matrix element, E_{ij} as the amplitude of the electromagnetic field and ϕ_{ij} as the phase.

The evolution of the system is described by the Liouville-von Neumann equation for the density matrix

$$\dot{\rho} = -\frac{i}{\hbar}[H, \rho] - \frac{1}{2}\{\Gamma, \rho\}, \tag{4.2}$$

where ρ is the atomic density operator and Γ is the relaxation operator [78]. The substitution of Eq. 4.1 into Eq. 4.2 gives the following set of equations of motion with time-dependent coefficients

$$\begin{aligned}
\dot{\rho}_{11} &= -i\frac{\Omega_{12}}{2}\rho_{21} - i\frac{\Omega_{14}}{2}e^{-i\delta t}\rho_{41} + i\frac{\Omega_{12}^*}{2}\rho_{12} + i\frac{\Omega_{14}^*}{2}e^{i\delta t}\rho_{14} + \Gamma_{21}\rho_{22} + \Gamma_{41}\rho_{44},\\
\dot{\rho}_{12} &= i\frac{\Omega_{12}}{2}(\rho_{11} - \rho_{22}) - i\frac{\Omega_{14}}{2}e^{-i\delta t}\rho_{42} + i\frac{\Omega_{32}^*}{2}\rho_{13} - \gamma_{12}\rho_{12},\\
\dot{\rho}_{13} &= -i\frac{\Omega_{12}}{2}\rho_{23} - i\frac{\Omega_{14}}{2}e^{-i\delta t}\rho_{43} + i\frac{\Omega_{32}}{2}\rho_{12} + i\frac{\Omega_{34}^*}{2}\rho_{14} - \gamma_{13}\rho_{13},\\
\dot{\rho}_{14} &= -i\frac{\Omega_{12}}{2}\rho_{24} + i\frac{\Omega_{14}}{2}e^{-i\delta t}(\rho_{11} - \rho_{44}) + i\frac{\Omega_{34}}{2}\rho_{13} - \gamma_{14}\rho_{14},\\
\dot{\rho}_{22} &= -i\frac{\Omega_{12}^*}{2}\rho_{12} - i\frac{\Omega_{32}}{2}\rho_{32} + i\frac{\Omega_{12}}{2}\rho_{12} + i\frac{\Omega_{32}^*}{2}\rho_{23} - \Gamma_{21}\rho_{22} - \Gamma_{31}\rho_{22},\\
\dot{\rho}_{23} &= -i\frac{\Omega_{12}^*}{2}\rho_{13} - i\frac{\Omega_{32}}{2}(\rho_{33} - \rho_{22}) + i\frac{\Omega_{34}^*}{2}\rho_{24} - \gamma_{23}\rho_{23},\\
\dot{\rho}_{24} &= -i\frac{\Omega_{12}^*}{2}\rho_{14} - i\frac{\Omega_{32}}{2}\rho_{34} + i\frac{\Omega_{14}}{2}e^{-i\delta t}\rho_{21} + i\frac{\Omega_{34}}{2}\rho_{23} - \gamma_{24}\rho_{24},\\
\dot{\rho}_{33} &= -i\frac{\Omega_{32}^*}{2}\rho_{23} - i\frac{\Omega_{34}}{2}\rho_{43} + i\frac{\Omega_{32}}{2}\rho_{32} + i\frac{\Omega_{34}^*}{2}\rho_{34} - \Gamma_{23}\rho_{22} - \Gamma_{43}\rho_{44},\\
\dot{\rho}_{44} &= -i\frac{\Omega_{14}^*}{2}e^{i\delta t}\rho_{14} - i\frac{\Omega_{34}^*}{2}\rho_{34} + i\frac{\Omega_{14}}{2}e^{-i\delta t}\rho_{41} + i\frac{\Omega_{34}}{2}\rho_{43} - \Gamma_{41}\rho_{11} - \Gamma_{34}\rho_{33},
\end{aligned} \tag{4.3}$$

where $\delta = \Delta_{12} - \Delta_{32} + \Delta_{34} - \Delta_{14}$, $\gamma_{12} = i\Delta_{12} + \gamma_{12}^{dec}$, $\gamma_{13} = i(\Delta_{12} - \Delta_{32}) + \gamma_{13}^{dec}$, $\gamma_{14} = i(\Delta_{12} - \Delta_{32} - \Delta_{34}) + \gamma_{14}^{dec}$, $\gamma_{23} = -i\Delta_{32} + \gamma_{32}^{dec}$, $\gamma_{24} = i(-\Delta_{32} + \Delta_{34}) + \gamma_{24}^{dec}$ and $\gamma_{ij}^{dec} = \frac{1}{2}(\Gamma_i + \Gamma_j)$ is the decoherence rate between level $|i\rangle$ and $|j\rangle$.

In the four photon resonance ($\Delta_{12} - \Delta_{23} + \Delta_{34} - \Delta_{14} = 0$) condition, the Hamiltonian in Eq. 4.1 will be time independent and the probe absorption given by $\mathrm{Im}(\rho_{12}) + \mathrm{Im}(\rho_{32})$ is plotted in Fig. 4.3 with the change in phase ϕ, where $\phi = \phi_{12} - \phi_{23} - \phi_{34} - \phi_{14}$. This plot is obtained by varying the phase of the control laser, Ω_{14} in one of the arms of the interferometer. The sinusoidal behaviour from this plot shows the phase dependence of the system.

In order to have phase variation at high frequency, we need to introduce a frequency difference between the two arms of the interferometer by detuning one of the control fields which causes non-zero four-photon detuning and the above equations of motion are now time dependent. The time dependent equations can be solved using the Floquet expansion given by

$$\rho_{ij}(t) = \sum_{n=-\infty}^{\infty} \rho_{ij}^{(n)}(t) e^{in\delta t}, \tag{4.4}$$

where $\rho_{ij}^{(n)}(t)$ are the n^{th} harmonic amplitudes. Substitution of Eq. 4.4 in Eq. 4.3 and comparing the coefficients with same factor $e^{in\delta t}$, the time dependence of the equations of motion is removed which yields the following set of steady state equations of motion for the slowly varying harmonic amplitudes.

$$\begin{aligned}
\dot{\rho}_{11}^{(n)} &= -in\delta\rho_{11}^{(n)} - i\frac{\Omega_{12}}{2}\rho_{21}^{(n)} - i\frac{\Omega_{14}}{2}\rho_{41}^{(n+1)} + i\frac{\Omega_{12}^{*}}{2}\rho_{12}^{(n)} + i\frac{\Omega_{14}^{*}}{2}\rho_{14}^{(n-1)} + \Gamma_{21}\rho_{22}^{(n)} + \Gamma_{41}\rho_{44}^{(n)},\\
\dot{\rho}_{12}^{(n)} &= -in\delta\rho_{12}^{(n)} + i\frac{\Omega_{12}}{2}(\rho_{11}^{(n)} - \rho_{22}^{(n)}) - i\frac{\Omega_{14}}{2}\rho_{42}^{(n+1)} + i\frac{\Omega_{32}^{*}}{2}\rho_{13}^{(n)} - \gamma_{12}\rho_{12}^{(n)},\\
\dot{\rho}_{13}^{(n)} &= -in\delta\rho_{13}^{(n)} - i\frac{\Omega_{12}}{2}\rho_{23}^{(n)} - i\frac{\Omega_{14}}{2}\rho_{43}^{(n+1)} + i\frac{\Omega_{32}}{2}\rho_{12}^{(n)} + i\frac{\Omega_{34}^{*}}{2}\rho_{14}^{(n)} - \gamma_{13}\rho_{13}^{(n)},\\
\dot{\rho}_{14}^{(n)} &= -in\delta\rho_{14}^{(n)} - i\frac{\Omega_{12}}{2}\rho_{24}^{(n)} + i\frac{\Omega_{14}}{2}(\rho_{11}^{(n+1)} - \rho_{44}^{(n+1)}) + i\frac{\Omega_{34}}{2}\rho_{13}^{(n)} - \gamma_{14}\rho_{14}^{(n)},\\
\dot{\rho}_{22}^{(n)} &= -in\delta\rho_{22}^{(n)} - i\frac{\Omega_{12}^{*}}{2}\rho_{12}^{(n)} - i\frac{\Omega_{32}}{2}\rho_{32}^{(n)} + i\frac{\Omega_{12}}{2}\rho_{12}^{(n)} + i\frac{\Omega_{32}^{*}}{2}\rho_{23}^{(n)} - \Gamma_{21}\rho_{22}^{(n)} - \Gamma_{31}\rho_{22}^{(n)},\\
\dot{\rho}_{23}^{(n)} &= -in\delta\rho_{23}^{(n)} - i\frac{\Omega_{12}^{*}}{2}\rho_{13}^{(n)} - i\frac{\Omega_{32}}{2}(\rho_{33}^{(n)} - \rho_{22}^{(n)}) + i\frac{\Omega_{34}^{*}}{2}\rho_{24}^{(n)} - \gamma_{23}\rho_{23}^{(n)},\\
\dot{\rho}_{24}^{(n)} &= -in\delta\rho_{24}^{(n)} - i\frac{\Omega_{12}^{*}}{2}\rho_{14}^{(n)} - i\frac{\Omega_{32}}{2}\rho_{34}^{(n)} + i\frac{\Omega_{14}}{2}\rho_{21}^{(n+1)} + i\frac{\Omega_{34}}{2}\rho_{23}^{(n)} - \gamma_{24}\rho_{24}^{(n)},\\
\dot{\rho}_{33}^{(n)} &= -in\delta\rho_{33}^{(n)} - i\frac{\Omega_{32}^{*}}{2}\rho_{23}^{(n)} - i\frac{\Omega_{34}}{2}\rho_{43}^{(n)} + i\frac{\Omega_{32}}{2}\rho_{32}^{(n)} + i\frac{\Omega_{34}^{*}}{2}\rho_{34}^{(n)} - \Gamma_{23}\rho_{22}^{(n)} - \Gamma_{43}\rho_{44}^{(n)},\\
\dot{\rho}_{44}^{(n)} &= -in\delta\rho_{44}^{(n)} - i\frac{\Omega_{14}^{*}}{2}\rho_{14}^{(n-1)} - i\frac{\Omega_{34}^{*}}{2}\rho_{34}^{(n)} + i\frac{\Omega_{14}}{2}\rho_{41}^{(n+1)} + i\frac{\Omega_{34}}{2}\rho_{43}^{(n)} - \Gamma_{41}\rho_{11}^{(n)} - \Gamma_{34}\rho_{33}^{(n)},
\end{aligned} \tag{4.5}$$

It is difficult to derive an analytical solution of the various harmonic components of the density matrix but the equation can be solved numerically and we have truncated the order at n=2. The zeroth order given by $\mathrm{Im}(\rho_{12}^{(0)}) + \mathrm{Im}(\rho_{32}^{(0)})$ gives the DC component of the probe absorption. The $\mathrm{Im}(\rho_{12}^{(-1)}) + \mathrm{Im}(\rho_{32}^{(-1)})$, $\mathrm{Im}(\rho_{12}^{(+1)}) + \mathrm{Im}(\rho_{32}^{(+1)})$ and $\mathrm{Im}(\rho_{12}^{(-2)}) + \mathrm{Im}(\rho_{32}^{(-2)})$, $\mathrm{Im}(\rho_{12}^{(+2)}) + \mathrm{Im}(\rho_{32}^{(+2)})$ gives the first harmonics and second harmonics and so on of the probe absorption. For small Rabi frequencies of the probe field compared to the control field, the amplitude of the second harmonics is very small.

The plot for the amplitude of probe absorption of the first harmonic given by $\mathrm{Im}(\rho_{12}^{(+1)})+\mathrm{Im}(\rho_{32}^{(+1)})$ with the change in the magnetic field at different control field detunings, Δ_{14} and $\Omega_{14} = \Omega_{34} = 0.5\Gamma_2$ is given in Fig. 4.4a. When the magnetic field is absent (i.e., $B = 0$), levels $|1\rangle$ and $|3\rangle$ are degenerate. In presence of magnetic field applied along the direction of the probe field, the degeneracy is lifted and the shift in levels are given by the Zeeman shift, $\Delta_B = \mathrm{g}_F\mathrm{m}_F\mu_B\mathrm{B}$ where g_F is the Landé g factor, m_F is the magnetic quantum number and μ_B is the Bohr magneton. For the ground state $5\mathrm{S}_{3/2}(\mathrm{F} = 1)$ of ^{87}Rb, g_F=-1/2 and for m_F=1, we have $\Delta_B = 1.4$ MHz when B = 1 G. With the increase in strength of the magnetic field, the shift in the levels for $|1\rangle$ and $|3\rangle$ are enhanced and are given by $\Delta_B/2$ and $-\Delta_B/2$ respectively. When magnetic field increases to a value $B = \Delta_{14}/1.4$ MHz, the amplitude of the interference reaches a maximum value as the two-photon resonance $(\Delta_{34} - \Delta_{14} = 0)$ condition is now satisfied. When B further increases, the amplitude of the interference decreases as the two-photon resonance condition is no longer satisfied. This can be used to optimize the amplitude of the interference by properly adjusting the magnetic field. The peaks are fitted to a Lorentzian, and each fit yields a linewidth of around (1.5 ± 0.1) G ((2.1 ± 0.1) MHz). Fig. 4.4b presents the same plot of the amplitude of probe absorption with magnetic field, but with higher Rabi frequency of control fields $\Omega_{14} = \Omega_{34} = 1\Gamma_2$. This plot simply shows the power broadening effect of the control fields on the Lorentzian peaks. The peaks are fitted to a Lorentzian, and each fit yields a linewidth of around (5.5 ± 0.1) G ((7.7 ± 0.1) MHz).

In order to study the frequency response of the system, we now plot the amplitude of probe absorption with the detuning of the control field Δ_{14} and $\Omega_{14} = \Omega_{34} = 0.5\Gamma_2$ in Fig. 4.5a. The red and blue curve corresponds to the amplitude of interference in absence and in presence of the magnetic field respectively. The blue curve is obtained by setting the value of B such that the interference amplitude is maximized as discussed above. We can clearly see that the magnetic field enhances the frequency response of the system. The plots are fitted to a Lorentzian and the linewidth in absence and in presence of the magnetic field is around (2.5 ± 0.1) MHz and (12 ± 0.1) MHz respectively. Fig. 4.4b presents the same plot of amplitude of probe absorption with the detuning of the control field Δ_{14}, but with higher Rabi frequency of control fields $\Omega_{14} = \Omega_{34} = \Gamma_2$. This plot

simply shows the power broadening effect of the control fields on the frequency response curve. The plots are fitted to a Lorentzian and the linewidth in absence and in presence of the magnetic field is around 6 MHz and 12 MHz respectively. We also see similar behaviour in the case of excited states with different decay rates ($\Gamma_2 = 2\pi\times$ 6 MHz and $\Gamma_4 = 2\pi\times$ 1.4 MHz) of the double Λ-type system.

4.4 Experimental Results

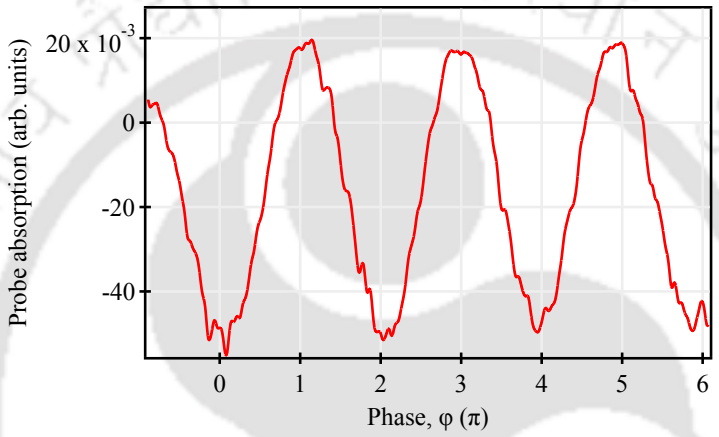

FIGURE 4.6: The probe absorption vs the change in phase, ϕ of the double Λ-type system in Fig. 4.1b which involves the excited states with same decay rates ($\Gamma_2 = \Gamma_4 = 2\pi\times$ 6 MHz) at 780 nm transition.

4.4.1 Double Λ-type system at 780 nm transition

In order to monitor the phase sensitivity of the closed loop double Λ-type system which involves the excited states with same decay rates at 780 nm transitions in Fig. 4.1b, we plot the probe absorption from the photodetector as a function of the change of phase, ϕ and is shown in Fig. 4.6. This plot is obtained by introducing a phase difference between the two arms of the interferometer by employing a mirror driven by a PZT as shown in the set-up given in Fig. 4.2a. When $\phi = 2n\pi$ radians, two waves are in phase they interfere constructively and when $\phi = (2n+1)\pi$ radians, the two waves are out of phase and they interfere destructively and cancel each other out. The difference between the maxima and minima is scaled to π and is consistent with the voltage calibration for PZT that was employed.

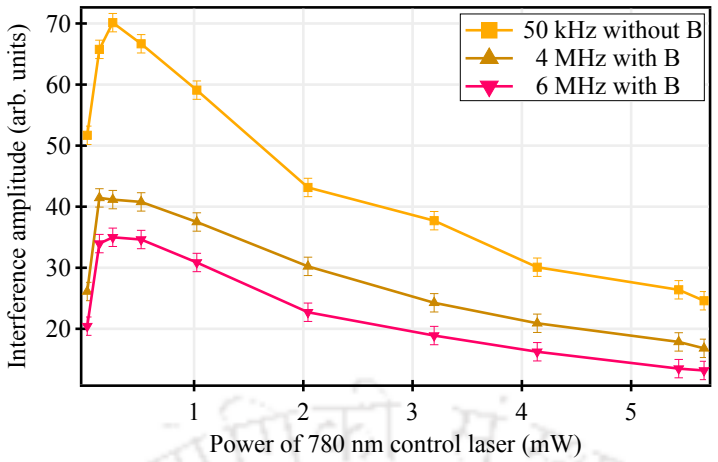

FIGURE 4.7: The interference amplitude vs the power of the 780 nm control laser in mW at different detuning of the control laser frequency, Δ_{14} =0.5, 4 and 6 ($2\pi\times$ MHz) of the double Λ-type system in Fig. 4.1b which involves the excited states with same decay rates ($\Gamma_2 = \Gamma_4 = 2\pi\times$ 6 MHz) at 780 nm transitions.

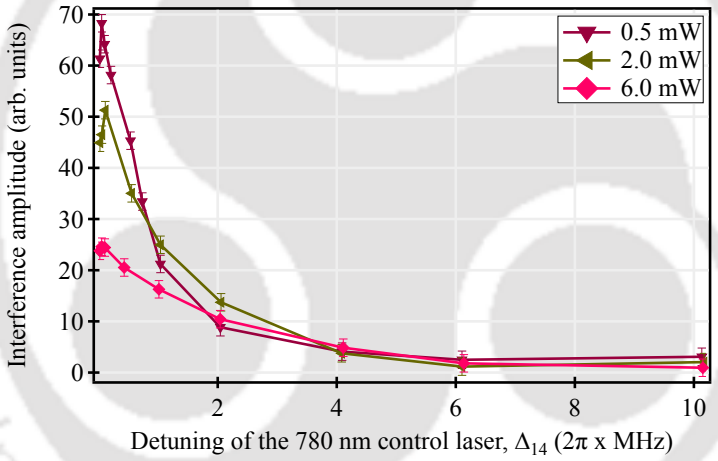

FIGURE 4.8: The interference amplitude vs the detuning of the 780 nm control laser, Δ_{14} in MHz of the double Λ-type system in Fig. 4.1b which involves the excited states with same decay rates ($\Gamma_2 = \Gamma_4 = 2\pi\times$ 6 MHz) at 780 nm transitions. Plots are shown for three different powers of the 780 nm control laser: 0.5, 2 and 6 mW.

To ensure that a change in voltage applied to the PZT results in a change of phase in the interferometer, a voltage calibration was performed. The calibration involved measuring the relationship between the voltage applied to the PZT and the corresponding change in the position of the mirror attached to it. In this particular case, a displacement of 0.39 μm is required for a phase difference of 2π, which corresponds to a PZT voltage of 13 V. So, for four fringes, a PZT voltage of (52 $\pm$ 2)V is required which is consistent with Fig. 4.6.

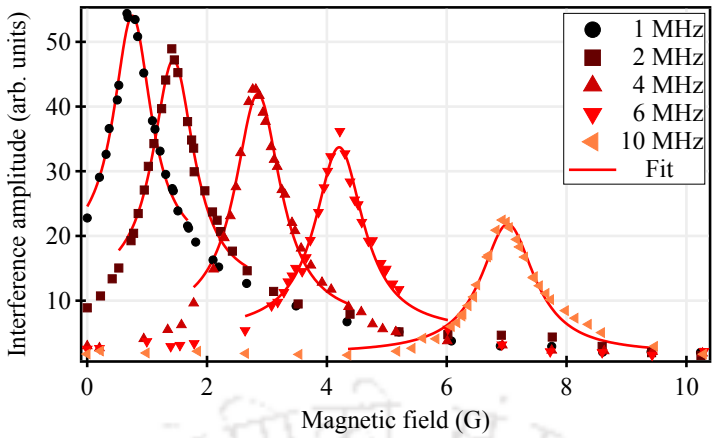

FIGURE 4.9: The interference amplitude vs the magnetic field in Gauss at different detunings of the 780 nm control laser frequency, Δ_{14} =1, 2, 4, 6 and 10 ($2\pi\times$ MHz) of the double Λ-type system in Fig. 4.1b which involves the excited states with same decay ($\Gamma_2 = \Gamma_4 = 2\pi\times$ 6 MHz) rates at 780 nm transitions.

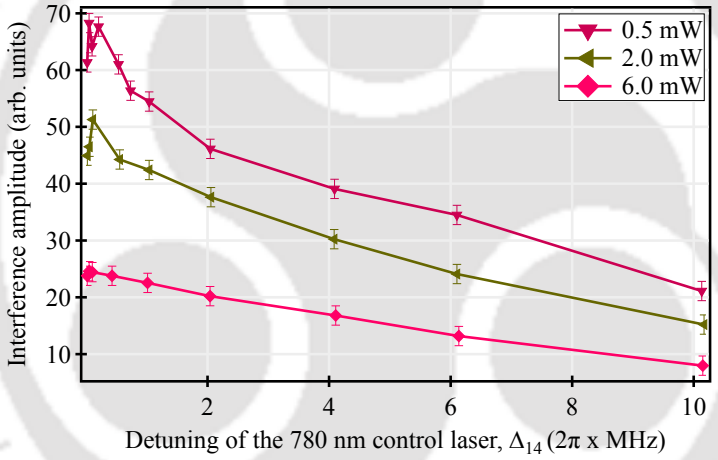

FIGURE 4.10: The interference amplitude vs the detuning of the 780 nm control laser, Δ_{14} in the presence of magnetic field of the double Λ-type system in Fig. 4.1b which involves the excited states with same decay rates ($\Gamma_2 = \Gamma_4 = 2\pi\times$ 6 MHz) at 780 nm transitions. Plots are shown for three different powers of the 780 nm control laser: 0.5, 2 and 6 mW.

We now study the frequency response of this system. In order to begin, we must first investigate the effect of the power of the 780 nm control laser on the amplitude of probe absorption. The plot of the amplitude of probe absorption with change in the control laser power at three different control laser frequency detunings, Δ_{14} is shown in Fig. 4.7. According to this plot, the maximum interference amplitude is at around 500 μW, thus we set the control power at this value. When the power of 780 nm control laser is further increased, the interference amplitude decreases as the atoms are optically pumped to the

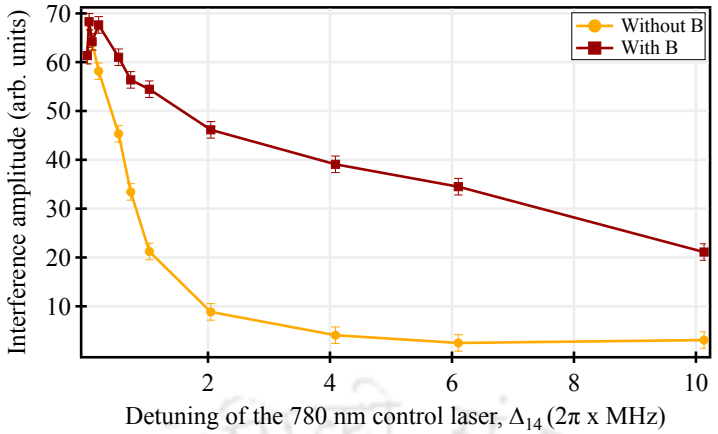

FIGURE 4.11: The interference amplitude vs the detuning of the 780 nm control laser, Δ_{14} in absence and in presence of the magnetic field of the double Λ-type system in Fig. 4.1b which involves the excited states with same decay rates ($\Gamma_2 = \Gamma_4 = 2\pi\times$ 6 MHz) at 780 nm transitions. The power of the probe and control lasers are kept at 0.02 mW and 0.5 mW respectively.

other ground state $5S_{1/2}$(F=2) as the system is not perfectly closed. We then plot the amplitude of probe absorption with change in the control laser detuning, Δ_{14} at three different powers of the 780 nm control laser and is shown in Fig. 4.8. The plot is obtained by detuning the frequency of the control laser in one of the arms of the interferometer using the AOM arrangement as shown in the set-up given in Fig. 4.2a and measuring the amplitude of the interference signal obtained at every frequency detuning.

We also study the frequency response of this system in the presence of a magnetic field. In order to do this, we must first optimize the magnetic field strength for a particular control laser frequency detuning as described above. Therefore, while keeping the control laser frequency detuning fixed, we vary the magnetic field such that the interference amplitude is maximized. This occurs as a result of the magnetic field lifting the degeneracy of magnetic sublevels such that the two-photon resonance condition is satisfied. The plot of the amplitude of probe absorption with the change in magnetic field at various control frequency detunings is shown in Fig. 4.9 and each peak depicts this behaviour. The peaks are fitted to a Lorentzian, and each fit yields a linewidth of around (0.7 ± 0.1) G ((1.0 ± 0.1) MHz). Next, we plot the amplitude of probe absorption with the detuning of the 780 nm control laser, Δ_{14} at three different powers of the 780 nm control laser but in the presence of a magnetic field and is shown in Fig. 4.10. The plot is obtained

by measuring the interference amplitude at every control laser detuning after it has been optimize using the magnetic field such that it is maximum.

Further, we plot the amplitude of probe absorption with the detuning of the 780 nm control laser, Δ_{14} in absence and in presence of a magnetic field at optimum power and is shown in Fig. 4.11. The plot shows that the frequency response is improved in the presence of the magnetic field. The yellow and brown curve corresponds to the amplitude of interference in absence and in presence of the magnetic field respectively. The plots are fitted to a Lorentzian and the linewidth in absence and in presence of the magnetic field is around (1.5 ± 0.1) MHz and (8.4 ± 0.1) MHz respectively.

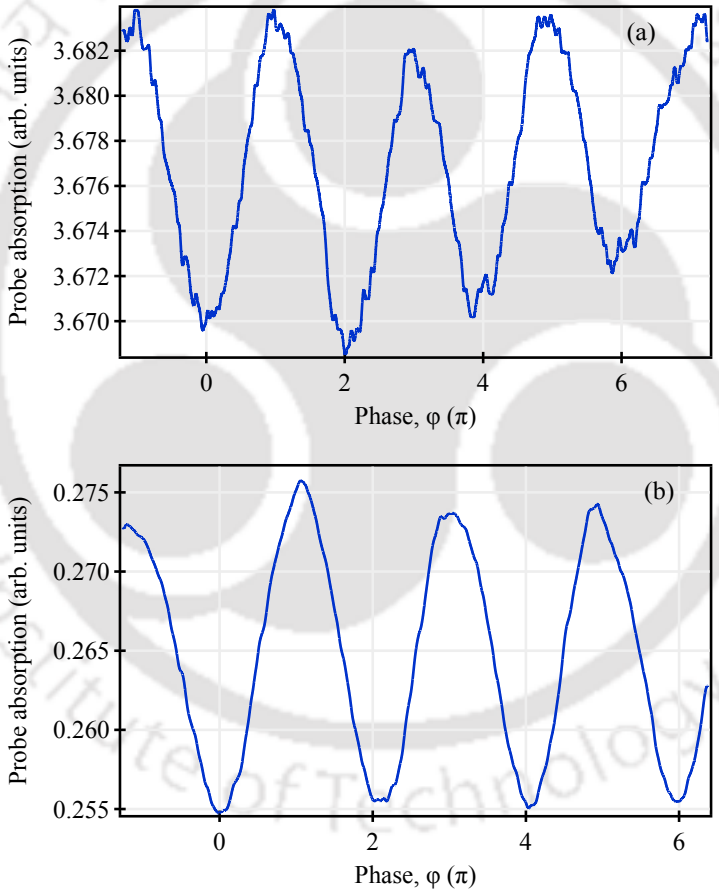

FIGURE 4.12: The probe absorption vs the change in phase ϕ of the double Λ-type system which involves the excited states with different decay rates ($\Gamma_2 = 2\pi\times$ 6 MHz and $\Gamma_4 = 2\pi\times$ 1.4 MHz) at 780 nm and 420 nm transitions when (a) probe laser is locked to $5S_{3/2}(F = 1) \rightarrow 5P_{3/2}(F = 0)$ in Fig. 4.1c, and (b) probe laser is locked to $5S_{3/2}(F = 1) \rightarrow 5P_{3/2}(F = 1)$ in Fig. 4.1d.

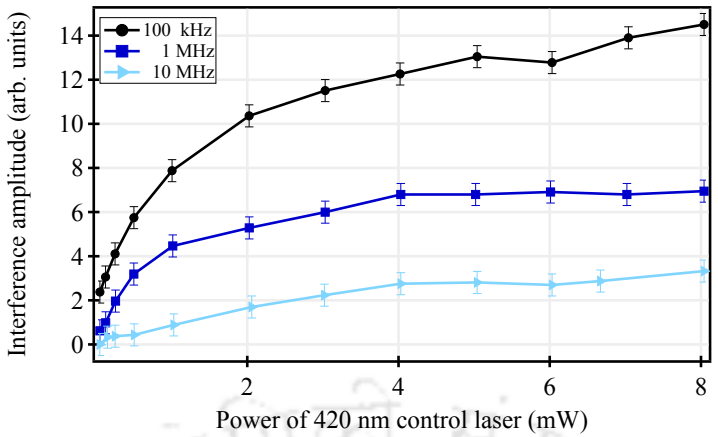

FIGURE 4.13: The interference amplitude vs the power of the 420 nm control laser in mW at various detuning of the 420 nm control laser, Δ_{14} =0.1, 1 and 10 ($2\pi\times$ MHz) for the double Λ-type system in Fig. 4.1d. which involves the excited states with different decay rates ($\Gamma_2 = 2\pi\times$ 6 MHz and $\Gamma_4 = 2\pi\times$ 1.4 MHz) at 780 nm and 420 nm transitions.

4.4.2 Double Λ-type system at 780 nm transition and 420 nm transition

Similarly, we monitor the phase sensitivity of the closed loop double Λ-type systems which involves the excited states with different decay rates at 780 nm and 420 nm transitions in Fig. 4.1c and Fig. 4.1d. We again plot the probe absorption from the photodetector as a function of the change of phase between the two arms of the interferometer, ϕ and is shown in Fig. 4.12a and Fig. 4.12b. The sinusoidal behaviour from these plots shows phase sensitivity of the two systems.

We now study the frequency response of the two systems given in Fig. 4.1c and Fig. 4.1d similar to Fig. 4.1b as described above. We first investigate the effect of the power of the 420 nm control laser on the amplitude of probe absorption. The plot of the amplitude of probe absorption with the change in the 420 nm control laser power at three different control laser detunings, Δ_{14} is shown in Fig. 4.13. According to this plot, the maximum interference signal amplitude is at around 8 mW, thus we set the control power at this value. We then plot the amplitude of probe absorption with change in the control laser detuning, Δ_{14} at three different powers of the 420 nm control laser and is shown in Fig. 4.14a and Fig. 4.14b. The plot is obtained by detuning the frequency of the 420 nm control laser in one of the arms of the interferometer using the AOM arrangement as

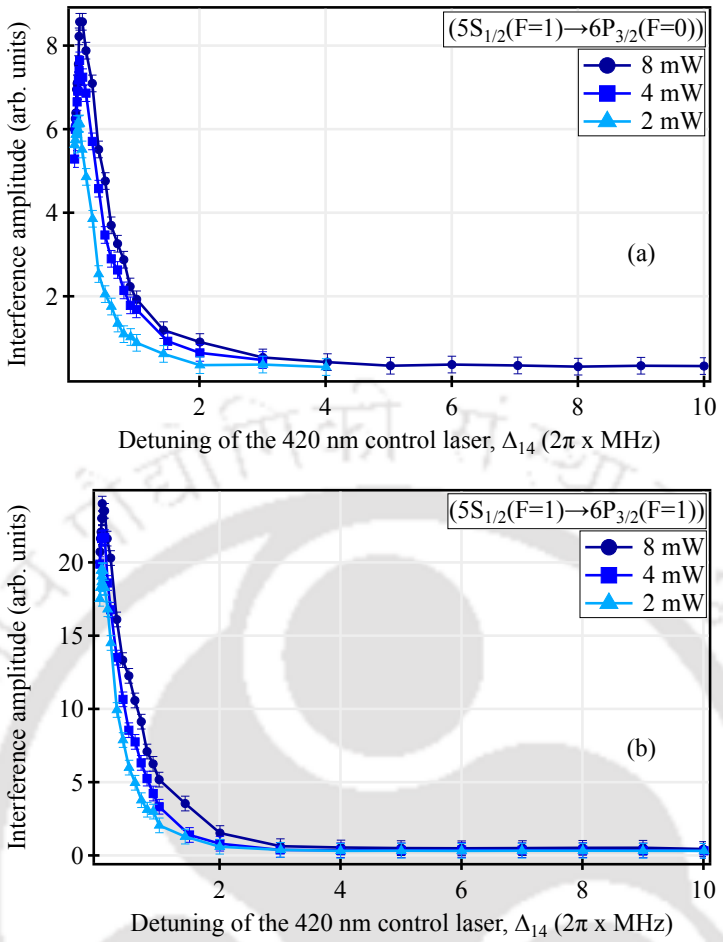

FIGURE 4.14: The interference amplitude vs the detuning of the 420 nm control laser in MHz for the double Λ-type system in (a) Fig. 4.1c, and (b) Fig. 4.1d which involves the excited states with different decay rates ($\Gamma_2 = 2\pi\times$ 6 MHz and $\Gamma_4 = 2\pi\times$ 1.4 MHz) at 780 nm and 420 nm transitions. Plots are shown for three different powers of the 420 nm control laser: 2, 4 and 8 mW.

shown in the set-up given in Fig. 4.2b and measuring the amplitude of the interference signal obtained at every frequency detuning.

We also study the frequency response of the two systems given in Fig. 4.1c and Fig. 4.1d in the presence of a magnetic field. The plot of the interference amplitude with the change in magnetic field is shown in Fig. 4.15a and Fig. 4.15b at various control frequency detunings. From these plots we find that whenever the two-photon resonance condition is satisfied, the interference amplitude is maximized. Next, we plot the interference amplitude with the detuning of the 420 nm control laser, Δ_{14} but in the presence of a magnetic field and is shown in Fig. 4.16a and Fig. 4.16b. The plot is obtained by

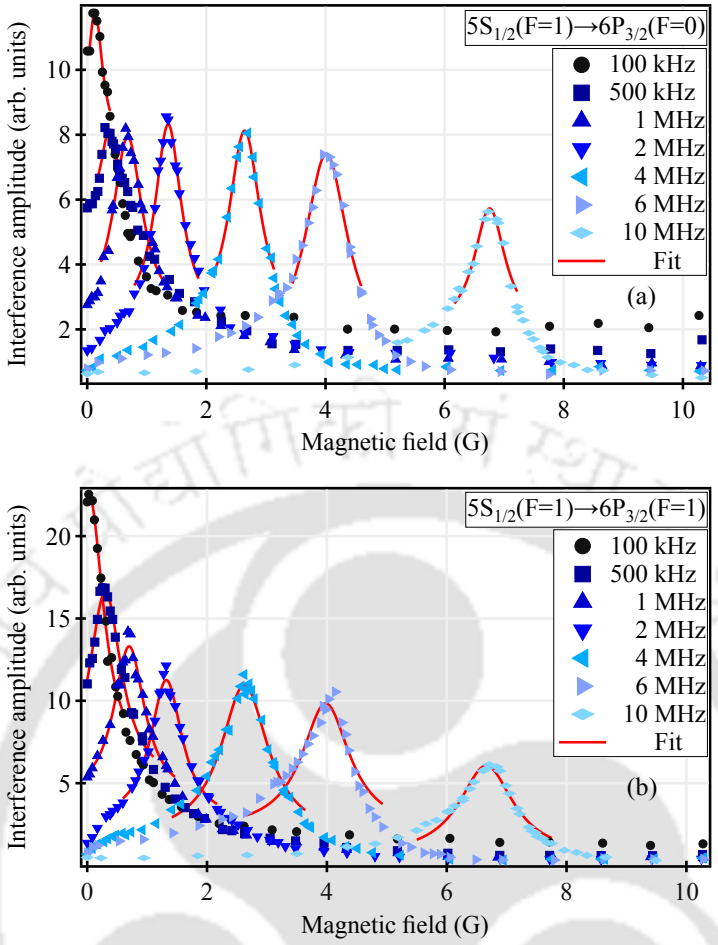

FIGURE 4.15: The interference amplitude vs the magnetic field in Gauss at various detuning of the control laser frequency, Δ_{14} =0.1, 0.5, 1, 2, 4, 6 and 10 ($2\pi\times$ MHz) for the double Λ-type system in (a) Fig. 4.1c, and (b) Fig. 4.1d which involves the excited states with different decay rates ($\Gamma_2 = 2\pi\times$ 6 MHz and $\Gamma_4 = 2\pi\times$ 1.4 MHz) at 780 nm and 420 nm transitions

measuring the interference amplitude at every control laser detuning after it has been optimize using the magnetic field such that it is maximum.

Further, we plot the amplitude of probe absorption with the detuning of the 420 nm control laser, Δ_{14} in absence and in presence of a magnetic field at optimum power and is shown in Fig. 4.17a and Fig. 4.17b. The plot shows that the frequency response is improved in the presence of the magnetic field. Fig. 4.18 shows a comparison of the amplitude of probe absorption vs the detuning of the control laser, Δ_{14} in presence and in absence of the magnetic field for the two different configuration of the closed loop double Λ-type system given in Fig. 4.1b and Fig. 4.1c. The plot shows that the behaviour in terms of the frequency response of the two systems is similar.

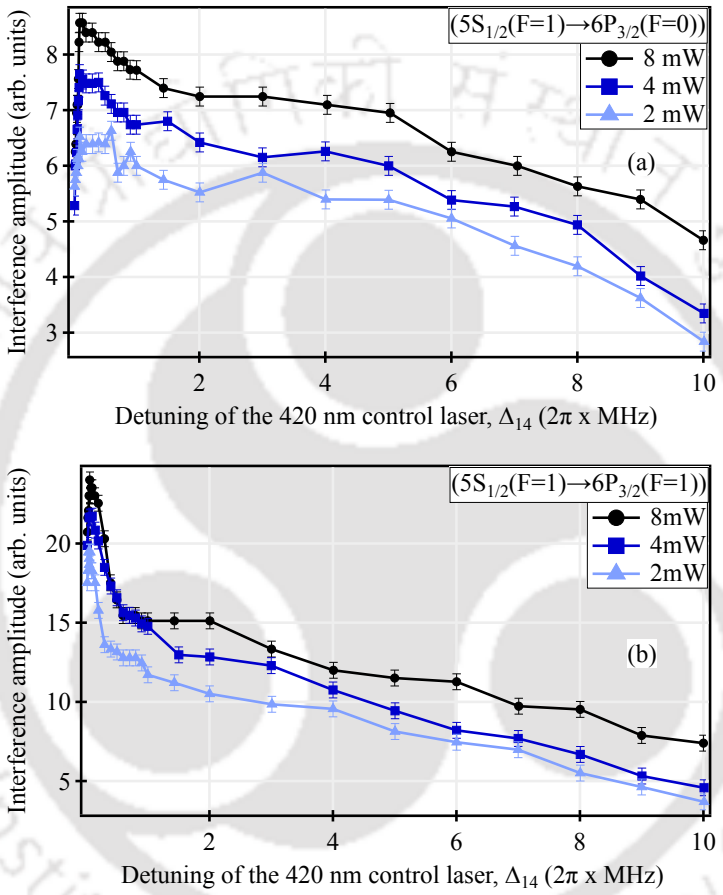

FIGURE 4.16: The interference amplitude vs the detuning of the 420 nm control laser, Δ_{14} in the presence of magnetic field for the double Λ-type system in (a) Fig. 4.1c, and (b) Fig. 4.1d which involves the excited states with different decay rates ($\Gamma_2 = 2\pi\times$ 6 MHz and $\Gamma_4 = 2\pi\times$ 1.4 MHz) at 780 nm and 420 nm transitions. Plots are shown for three different powers of the 420 nm control laser: 2, 4 and 8 mW.

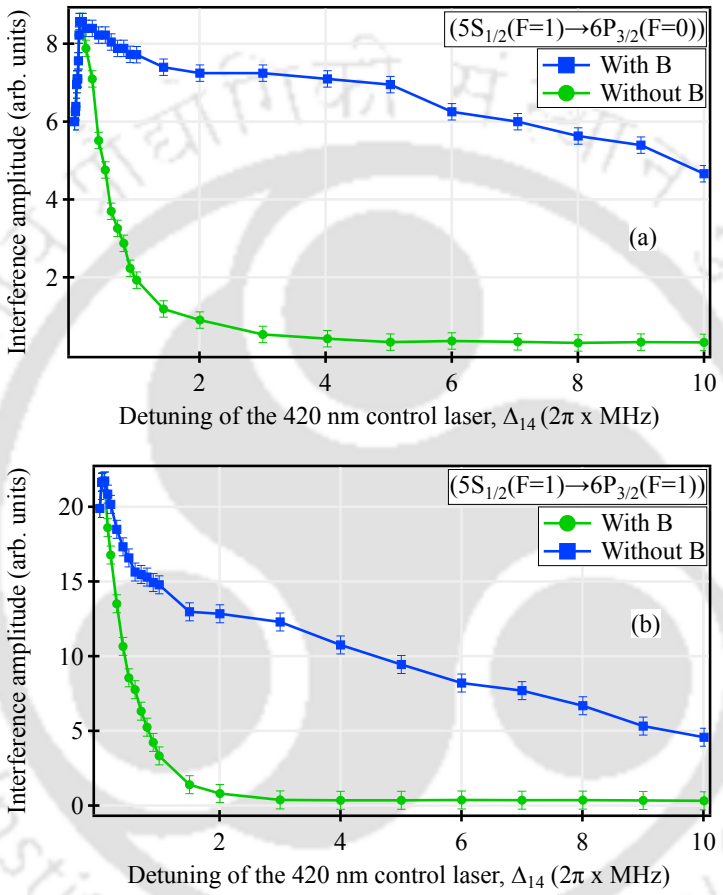

FIGURE 4.17: The interference amplitude vs the detuning of the 420 nm control laser, Δ_{14} in absence and in presence of the magnetic field for the double Λ-type system in (a) Fig. 4.1c, and (b) Fig. 4.1d which involves the excited states with different decay rates ($\Gamma_2 = 2\pi\times$ 6 MHz and $\Gamma_4 = 2\pi\times$ 1.4 MHz) at 780 nm and 420 nm transitions. The power of the probe and control lasers are kept at 0.02 and 8 mW respectively.

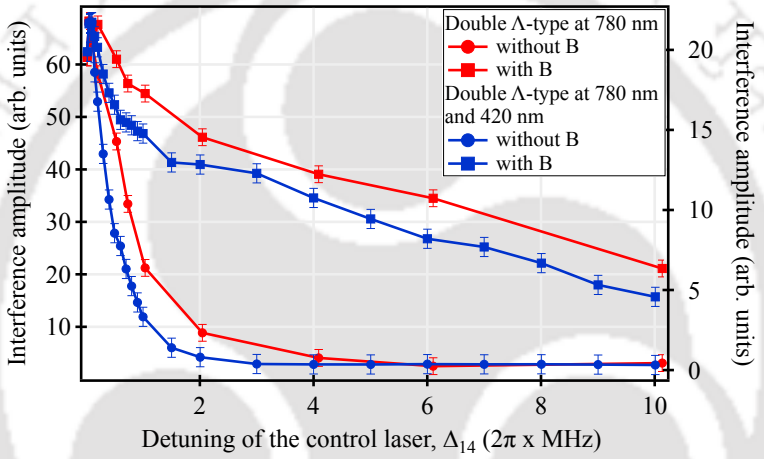

FIGURE 4.18: The interference amplitude vs the detuning of the control laser, Δ_{14} in presence and in absence of the magnetic field for the two different configuration of the closed loop double Λ-type system given in Fig. 4.1b and Fig. 4.1c. The plot in red involves the excited states with same decay rates ($\Gamma_2 = \Gamma_4 = 2\pi\times$ 6 MHz) at the 780 nm transition and the plot in blue involves the excited states with different decay rates ($\Gamma_2 = 2\pi\times$ 6 MHz and $\Gamma_4 = 2\pi\times$ 1.4 MHz) at the 780 nm and 420 nm transitions.

4.5 Conclusions

In conclusion we have demonstrated the atomic coherence based multi lasers interferometry in two different configurations of the closed loop double Λ-type system which is based upon the principle of phase-dependent EIT. These configurations involve the excited states with same decay rates at the 780 nm transition and with different decay rates at the 780 nm and 420 nm transitions respectively. We observed a similar behaviour in terms of the frequency response of the two different systems.

This chapter is to submitted as:

Atomic coherence based multi lasers interferometry

Dangka Shylla, Rajnandan Choudhury Das and Kanhaiya Pandey

Chapter 5

Characterization of ^{85}Rb atoms in the MOT

This chapter outlines the characterization of the cold Rb atoms in the magneto-optical trap (MOT). We know that cold atoms reduce the decoherence brought on by transit time broadening, the Doppler effect, collisions, etc., so it will be helpful for our interferometric experiments. We compared the sensitivity of the phase of atoms at room temperature and cold atoms in chapter 3, and it is evident that cold atoms perform better in the sensitivity measurements. In light of this, we set up the cold atom experiments and performed the cold atom characterization for ^{85}Rb atoms in the MOT using the $5S_{1/2}(F = 3) \rightarrow 5P_{3/2}(F = 4)$ broad cyclic IR transition at 780 nm. We studied the behaviour of the cold ^{85}Rb atoms in the MOT with various parameters such as hold time, power of cooling beam as well as the repumping beam. We also measured the optical density, the number of atoms and the temperature using absorption imaging. The temperature of the atoms in the MOT is around 500 μK as the result of Doppler cooling and the number of atoms trapped is around 1.5×10^8.

5.1 Introduction

One of the most basic laser cooling techniques [79, 109] used to obtain a cold gas cloud of atoms is the Doppler cooling method, which has a cooling limit [110, 111]

$$T_{\mathrm{D}}^{\mathrm{min}} = \frac{\hbar\Gamma}{2k_{\mathrm{B}}} \tag{5.1}$$

where, Γ is the natural linewidth of the atomic transition, $\hbar$ is the reduced Planck's constant and k_B is the Boltzmann's constant. However, the expression in Eq. 5.1 is valid in cases where the energy width of the excited state $\hbar\Gamma$ exceeds the recoil energy E_{r}

$$\hbar\Gamma \gg E_{\mathrm{r}} = \frac{\hbar^2 k^2}{2m} \tag{5.2}$$

where, m is the mass of the atom and k is the wave vector of the transition. In order to reach sub-Doppler temperatures, other cooling methods such as Sisyphus cooling [82, 83], grey molasses [84, 85] and evaporative cooling [86] methods are used. By laser cooling we can lower the temperature of the atoms, but a trapping mechanism is needed to keep the atoms confined. The configuration that can cool as well as trap the atoms is known as a magneto-optical trap (MOT) [112]. The cold gas cloud of atoms in the MOT serves as the foundation for many experimental studies on high precision spectroscopy [66], atom interferometry [67, 68], Bose-Einstein condensation (BEC) [69], atomic clocks [70], etc., as the ensemble of such atoms effectively reduces the collisional dephasing rate in the medium and also eliminates the Doppler effect in the spectral feature.

In this chapter, we discuss the design of a MOT for laser cooling and trapping of Rb atoms. The cold atom characterization was done for ^{85}Rb at $5S_{1/2}(F = 3) \rightarrow 5P_{3/2}(F = 4)$ broad cyclic IR transition using absorption imaging. To analyse the images and extract information about the cloud, such as its radius, optical density, number of atoms in the trap, and temperature, an image analysis programme was built. We report on the number of atoms we were able to trap as well the temperature of the cold atom cloud achieved with our set-up. These atoms can be further cooled by using sub-Doppler cooling mechanism such as polarization gradient cooling or narrow linewidth cooling at

420 nm open transition. In polarization gradient cooling, the cooling beams are left on and the magnetic field is switched off so the temperature reduces but the density of the cloud also reduces as a result of the cloud expansion. In narrow linewidth cooling, the IR MOT is simply transferred to the 420 nm MOT where the linewidth is four times lower than the IR transition. As a result, by the Doppler limit the temperature is lowered by four times while also winning at high phase-space density for quantum degeneracy which can benefit applications for a wide range of many-body physics phenomena [113] as well as quantum information processing [114–116]. We prepare such cold atoms for loading into a second stage narrow linewidth cooling at 420 nm open transition where we will experimentally realize the lower temperature it can offer [117].

This chapter is organized as follows: In section 5.2, we describe the energy level scheme and the experimental set-up which includes the polarization spectroscopy set-up, the MOT set-up that comprises the vacuum part as well as the magnetic field generation and the imaging set-up for the laser cooling and trapping of ^{85}Rb atoms in the MOT. In section 5.3, we present the experimental results obtained with our set-up. Finally in section 5.4, we give the conclusion on this work.

5.2 The energy level scheme and experimental set-up

The energy level scheme for the laser cooling and trapping of ^{85}Rb atoms with hyperfine splitting in MHz of the ground state $5S_{1/2}$ and excited state $5P_{3/2}$ [118] is given in Fig. 5.1. The lifetime of the $5P_{3/2}$ state is $\tau_1 = 26.25$ ns [96, 119]. In order to achieve the laser cooling and trapping of ^{85}Rb atoms, the 780 nm cooling laser is red detuned (in our case by 15 MHz) from the $5S_{1/2}(F = 3) \rightarrow 5P_{3/2}(F = 4)$ cooling transition. This is a closed transition so an atom excited to the $5P_{3/2}(F = 4)$ state will spontaneously decay back to the $5S_{1/2}(F = 3)$ ground state. However, despite the significant frequency mismatch it is also possible for an off-resonant excitation of another transition to the $5P_{3/2}(F = 3)$ state to occur. In this case the atom can then decay to the $5S_{1/2}(F = 2)$ lower ground state or $5S_{1/2}(F = 3)$ upper ground state. If an atom decays to the $5S_{1/2}(F = 2)$ lower ground state then it will become inaccessible to the cooling laser. The repumping laser that is

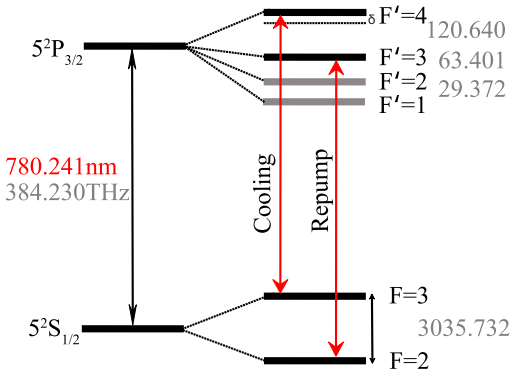

FIGURE 5.1: The energy level scheme for the characterization of ^{85}Rb atoms in the MOT using 780 nm laser with hyperfine splitting in MHz.

resonant with the $5S_{1/2}(F = 2) \rightarrow 5P_{3/2}(F = 3)$ transition is then used to bring back the atoms into the cooling cycle. This ensures the continuous operation of the MOT.

The experimental set-up for the laser cooling and trapping of ^{85}Rb atoms at $5S_{1/2}(F = 3) \rightarrow 5P_{3/2}(F = 4)$ cooling transition is shown in Fig. 5.3. The IR lasers are generated from the laser diodes (Thorlab L785H1) which are home-assembled extended cavity diode lasers (ECDLs) with a typical linewidth of 500 kHz [107] and beam diameter of 2 mm × 3 mm. In order to prevent the optical back reflections into the laser cavity, each laser is shielded with a single stage 40 dB optical isolator (Isowave I-80-T4-H). The IR lasers DL1 and DL2 operates in the master-slave configuration [120, 121] as shown in Fig. 5.3. The master laser is designated as DL1, while the slave laser as DL2. A portion of the beam from the master laser is frequency shifted by around +2×100 MHz using an acousto-optic modulator (AOM) in the double-pass configuration [122] and is then injected into the slave laser as shown in the Fig. 5.3. The double-pass configuration has the advantage of preserving the optical alignment of the injection beam when the frequency of the AOM is changed. The frequency of the master laser is stabilized by an electronic feedback circuit with the method of polarization spectroscopy [123]. The frequency of the slave laser gets locked to the frequency of the injection beam. By varying the frequency of the AOM, the frequency of the slave laser can be changed precisely and rapidly. With this configuration, the frequency of the cooling laser is always precise within sub-MHz precision and provides a tuning range up to 26 MHz. The slave laser output of 70 mW is used as the cooling beam for the MOT experiments after it has been frequency shifted

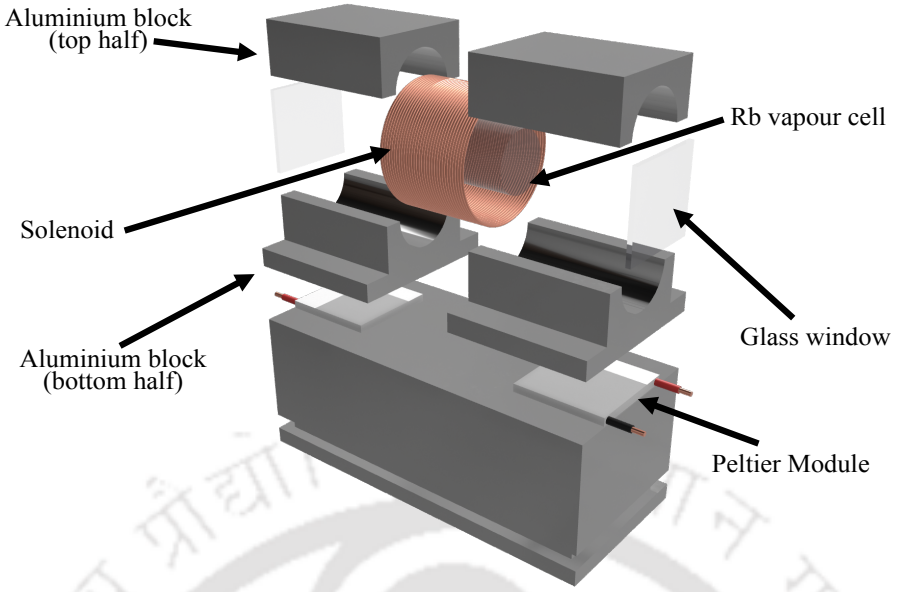

FIGURE 5.2: Illustration of the Rubidium cell oven.

by +114 MHz using another AOM in the single-pass configuration such that it is red detuned on the $5S_{1/2}(F = 3) \rightarrow 5P_{3/2}(F = 4)$ cooling transition. This AOM is used for fast switching and power variation of the 780 nm cooling beam. The DL3 with laser output of 25 mW is used as the repumping laser. Both the cooling and repumping beams are combined to co-propagate and is then sent to the MOT set-up. The experimental set-up is further divided into three main sections: the spectroscopy set-up, the MOT set-up and the imaging set-up.

5.2.1 The spectroscopy set-up

In order to improve the signal-to-noise ratio of the absorption spectra for the spectroscopy, an oven for heating the Rb vapour cell is designed and is shown in Fig. 5.2. The Rb vapour cell is heated to around 50°C using two Peltier modules. These two Peltier modules are placed close to the windows to prevent coating which develops as a result of uneven heating of the Rb vapour cell and can obstruct beam transmission, resulting in weak spectra signals and consequently low signal-to-noise ratio. The signal-to-noise ratio significantly increases with this arrangement given in Fig. 5.2. The spectroscopy set-up for error signal generation and laser stabilization of the 780 nm cooling and repumping laser to the desired transition is done using polarization spectroscopy [124–126] where

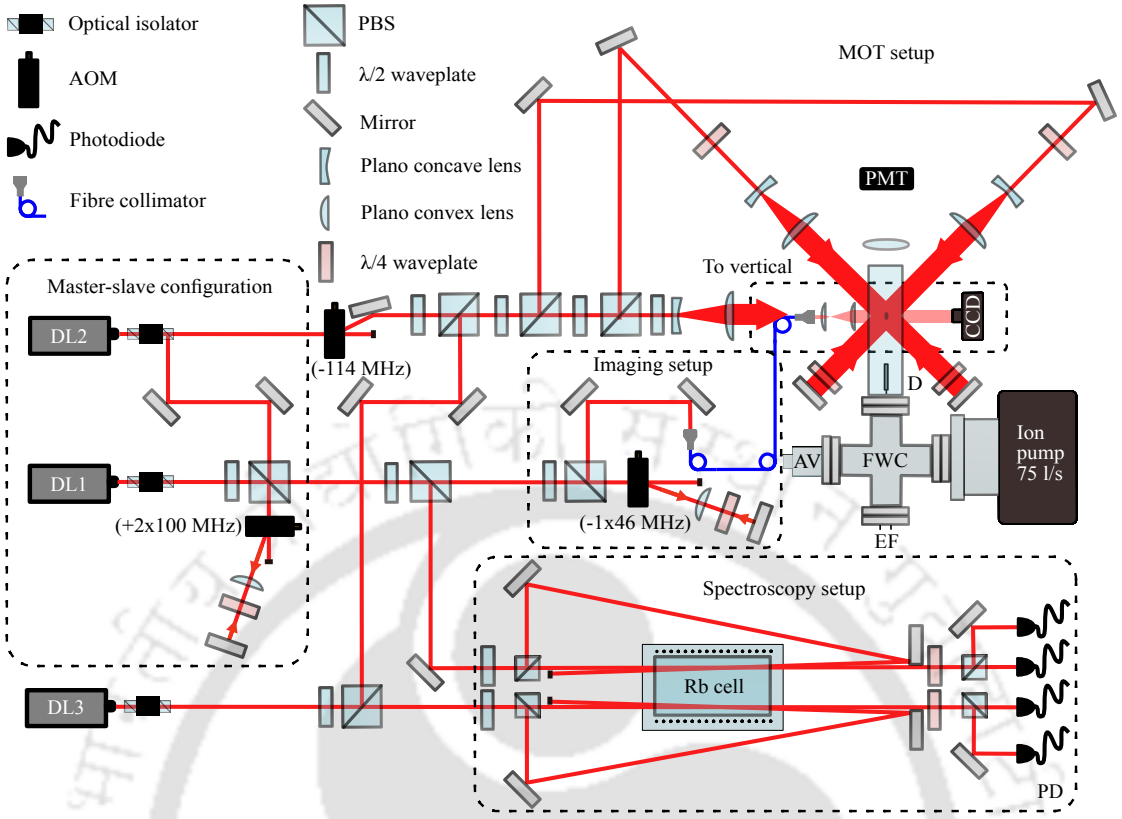

FIGURE 5.3: A schematic diagram of the experimental set-up displaying how the optical table is arranged. The Master-slave configuration, spectroscopy set-up, imaging set-up and the MOT set-up are shown in blocks marked with a dashed line. DL: diode laser; AOM: acousto-optic modulator; PD: photodetector; PMT: photomultiplier tube; CCD: charge-coupled device; FWC: four-way cross; AV: angle valve; EF: electrical feedthrough.

the magnetic field is applied in the direction of propagation of the probe beam and is labelled as spectroscopy set-up in Fig. 5.3. The advantage of this method is that it does not affect the frequency of the laser beam going to the experiment. The typical error signal generated by polarization spectroscopy is shown in Fig. 5.4a and 5.4b.

The master laser is divided into three main parts. The first part is used for injection locking as described above. The second part is sent to the Rb vapour cell inside the oven for the frequency stabilization to the $F = (2, 4)$ crossover peak of the ^{85}Rb absorption spectrum as shown in Fig. 5.4a. The power of the control and probe beams used are around 1 mW and 160 μW, respectively. The third part is sent to the imaging set-up where it will be covered in section 5.2.3.

The 780 nm repumping laser is divided into two parts. The first part is sent to the

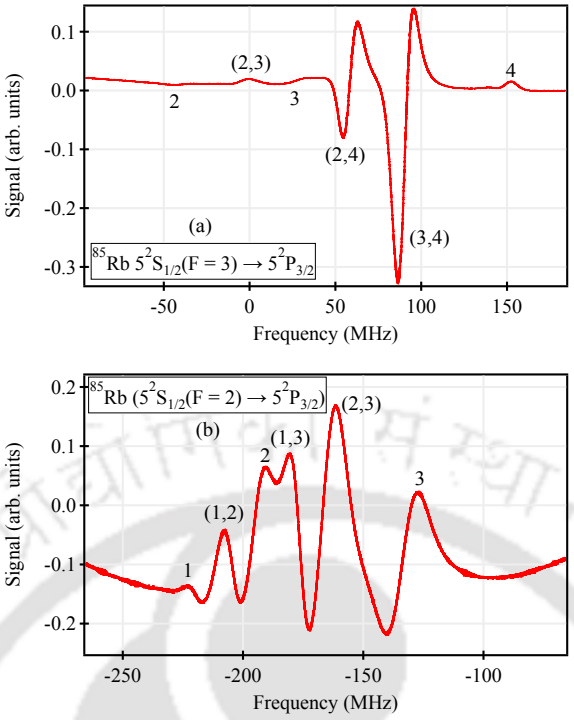

FIGURE 5.4: (a) Error signal vs frequency scan in MHz of ^{85}Rb $5S_{1/2}(F = 3) \rightarrow 5P_{3/2}(F = 4)$ and (b) Error signal vs frequency scan in MHz of ^{85}Rb $5S_{1/2}(F = 2) \rightarrow 5P_{3/2}(F = 3)$ using the polarization spectroscopy method. The numbers represent the various hyperfine levels and the numbers in the brackets are the crossover resonances.

same vapor cell inside the oven for the frequency stabilization. The repumping laser is frequency stabilized on the $5S_{1/2}(F = 2) \rightarrow 5P_{3/2}(F = 3)$ transition of the ^{85}Rb absorption spectrom as shown in Fig. 5.4b using the same polarization spectroscopy [126]. The power of the control and probe beams are 150 μW and 128 μW, respectively. The spatial separation between the cooling and repumping probe beams is around 1 cm. The second part is then sent to the MOT set-up.

5.2.2 The MOT set-up

The MOT set-up consists of a vacuum system, an atomic source of Rb, magnetic field coils and three sets of beams as shown in the Fig. 5.5.

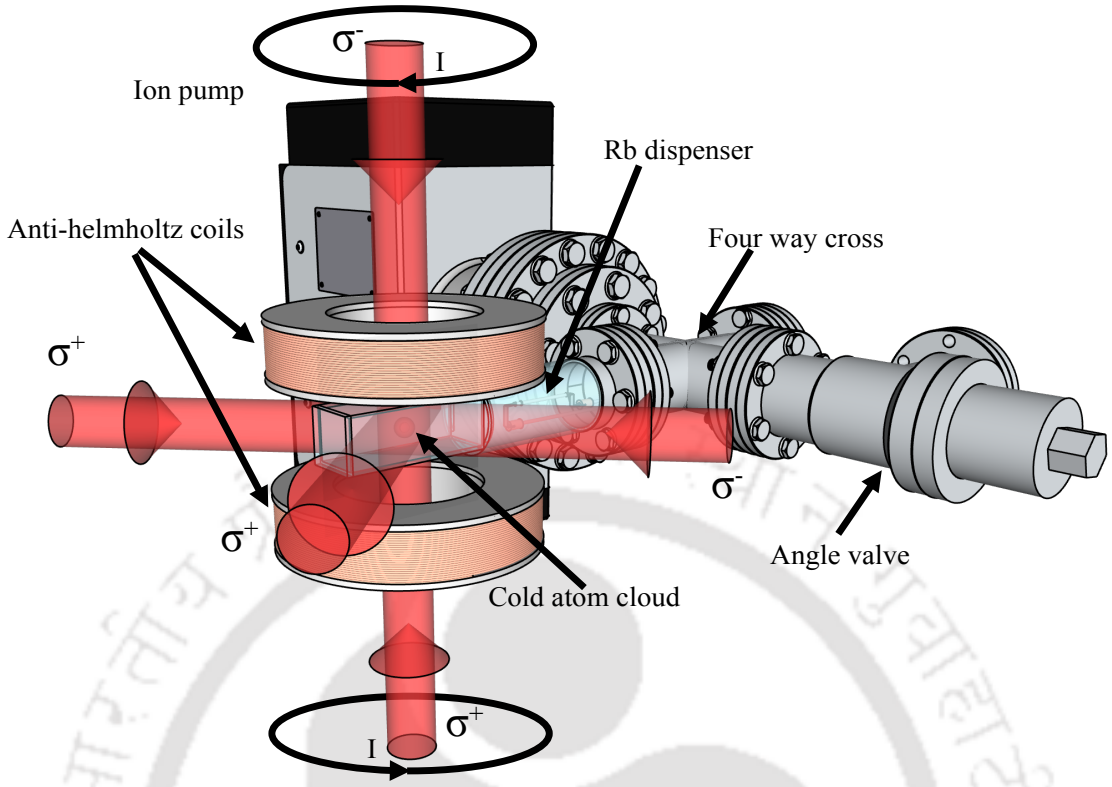

FIGURE 5.5: The 3D-MOT set-up displaying the vacuum chamber of the experiment, the three pairs of the circularly polarized cooling laser beams counter-propagating along three coordinate axes and current I flowing in opposite directions of the AH coils.

Vacuum system

In order to reach the required vacuum conditions for our MOT experiments, three pumps have been employed in the following order: rotary pump, turbo-molecular pump, and ion pump. Each one of them operates within a specific range of pressure. The rotary pump has a pressure range from 1 bar to 1.9×10^{-3} mbar, the turbo-molecular pump from 0.5×10^{-2} to 10^{-7} mbar and ion pump from 10^{-6} to 10^{-11} mbar. The rotary pump is connected to the turbo-molecular pump through a flexible corrugated metal hose using rubber O-rings and Klein Flange (KF) flanges. The turbo pump is then connected to a four-way cross and a pressure gauge is attached above it to monitor the pressure inside. One end of the four-way cross is then attached to the manually operated all-metal angle valve through another flexible corrugated metal hose. The angle valve is connected to one of the flanges of another four-way cross. On the flange opposite to the valve, there is an inlet and a branch in which the ion pump with pumping speed of 75 l/s is connected.

A separate ion-gauge gives a measure of the vacuum pressure inside, which should be in the range of 10^{-10} mbar. The vacuum system at this point are sealed by copper O-rings and ConFlat (CF) flanges. At the other two flanges, we have the MOT cell of dimension 100 mm x 25 mm x 25 mm and the Rb source that is attached to the electric feedthrough as shown in the Fig. 5.3.

The Rb source used here is a Rb dispenser (AlfaSource AS-Rb-0090-2C) which is a controllable source of Rb vapour has 90 mgs of Rb compound. The Rb compound is contained in a small stainless steel cylindrical casing. This source is affixed onto two pins of vacuum electric feedthrough system attached to one end of the four-way cross as shown in Fig. 5.5. When current is applied, Rb vapour is produced and flows in the MOT cell. The dispenser can emit Rb atoms only if the threshold current is exceeded. The more current applied to the dispenser the more Rb vapour is produced. The current is adjusted to the operating current preferably at low operating current of the dispenser which is 2.1 A in our case. The Rb dispenser is positioned as close to the MOT cell as shown in Fig. 5.5 but there must not be a direct line of sight between it and the ion pump.

Continuous baking of the chamber for one week at a temperature of around 200^oC has been done in order to remove as many molecules as possible through the process of degassing. Once the necessary pressure has been reached which is around 10^{-10} mbar in our case, the rotary and turbo-molecular pumps are removed from the ion pump. The angle valve is then used to isolate the vacuum system from the turbo-molecular pump using a hermetic seal and the ion pump is constantly kept on.

Magnetic field generation

A MOT requires a well designed Anti-Helmholtz coil [127, 128]. We have used an Anti-Helmholtz coil which can generate 18 G/cm magnetic field gradient by passing current, I= 1 A. Each coil has an inner diameter of 7 cm, outer diameter of 13 cm, thickness of 3 cm, and 500 number of turns. The wire diameter of 1 mm is also taken into consideration because there is a limit to how much current a wire can withstand before being damaged. The design of the Anti-Helmholtz coil pair is such that it does not obstruct our three pairs

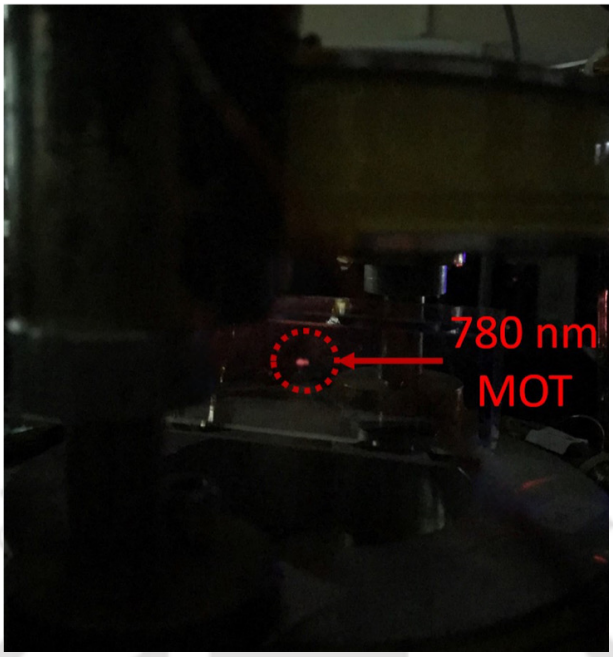

FIGURE 5.6: Photo of the cold atomic cloud in the MOT at780 nm as seen with the naked eye.

of laser beams. To eliminate the stray magnetic field, three pairs of shim coils are also utilized around the MOT chamber (although these are not included in the schematics). For fast switching "on" and "off" of the magnetic field, a high current switch based on an insulated-gate bipolar transistor (IGBT) is used. The switching-off time of the coil is around 20 μs.

In the MOT set-up the cooling and repumping beams after combining and co-propagating are further divided into three pairs. The three pairs of beams are expanded with Galilean telescopes consisting of a pair of plano-concave and plano-convex lens of focal length -25 mm and 250 mm respectively to a diameter of around 25 mm. The expanded beams are then made mutually perpendicular and properly circularized using a $\lambda/4$ wave-plate and retro reflected back with a combination of a mirror and a $\lambda/4$ wave-plate intersecting at the center of the MOT chamber. The laser cooled and trapped rubidium atomic cloud in the MOT at 780 nm observed that is visible to the naked eye and is as shown in Fig. 5.6.

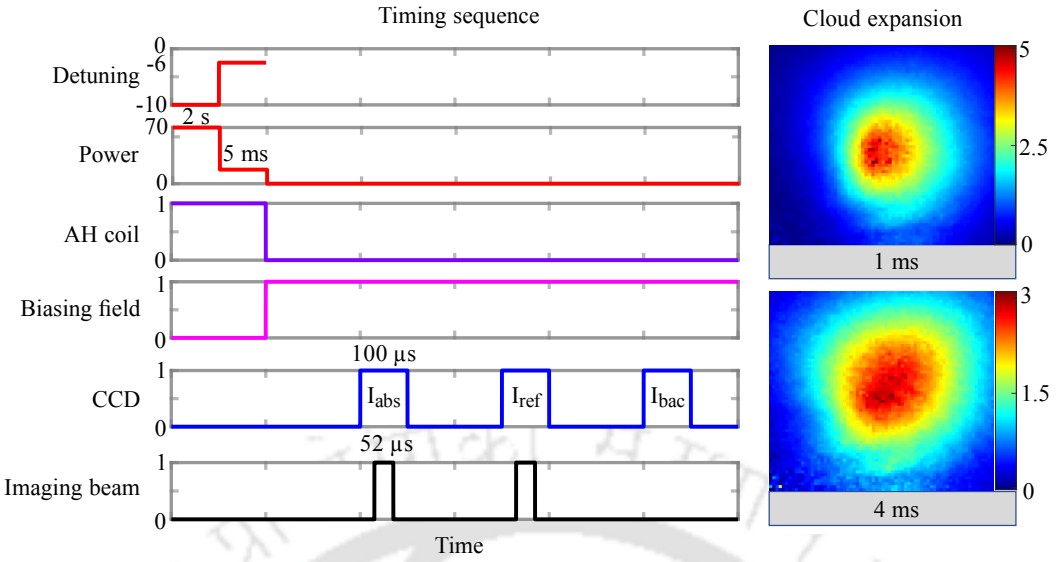

FIGURE 5.7: (a) Timing squence used to capture the images for the measurement of the optical density, radius, number of atoms in the trap as well as temperature, and (b) Cloud expansion at 1 ms and 4 ms TOF respectively.

5.2.3 Imaging set-up

The absorption imaging is done using a portion of beam from the master laser as shown in Fig. 5.3. It is upshifted by $+2\times46$ MHz using an AOM in double-pass configuration such that it is resonant on the $5S_{1/2}(F = 3) \rightarrow 5P_{3/2}(F = 4)$ cooling transition. This AOM is used mainly for fast switching and for tuning the frequency of the imaging beam around the resonance of the cooling transition. A double-pass configuration [122] is chosen as it prevents misalignment when the detuning of the imaging beam is changed. This beam is then sent to the polarizing maintaining fibre where its spatial modes are clean to a Gaussian. It is then expanded and collimated with a combination of lenses such that it is big enough to overlap with the whole atom cloud. It is also circularly polarized using a combination of $\lambda/4$ wave-plate and a polarizing beam splitter (PBS). A small biasing field if 1 G is generated from a pair of shim coils which is not shown in the schematics. The power of the imaging beam used before the expansion is around 6 μW. After the MOT the imaging beam is demagnified close to the size of the chip in the camera i.e. a demagnification of 0.1. The camera used is a CCD camera (Imprex B0620) with a chip of 640x480 pixels each of which has a size of 7.40 μm. The timing sequence used to capture the images for the measurement of the optical density, radius,

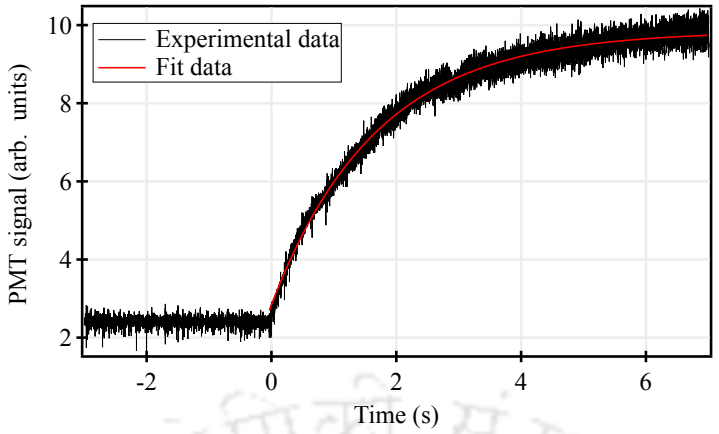

FIGURE 5.8: Loading of the MOT. The beams are turned on at t = 0, after which the signal shows an exponential growth with a time constant of about 1.7 s as obtained from the fit.

number of atoms in the trap as well as temperature using absorption imaging is as shown in Fig. 5.7a. Three images: the imaging beam with the atomic cloud, the imaging beam without the cloud and then the background are captured using the timing sequence to determine the optical density, radius of the cloud and the number of atoms. The same sequence is executed twice but with two different time of flights (TOF) at 1 ms and 4 ms to determine the temperature of atomic cloud and is shown in Fig. 5.7b.

5.3 Experimental results

We determined the loading time of the atom cloud by measuring the trap fluorescence with time by fast switching the beams from "off" to "on". The trapped fluorescence is related to the number of atoms. The plot of PMT signal with time is shown in Fig. 5.8. The loading time of the atom cloud is determined from the fit given by exponential growth equation

$$N = N_s(1 - e^{-\frac{t}{\tau}}) \tag{5.3}$$

where N_s is the number of atoms in the steady state and τ is the loading time. The loading time is found to be around 1.70 s as obtained from the fit (for time, t > 0). As a result, the loading time of the atomic cloud in the timing sequence for our experiments is fixed at 2 s.

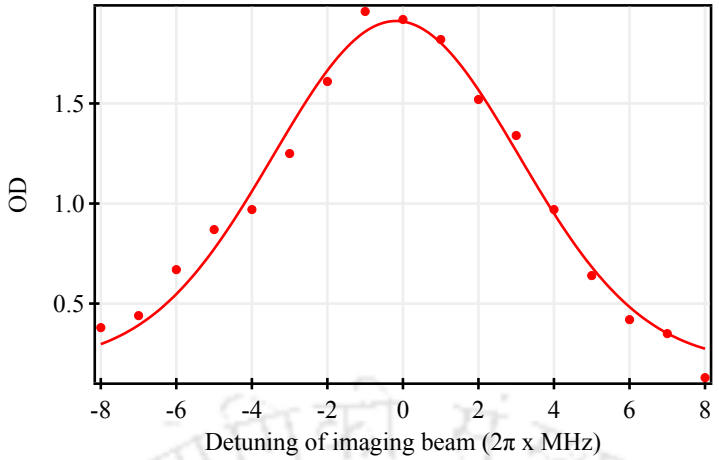

FIGURE 5.9: OD vs Imaging detuning in MHz. The line center is at the resonance indicating that there is no lock-offset and the linewidth is around $2\pi\times9$ MHz as obtained from the Lorentzian fit

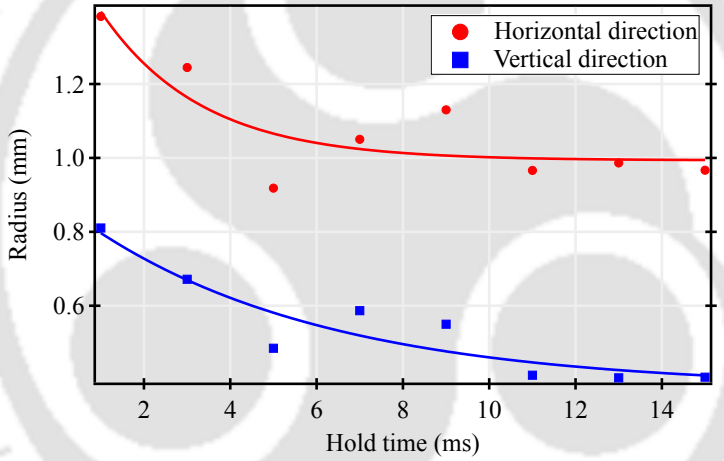

FIGURE 5.10: Characterization of ^{85}Rb atoms in the MOT. Radius of the atomic cloud vs the hold time in ms at low power of the cooling laser in the MOT for horizontal and vertical direction. The solid lines are exponential fits with 1/e decay time of 2.33 ms and 5.52 ms for horizontal and vertical direction respectively.

Using the loading time of 2 s, we measured the optical density (OD) at different detuning of the imaging beam in MHz. The OD is determined from three recorded images in the following sequence: the imaging beam with the atom cloud, the imaging beam without the cloud and then the background. Thus, the OD can then be calculated as:

$$OD = -\ln\left(\frac{I_{\text{abs}} - I_{\text{bac}}}{I_{\text{ref}} - I_{\text{bac}}}\right) \tag{5.4}$$

where I_{abs} is the image of the imaging beam with the atom cloud, I_{ref} is the image of the

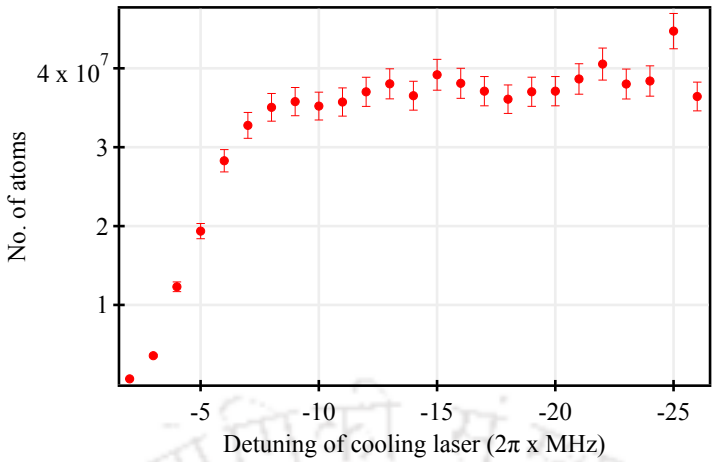

FIGURE 5.11: Characterization of ^{85}Rb atoms in the MOT. Number of atoms vs Frequency detuning of cooling laser in MHz keeping the power of cooling and repumping laser at maximum i.e., at 70 mW and 20mW respectively. The detuning of the cooling laser at 780 nm is kept at -6 MHz during the hold time.

imaging beam without the atom cloud and I_{bac} is the image of the background. To find the OD the fraction of $-\ln\left(\frac{I_{\text{abs}}-I_{\text{bac}}}{I_{\text{ref}}-I_{\text{bac}}}\right)$ for every pixel is calculated at every detuning of the imaging beam, thus creating a matrix for the optical density for every pixel of the CCD chip. Using a 2D gaussian fit we extract the OD and the radii of the cloud along horizontal and vertical direction. The plot of OD with various imaging detuning in MHz is as shown in Fig. 5.9 and linewidth is found to be 8 MHz as obtained from the Lorentzian fit. It also shows that there is no lock offset as the OD is maximum at the resonant frequency of the cooling transition at $5S_{1/2}(F=3) \rightarrow 5P_{3/2}(F=4)$.

We then vary the hold time and lower the power of the cooling laser by factor of 10 keeping the detuning of the cooling laser at -6 MHz. Fig. 5.10 shows the radius of the atomic cloud with the hold time decreasing exponentially with increase in the hold time, indicating the cooling of the cloud. The radii data are fitted to an exponential decay function with 1/e decay time of 2.33 ms and 5.52 ms for horizontal and vertical direction respectively. The plot also shows that the radius of the cloud does not vary in size after a 5 ms hold time. For this reason, the cooling laser power is lowered to 7 mW for 5 ms throughout our experiments.

Next, the number of atoms in the atom cloud is measured by varying various parameters like the detuning of the cooling beam and power of the cooling beam as well as the

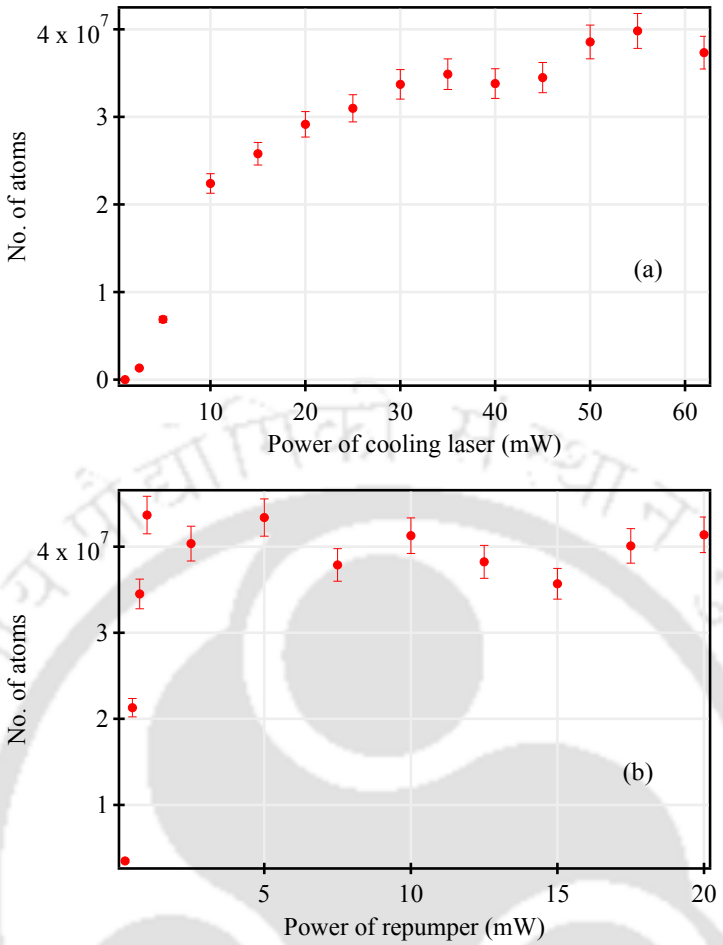

FIGURE 5.12: Characterization of ^{85}Rb atoms in the MOT. (a)Number of atoms vs Power of cooling laser in mW keeping power of repumper at maximum i.e., at 20 mW and (b) Number of atoms vs Power of repumper in mW keeping power of cooling laser at maximum i.e., at 70 mW. The detuning of the cooling laser at 780 nm is kept at -15 MHz during the loading time and -6 MHz during the hold time for both cases.

repumping beam. To find the number of atoms, we first determine the number density using optical density and radii obtained above. The number density n_0 of atoms is given by

$$n_0 = \frac{OD}{\sqrt{2\pi} S_0 \sigma_{\min}} \tag{5.5}$$

where $S_0 = 3\lambda^2/2\pi$ is the saturation parameter and the total number of atoms can be obtain by using Eq. 5.5 in

$$N_0 = (2\pi)^{3/2} n_0 \sigma_x \sigma_y \sigma_{\min} \tag{5.6}$$

σ_x and σ_y are the radii along the horizontal and vertical direction. $\sigma_{\min}$ is taken to be the minimum of σ_x or σ_y.

The number of atoms is first monitored by varying the detuning of the cooling laser during the loading time and keeping it fixed to -6 MHz during the hold time. We obtained a plot for number of atoms with the frequency detuning of the cooling laser in MHz and is shown in Fig.5.11a. From the plot, it shows that the number of atoms increases with the increase in the detuning of the cooling laser and then begins to saturate at higher detuning. At -15 MHz detuning of the cooling beam, maximum number of atoms (4×10^7) are trapped. This detuning is hence used for loading throughout our experiments.

In order to study the effect of power of cooling laser on the number of atoms, the detuning of the cooling beam is kept at -15 MHz during the loading time, -6 MHz during the hold time and power of the repumper is kept at maximum. We obtained a plot for the number of atoms with change in power of the cooling laser in mW and is shown in Fig 5.12 a where the number of atoms starts to increases with increase in power of the cooling laser and then saturates at high power. It indicates that 70 mW power of the cooling laser is sufficient for the loading of the cold atoms and is used throughout the experiments.

We also studied the effect of the power of the repumping laser on the number of atoms and the plot is given in Fig.5.12b. The power of the cooling laser is kept at maximum and its detuning is kept at -15 MHz during the loading time and -6 MHz during the hold time. We observe a similar behaviour with the cooling laser power. The number of atoms first increases with increase in repumping power and then saturates to a maximum at high power. It shows that 25 mW of repumper power is sufficient to capture 4×10^7 atoms.

Lastly, we measured the number of atoms and temperature in μK of the atom cloud with various detuning of the cooling laser during the hold time but keeping the detuning fixed at -15 MHz during the loading time. From the plot shown in Fig.5.13a it shows that the number of atoms increases with the increase in the detuning of the cooling laser and then begins to saturate at higher detuning. At around -15 MHz detuning of the cooling beam, maximum number of atoms 1.5×10^8 are trapped. For the temperature measurements as discussed above, the atomic cloud temperature is measured by comparing its radius at two distinct TOF where the magnetic field has been turned "off". This is done by repeating the same time sequence in Fig. 5.7 again, but using TOF 1 ms and 4 ms. The

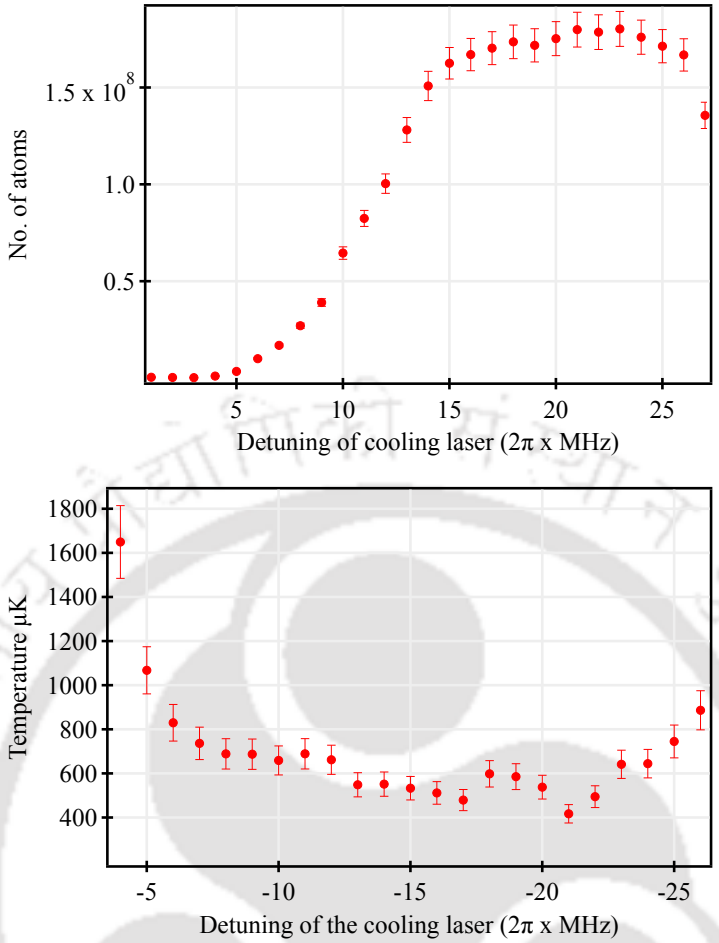

FIGURE 5.13: Characterization of ^{85}Rb atoms in the MOT. (a) Number of atoms vs Cooling laser frequency detuning in MHz. (b) Temperature in μK vs Cooling laser frequency detuning in MHz keeping cooling and repumping laser power at maximum i.e., at 60 and 20 mW respectively. The detuning of the cooling laser at 780 nm is kept at -15 MHz in the loading phase and -is varied from 0 to -27 MHz in the optimization phase for both the cases.

radius of the cloud is expressed as a function of time t by [129]

$$\sigma_z^2 = \sigma_{z0}^2 + \left(\frac{k_B T}{M_{Rb}}\right) t^2 \tag{5.7}$$

The temperature is then determined from Eq. 5.7 and is given by

$$T = \frac{M_{Rb}}{k_B}\left(\frac{\sigma_{z2}^2 - \sigma_{z1}^2}{t_2^2 - t_1^2}\right) \tag{5.8}$$

where M_{Rb} is the mass of Rb, σ_{z1} and σ_{z2} are the radii of the cloud at t_1 and t_2 respectively. The plot of temperature with change in the detuning of the cooling laser is

shown in Fig.5.13b. From the plot, the temperature decreases rapidly as the deturning is shifted from the resonance and then it increases slowly as the detuning is further change from the point of minimum. We observe that at -15 MHz, the temperature of the atomic cloud is minimum and it is around 500(50) μK.

5.4 Conclusions

In conclusion we have demonstrated the laser cooling and trapping of ^{85}Rb atoms in the MOT using the broad cyclic IR transition, $5S_{1/2} \rightarrow 5P_{3/2}$ at 780 nm to trap around 1.5×10^{8} number of atoms at typical temperature of 500(50) μK. These cold atoms are prepared to be loaded into a second stage narrow linewidth cooling at a 420 nm open transition, where we finally realized the lower temperature it can offer due to the Doppler cooling limit. This will help create the high phase-space density atomic cloud necessary to achieve quantum degeneracy.

Chapter 6

Effect of detuning on velocity induced population oscillation

THIS chapter outlines an experimental study on the effect of detuning on velocity induced population oscillation (VIPO) for a Doppler mismatched double resonance. The double resonance experiment is conducted on $5S_{1/2} \rightarrow 5P_{3/2}$ transition (at 780 nm) and $5S_{1/2} \rightarrow 6P_{1/2}$ transition (at 421 nm) in ^{87}Rb at room temperature. The method measures the shift of the VIPO dip from the line center of the transparency or enhanced absorption (EA) peaks caused by the lock offset point of the resonantly driving laser i.e., the IR laser in our case. The shift in the VIPO dip with IR laser detuning is non-linear but symmetrical and the width of the line profile for the VIPO dip height with IR laser detuning is sub-natural. We subsequently utilized the effect to precisely determine the locking point of the IR laser on the $5S_{1/2}(F=2) \rightarrow 5P_{3/2}(F=3)$ transition in the double resonance configurations with an uncertainty of around 100 kHz. The experimental result is well supported by numerical simulation using the density matrix calculations.

6.1 Introduction

Velocity-induced population oscillation (VIPO) [71–73] is an important addition to the commonly used saturated absorption spectroscopy (SAS) [130, 131] and has been utilized for the removal of crossover peaks and broadening due to mismatch of the wavelength for probe and control lasers [75, 76]. The phenomenon of VIPO has been rigourously studied for the saturated fluorescence spectrum in two-level system, which is a very useful spectroscopic technique for weak transitions [74]. Recently, the VIPO effect has been utilized to eliminate the partial Doppler broadening and hence resolve the closely spaced hyperfine levels of the $6P_{3/2}$ state in Rb for Doppler mismatched double resonance [77].

In this work, we describe the effect of detuning on the VIPO dip which can be an effective method to determine the laser lock offset on a particular atomic transition. Laser lock offset is very important for the precision measurement of the optical transition. As the precision measurement of the atomic-optical frequency is used for the verifications of various atomic models [132, 133], accurate calculations of physical quantities such as Lamb shift [134], hyperfine structure constants [135], optical frequency reference [136], coherent excitation of the Rydberg states for quantum information processing [137], etc.

We demonstrate this effect i.e. the detuning on VIPO resonance in the V-type and in the optical pumping system in ^{87}Rb. A probe and a counter-propagating control laser beam of same polarization driving the $5S_{1/2}(F = 2) \rightarrow 5P_{3/2}(F = 3)$ transition starts interfering (or beating) which induces a temporal modulation of the population between the lower and upper levels of the transition [138–144]. A second pump laser scans across the $6P_{1/2}$ hyperfine levels on $5S_{1/2} \rightarrow 6P_{1/2}$ transition and redistributes the population. In this configuration, a VIPO dip appears in the transparency or EA spectrum window whose position is sensitive to the IR laser detuning. The shift in the VIPO dip vs IR detuning is non-linear but symmetrical. The width of the profile for the VIPO dip height vs IR laser detuning is sub-natural which helps us to precisely determine the lock offset of the IR laser. VIPO is very similar to the standing wave electromagnetically induced transparency (EIT). Note that, EIT in the standing wave probe-control configuration in a V-type system [77, 145, 146] as well as in the standing wave control-control configuration in the ladder system [147, 148] and lambda system [149] has been studied. However, the

effect of detuning has not been studied in detail and it has not been utilized in the theme of spectroscopy. In this work, we utilize these effects to determine the laser lock offset.

This chapter is organized as follows. In section 6.2, we describe the relevant energy levels for the different experimental configurations and the experimental set-up. In section 6.3, we describe the density matrix formalism for the various systems considered and the numerically simulated absorption profile of the probe. In section 6.4, we present the experimental results of the effect of detuning on the VIPO dip corresponding to $5S_{1/2}(F = 2) \rightarrow 5P_{3/2}(F = 3)$ transition in ^{87}Rb. Finally in section 6.5, we give the conclusion on this work.

6.2 The energy schemes and set-up

The relevant energy levels for the different experimental configurations are shown in Fig. 6.1. The propagation direction of the beams for the probe and control laser at 780 nm (IR) and the pump laser at 421 nm (blue) transitions are shown at the bottom of the level schemes. The IR laser is tuned near the resonance on the $5S_{1/2}(F = 2) \rightarrow 5P_{3/2}(F = 3)$ cycling transition. The lifetime of the $5P_{3/2}$ state is $\tau_1 = 26.23$ ns [96]. The absorption of the probe is monitored as the co-propagating blue pump laser scans across the $6P_{1/2}$ hyperfine levels on $5S_{1/2}(F = 2) \rightarrow 6P_{1/2}$ transition which corresponds to a V-type system (or $5S_{1/2}(F = 1) \rightarrow 6P_{1/2}$ transition which corresponds to the optical pumping system). The lifetime of the $6P_{1/2}$ state is $\tau_2 = 125.32$ ns [150]. The experimental set-up for the various configurations (in Fig. 6.1) is shown in Fig. 6.2. The IR laser is generated from a laser diode (Thorlab L785H1) which is a home-assembled extended cavity diode laser (ECDL) with a typical linewidth of 500 kHz. The beam diameter of the 780 nm beams are 2×3 mm. The power of the probe beam used in the experiment is 42 μW (or peak intensity of 1.78 mW/cm^2).

The blue laser is generated using a commercially available ECDL (Toptica DL PRO HP) with a typical linewidth of < 200 kHz and output power of 70 mW. A portion of the blue beam is fed to the Fabry-Perot Interferometer for monitoring the single-mode operation of the laser. The beam diameter of the 421 nm pump beams is 3×4 mm. The scan of

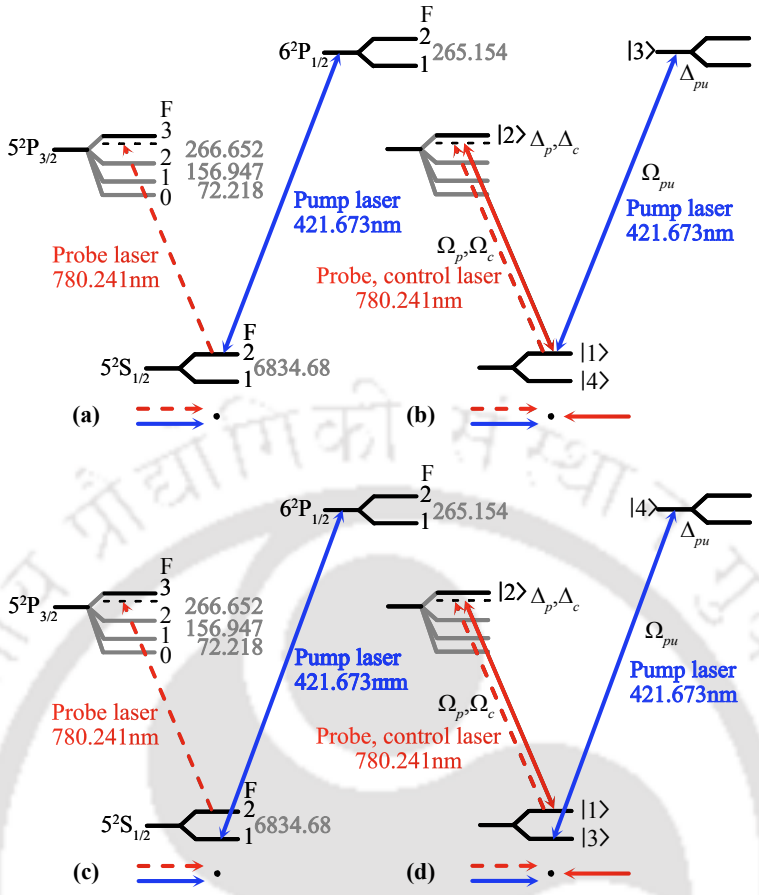

FIGURE 6.1: The energy level schemes (with hyperfine splitting in MHz) for (a) V-type system, (b) V-type system with VIPO effect at IR transition, (c) optical pumping system and (d) optical pumping system with VIPO effect at IR transition.

the blue pump laser is frequency calibrated using the peaks of the reference spectrum corresponding to the $6P_{1/2}$(F=1,2) hyperfine levels and the hyperfine interval is given in Ref. [151].

In order to study the effect of detuning of the IR lasers on the VIPO dip, the probe laser beam is divided into two beams with the same polarization and power. The two probes co-propagate in another Rb cell with a spatial separation of about 1 cm. The blue laser beam is also divided into two beams with identical polarization and co-propagates with the two probes (see the experimental set-up in Fig. 6.2 for details). One set of co-propagating probe and blue pump beam is used as a reference for frequency calibration of the scan of the blue pump laser. The IR control beam which counter-propagates with only one of the probe beam, has the same polarization as the probe beam. The same

polarization is crucial for the beating of the two fields addressing the same IR transition. The angle between the beams is kept as minimum as possible and in addition a magnetic shield is also used to minimize the broadening effects of the spectrum.

6.3 Theoretical model

6.3.1 The V-type system

The energy level configuration for the V-type system is shown in Fig. 6.1a. The absorption of the probe is reduced by blue pump laser due to multiple effects namely, population transfer by the blue pump laser in a V-type atomic system [152], the coherence effect causing EIT in a V-type atomic system [153, 154] and the optical pumping of population [155–157] to the other ground state hyperfine level $5S_{1/2}(F = 1)$. These effects give rise to Doppler-free transparency peaks of the $6P_{1/2}$ hyperfine levels and has been utilized for the hyperfine measurement of the $6P_{1/2}$ state [151].

The energy level configuration of the V-type system with VIPO at IR transition is shown in Fig. 6.1b. The interference (or beating) of the two counter-propagating IR laser fields (i.e., probe and control) addressing the $5S_{1/2}(F = 2) \rightarrow 5P_{3/2}(F = 3)$ transition induces a temporal modulation of population difference between the upper level $5P_{3/2}(F = 3)$ and lower level $5S_{1/2}(F = 2)$, a phenomenon which is called population oscillation [138–144]. The beating frequency of the fields is $\delta = -2k_1 v$ where, k_1 is the wavevector of the 780 nm laser and v is the velocity of the atom in the direction of the probe. The beat frequency is dependent on the velocity of the atom and hence the phenomenon is called velocity induced population oscillation (VIPO) [74, 77]. The Hamiltonian, H of the V-type system under the electric-dipole and rotating-wave approximation and in rotating frame is expressed as

$$H = \frac{\hbar}{2}\left\{(\Omega_c + \Omega_p e^{i\delta t})\,|1\rangle\langle 2| + \Omega_{pu}\,|1\rangle\langle 3| - \Delta_c\,|2\rangle\langle 2| - \Delta_{pu}\,|3\rangle\langle 3| + h.c.\right\}, \quad (6.1)$$

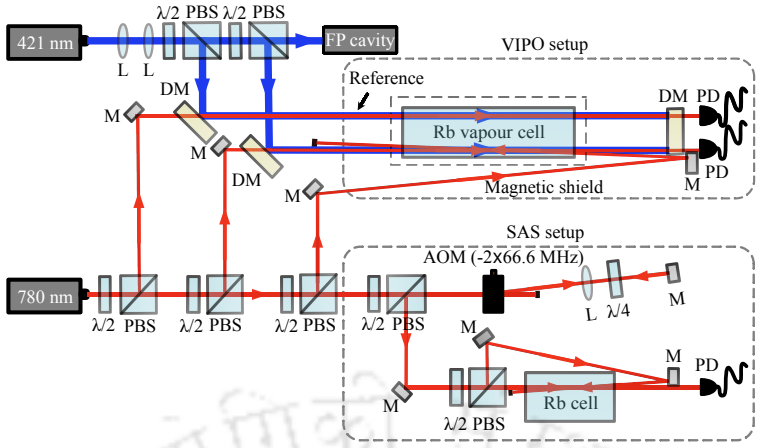

FIGURE 6.2: The experimental set-up for studying the effect of detuning on the VIPO dip in a V-type system and optical pumping system.

where $5S_{1/2}(F = 2) = |1\rangle$, $5P_{3/2}(F = 3) = |2\rangle$, $6P_{1/2}(F = 1) = |3\rangle$, $5S_{1/2}(F = 1) = |4\rangle$, Ω_p (and Ω_c) is the Rabi frequency of the probe (and control) laser driving the $5S_{1/2}(F = 2) \rightarrow 5P_{3/2}(F = 3)$ transition and Ω_{pu} is the Rabi frequency of the pump laser driving the $5S_{1/2}(F = 2) \rightarrow 6P_{1/2}(F = 1)$ transition. The frequency of the probe (and control) lasers are ω_p (and ω_c) and $\delta = (\omega_p - k_1 v) - (\omega_c + k_1 v) = -2k_1 v$ is the Doppler frequency difference between IR probe and control beams (since these two laser fields are from the same laser source i.e. $\omega_p = \omega_c$). $\Delta_c = \omega_c - (\omega_2 - \omega_1) + k_1 v$ is the detuning of the 780 nm control laser and $\Delta_{pu} = \omega_{pu} - (\omega_3 - \omega_1) - k_2 v$ is the detuning of the blue pump laser for moving atoms with velocity v along the direction of the probe laser and k_2 is the wavevector of the 421 nm laser.

The atom-field interaction is described by writing the Liouville-von Neumann equation for the density matrix

$$\dot{\rho} = -\frac{i}{\hbar}[\mathrm{H}, \rho] - \frac{1}{2}\{\Gamma, \rho\}, \tag{6.2}$$

where ρ is the atomic density operator, Γ is the relaxation operator defined as $\langle i|\,\Gamma\,|j\rangle = \gamma_i \delta_{ij}$ ($\delta_{ij} = 1$ if $i = j$ and 0 if $i \neq j$) and γ_i is the decay rate of state $|i\rangle$. γ_3 includes optical pumping of population to the other ground hyperfine level and Π_g which is ground states mixing rate [158–160]. The equations of motion for the density matrix (corresponding to a V-type configuration given in Fig. 6.1b) is obtained by substituting Eq. 6.1 in Eq.

6.2. The resulting equations of motion (given in Eq. A.1) are time dependent and can be solved using the Floquet expansion given as

$$\rho_{ij}(t) = \sum_{n=-\infty}^{\infty} \rho_{ij}^{(n)}(t) e^{in\delta t}, \tag{6.3}$$

where $\rho_{ij}^{(n)}(t)$ are the n^{th} harmonic amplitudes. Substitution of Eq. 6.3 in Eq. A.1 and comparing the coefficients with same factor $e^{in\delta t}$, the time dependence of the equations of motion is removed. In the steady state condition ($\dot{\rho}_{ij}^{(n)} = 0$ for all n, i and j), the imaginary part of the zeroth harmonic $\rho_{12}^{(0)}$ and first harmonic $\rho_{12}^{(+1)}$ corresponds to the IR pump and probe absorption respectively and all the other harmonics are for wave-mixing [161].

6.3.2 The optical pumping system

The energy level configuration of the optical pumping system is shown in Fig. 6.1c. The absorption of the probe driving the $5S_{1/2}(F = 2) \rightarrow 5P_{3/2}(F = 3)$ transition is increased by optical pumping of population to the upper ground hyperfine level $5S_{1/2}(F = 2)$ [155–157] in the presence of the blue pump laser driving the $5S_{1/2}(F = 1) \rightarrow 6P_{1/2}$ transition. The effect gives rise to Doppler-free enhanced absorption (EA) peaks of $6P_{1/2}$ hyperfine levels and again has been utilized for the hyperfine measurement of the $6P_{1/2}$ state [151].

The energy level configuration of the optical pumping system with VIPO at IR transition is shown in Fig. 6.1d. The beating of the IR probe and control laser fields on $5S_{1/2}(F = 2) \rightarrow 5P_{3/2}(F = 3)$ transition induces a VIPO dip on the EA peaks of the $6P_{1/2}$ hyperfine levels [74, 77]. The Hamiltonian, H of the optical pumping system under electric-dipole and rotating-wave approximation and in the rotating frame is expressed as

$$H = \frac{\hbar}{2}\{(\Omega_c + \Omega_p e^{i\delta t}) |1\rangle \langle 2| + \Omega_{pu} |4\rangle \langle 3| - \Delta_c |2\rangle \langle 2| - \Delta_{pu} |3\rangle \langle 3| + h.c.\}, \tag{6.4}$$

where $5S_{1/2}(F = 2) = |1\rangle$, $5P_{3/2}(F = 3) = |2\rangle$, $5S_{1/2}(F = 1) = |3\rangle$ and $6P_{1/2}(F = 1) = |4\rangle$.

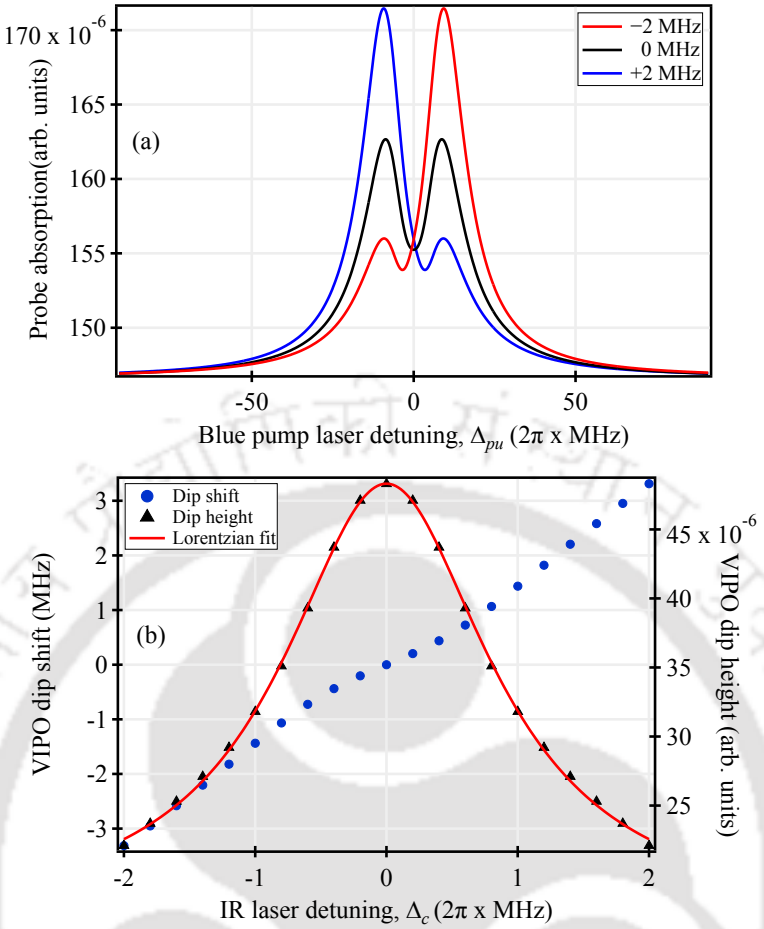

FIGURE 6.3: (a) Theoretically calculated probe absorption (ρ_{12}^{+1}) vs blue pump laser detuning (Δ_{pu}) for three different IR laser detuning i.e. lock-offset of IR laser. (b) The VIPO dip position relative to the EA peaks and VIPO dip height vs IR detunings for $\Omega_c = 2\pi \times 10$ MHz, $\Omega_{pu} = 2\pi \times 6$ MHz, $\Gamma_2 = 2\pi \times 6$ MHz, $\Gamma_3 = 2\pi \times 1.27$ MHz, $\Pi_g = 2\pi \times 40$ kHz. The linewidth of the spectrum (dip height vs IR detuning) is around $2\pi \times 2$ MHz as obtained from the Lorentzian fit.

The equations of motion for the density matrix (corresponding to EA configuration given in Fig. 6.1d) is obtained by substituting Eq. 6.4 in Eq. 6.2. The resulting equations of motion (given in Eq. A.3) are also time dependent and can be solved using the Floquet expansion of the density matrix element ρ_{ij} given in Eq. 6.3. The absorption of the probe laser is proportional to the imaginary part of $\rho_{12}^{(+1)}$ and is plotted in Fig. 6.3a with detuning of the pump laser (Δ_{pu}) for various detunings of probe and control IR laser.

The VIPO dip inside the EA spectrum shifts with the IR laser detuning from the line center of the transition. The VIPO dip shifts to the left of the line center of the EA peak when the IR frequency is red detuned (see red trace of Fig. 6.3a when lock offset

is -2 MHz) and shifts to the right when the IR frequency is blue detuned (see the blue trace of Fig. 6.3a when lock offset is +2 MHz). When the IR laser frequency is locked to resonance, the VIPO dip is symmetrical about the line center of the EA peak (see the black trace of Fig. 6.3a). In order to quantify the shift, the spectrum is fitted with a function given as

$$A_1 + A_2 e^{-\frac{(\Delta_{pu}-A_4)^2}{(A_3)^2}} \frac{A_5}{(\Delta_{pu}-A_4)^2 + A_5} - A_6 e^{-\frac{(\Delta_{pu}-A_8)^2}{(A_7)^2}}, \tag{6.5}$$

where $A_1,\ A_2,\ \cdots A_8$ are fit parameters. The parameters $A_2,\ A_3,\ A_4$ and A_5 corresponds to the EA peaks and $A_6,\ A_7$ and A_8 are for the VIPO dip. The fit parameters A_6 and A_8 gives the height and position of the VIPO dip respectively.

For the numerically simulated plots, we plot the VIPO dip height (A_6) and the VIPO dip center (A_8) vs IR laser detuning from -2 MHz to +2 MHz in steps of 200 kHz in Fig. 6.3b. The VIPO dip height is maximum for $\Delta_c = 0$ ($\Delta_c = \Delta_p$) and decreases with $|\Delta_c|$. The VIPO dip height (A_6) vs IR laser detuning is fitted with a Lorentzian profile whose linewidth is found to be around $2\pi\times2$ MHz which is sub-natural. The VIPO dip position with respect to the EA peak is shown in Fig. 6.3b with blue dots which is symmetric but non-linear. We also see similar behavior of the VIPO dip in the case of the transparency spectrum of V-system.

6.4 Experimental results

In this section, we study the effect of the VIPO dip with IR laser detuning. The frequency of the IR laser is downshifted by around 133 MHz using AOM in the double pass configuration and is locked to the cross-over peak F=(2,3) of the saturated absorption spectroscopy (SAS) set-up (see set-up of Fig. 6.2). The frequency of the AOM is varied from 2×66.0 MHz to 2×67.5 MHz in steps of 2×100 kHz around the cross-over resonance. The linewidth of the crossover peak in the SAS set-up is around $2\pi\times12$ MHz.

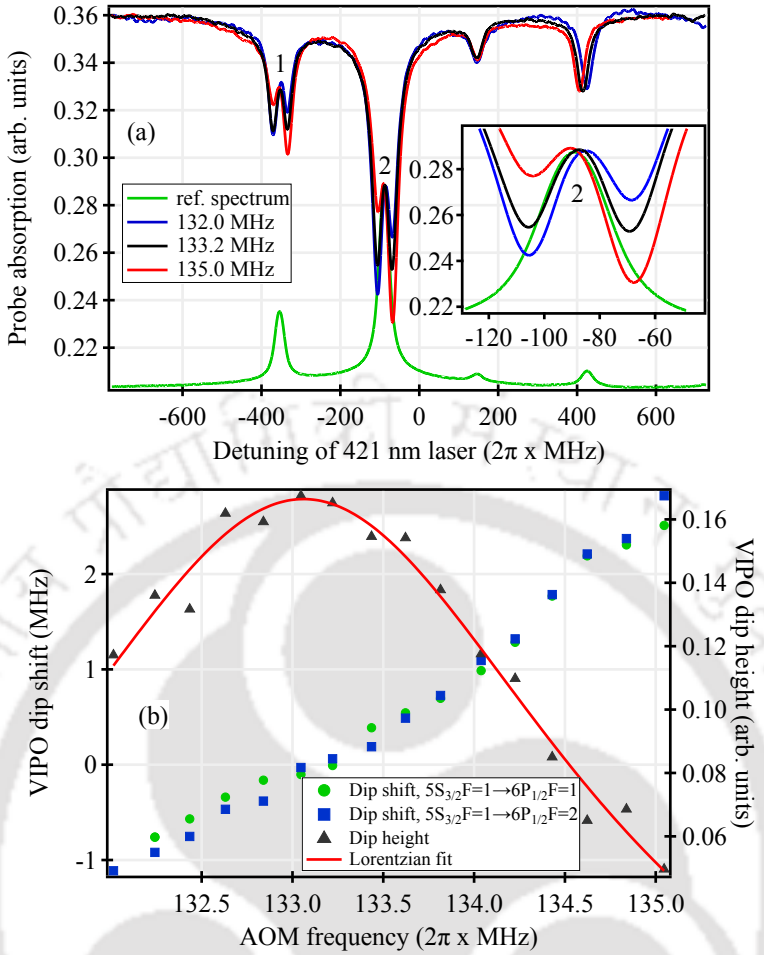

FIGURE 6.4: (a) The absorption spectra of the $6P_{1/2}$ hyperfine levels for various AOM frequencies. (b) The corresponding analysis of the VIPO dip shift from the line center of the absorption peak and height with the AOM frequency. The linewidth is $2\pi \times 3.8$ MHz as obtained from the Lorentzian fit.

The power of the blue pump laser used in the experiment is 10.05 mW (or peak intensity of 208 mW/cm^2). The power of the IR probe and control laser beams are 42 μW and 3.05 mW respectively (which correspond to peak intensity of 1.8 mW/cm^2 and 129 mW/cm^2). Fig. 6.4a shows the EA spectra (for 3 AOM frequencies) which corresponds to the optical pumping system shown in Fig. 6.1d. The VIPO dip shifts to the left from the line center of the EA peak when the AOM frequency is 132.0 MHz (see the red trace of Fig. 6.4a) and shifts to the right when the AOM frequency is 135.0 MHz (see the blue trace of Fig. 6.4a). When the AOM frequency is 133.2 MHz, the VIPO dip line center is nearly coinciding with the line center of the EA peak (see the black trace of Fig. 6.4a). Fig. 6.4b shows a corresponding analysis of the VIPO dip shift and height with the AOM frequency. The height of the VIPO dip is highest when the line

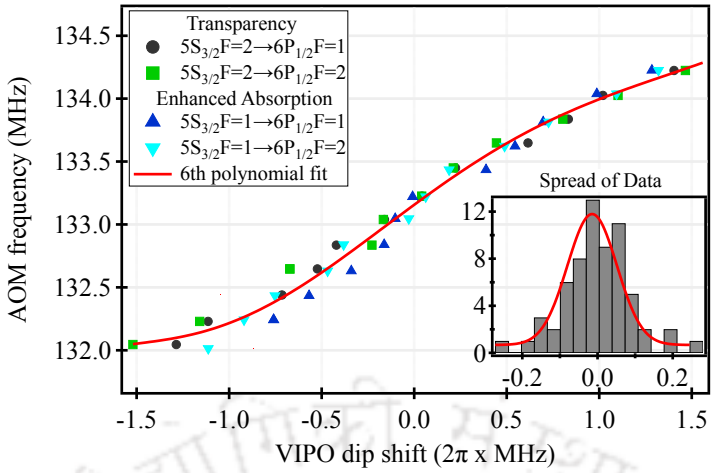

FIGURE 6.5: AOM frequency with the VIPO dip shift in MHz for Transparency and EA peaks. The spread of data from the mean lock point is shown in the inset. The precise lock point is (133.17± 0.10) MHz as obtained from the polynomial fit of n=6.

center of the EA peak and the VIPO dip coincide (i.e. zero shift of the dip). The zero shift of the VIPO dip corresponds to the precise lock point of the laser. The VIPO dip height vs AOM frequency is fitted with a Lorentzian profile whose linewidth is found to be around $2\pi\times$ 3.8 MHz which is sub-natural. We observe a similar behavior for the V-type configuration.

The precise lock point of the IR laser is determined from the plot of AOM frequency vs VIPO dip shift in Fig. 6.5 of the Transparency and EA peaks combined. The resulting curve is fitted to a polynomial function of sixth-order. The AOM frequency corresponding to a VIPO dip shift of zero is obtained from the polynomial fit and is determined to be (133.17 ±0.10) MHz. This frequency represents the precise lock point of the IR laser, as it corresponds to the resonance of IR laser on the $5S_{1/2}(F{=}2) \rightarrow 5P_{3/2}(F{=}3)$ transition. The error in the lock point is determined from the spread of the data in the plot of VIPO dip shift vs AOM frequency. The spread of the data is shown in the inset of Fig. 6.5, and it is fitted to a Gaussian distribution. The standard deviation of the Gaussian distribution is taken as the error in the lock point and is found to be around 0.10 MHz.

6.5 Conclusions

In conclusion we have presented a detailed experimental study on the effect of detuning on VIPO dip for a Doppler mismatched double resonance at 780 nm and 421 nm in ^{87}Rb that measures the shift of the VIPO dip from the line center of the transparency (or EA) peaks. This shift is due to the lock offset of the resonantly driving laser. The VIPO dip shift vs IR detuning is non-linear but symmetrical. The width of the line profile for the VIPO dip height vs the IR laser detuning is sub-natural. This effect is used to precisely determine the locking point of the IR laser on the $5S_{1/2}(F = 2) \rightarrow 5P_{3/2}(F = 3)$ transition. The lock offset measurement by this method has an uncertainty of around 100 kHz which is 1/100 times the linewidth of SAS of 12 MHz.

This chapter has been published as:

Effect of detuning on velocity induced population oscillation

Dangka Shylla, Elijah Nyakang'o Ogaro, Rajnandan Choudhury Das and Kanhaiya Pandey

Eur. Phys. J. D, (2022) 76:125. https://doi.org/10.1140/epjd/s10053-022-00431-5

Chapter 7

Conclusions and Future work

In conclusion, the thesis reports on the theoretical and experimental studies of closed loop multi-level systems, where EIT is dependent on the phase difference between the electromagnetic fields forming the loop. We first described the theoretical study of a phase-dependent EIT system in Rb using a six-level loopy ladder system involving the Rydberg states for the phase sensitive MW or RF electrometry. This system improves the sensitivity by two orders of magnitude and removes the drawback of the phase insensitivity of the previous demonstrations on MW or RF electrometry using the Rydberg states. Due to the Rydberg states properties, this system also has the advantage of the large frequency range of operation ranging from radio frequency (RF), MW to terahertz regime. The spatial resolution by this method is sub-wavelength $\lambda_{MW}/650$. This method provides a great opportunity to characterize the MW or RF electric fields completely including the propagation direction and the wavefront. The theoretical study of the phase-dependent EIT system was then demonstrated in a closed loop double Λ-type system using a Rb vapour cell at room temperature. We studied the phase-dependent EIT (i.e., atomic coherence based interferometry) in two different configuration of a closed loop double Λ-type system. The first configuration involves the excited states with same decay rates at the 780 nm transition and the second configuration involves

the excited states with different decay rates at the 780 nm and 420 nm transitions. We observed similar behavoiur in term of the frequency response of the two systems.

From the above theoretical study in chapter 3, the sensitivity of the MW field measurements can be improved by employing the cold atoms as cold atoms reduce the Doppler effect and also minimizes the collisions and transit time dephasing effect. Taking this into consideration, we also set up the cold atom experiments and so far we have characterized the ^{85}Rb atoms in the MOT using the $5S_{1/2}(F = 3) \rightarrow 5P_{3/2}(F = 4)$ broad cyclic IR transition at 780 nm where we trap around 1.5×10^{8} number of atoms at a typical temperature of 500 μK. In laser cooling and trapping experiments, the temperature of the cold atoms is sensitive to the lock point of the laser fields. The laser locking can have an offset from the line center of the transition which depends upon the linewidth of the transition. In order to determine the laser lock offset on a particular atomic transition, we also present an experimental study on the effect of detuning on a velocity-induced population oscillation (VIPO) dip. We utilized this effect to precisely determine the locking point of the IR laser on the $5S_{1/2}(F=2) \rightarrow 5P_{3/2}(F=3)$ transition. The lock offset measurement by this method has an uncertainty of around 100 kHz which is 1/100 times the linewidth of SAS of 12 MHz.

Our future objective is to experimentally realize the theoretical study of the phase sensitivity of the six-level loopy ladder system involving the Rydberg states that was desribed in chapter 3 of the thesis. We will further utilized this study in cold atoms as the cold atoms reduce the doppler effect, collisions, decoherence brought by transit time broadening and thus improve the sensitivity of the MW field measurement. The cold atoms prepared at 780 nm broad transition in chapter 5 are also ready to be loaded into a second stage narrow linewidth cooling at a 420 nm open transition, where we finally realized the lower temperature it can offer due to the doppler cooling limit. This will help create the high phase-space density atomic cloud necessary to achieve quantum degeneracy.

Appendix A

V-type and Optical pumping system

A.0.1 V-type system

The dynamics of the atom-field interactions for the V-type system with VIPO effect at IR transtion is obtained from Eq. 6.1 and 6.2 which gives the following set of equations of motion with time-dependent coefficients:

$$\begin{aligned}
\dot{\rho}_{12} =& \frac{i}{2}(\Omega_c + \Omega_p e^{i\delta t})(\rho_{11} - \rho_{22}) - \frac{i\Omega_{pu}}{2}\rho_{32} - \gamma_{12}\rho_{12},\\
\dot{\rho}_{13} =& \frac{i\Omega_{pu}}{2}(\rho_{11} - \rho_{33}) - \gamma_{13}\rho_{13} - \frac{i}{2}(\Omega_c + \Omega_p e^{i\delta t})\rho_{23},\\
\dot{\rho}_{14} =& -\frac{i\Omega_{pu}}{2}\rho_{34} - \gamma_{14}\rho_{14} - \frac{i}{2}(\Omega_c + \Omega_p e^{i\delta t})\rho_{24},\\
\dot{\rho}_{22} =& \frac{i}{2}(\Omega_c + \Omega_p e^{i\delta t})\rho_{21} - \frac{i}{2}(\Omega_c^* + \Omega_p^* e^{-i\delta t})\rho_{12} - \Gamma_2\rho_{22},\\
\dot{\rho}_{23} =& -\frac{i}{2}(\Omega_c^* + \Omega_p^* e^{-i\delta t})\rho_{13} + \frac{i\Omega_{pu}}{2}\rho_{21} - \gamma_{23}\rho_{23},\\
\dot{\rho}_{24} =& -\frac{i}{2}(\Omega_c^* + \Omega_p^* e^{-i\delta t})\rho_{14} - \gamma_{24}\rho_{24},\\
\dot{\rho}_{33} =& -\frac{i\Omega_{pu}^*}{2}\rho_{13} + \frac{i\Omega_{pu}}{2}\rho_{31} - \Gamma_3\rho_{33},\\
\dot{\rho}_{34} =& -\frac{i\Omega_{pu}^*}{2}\rho_{14} - \gamma_{34}\rho_{34},\\
\dot{\rho}_{44} =& \Gamma_{34}\rho_{33} + \Pi_g(\rho_{11} - \rho_{44}),
\end{aligned} \tag{A.1}$$

where $\gamma_{12} = i\Delta_c + \gamma_{12}^{dec}$, $\gamma_{13} = i\Delta_{pu} + \gamma_{13}^{dec}$, $\gamma_{14} = \gamma_{14}^{dec}$, $\gamma_{23} = i(\Delta_{pu} - \Delta_c) + \gamma_{23}^{dec}$, $\gamma_{24} = -i\Delta_c + \gamma_{24}^{dec}$, $\gamma_{34} = -i\Delta_{pu} + \gamma_{34}^{dec}$, $\Gamma_1 = \Gamma_4 = \Pi_g$ and $\Gamma_3 = \Gamma_{31} + \Gamma_{34}$. $\gamma_{ij}^{dec} = \frac{1}{2}(\Gamma_i + \Gamma_j)$ is the decoherence rate between level $|i\rangle$ and $|j\rangle$.

The absorption of the probe field is obtained by considering the steady state solution of Eq. A.1 to first order in the Floquet expansion. The substitution of truncated series of Eq. 6.3 into Eq. A.1 yields a set of steady state equations of motion of the V-type system. The $\rho_{12}^{(+1)}$ density matrix element in the Floquet expansion is given as

$$\begin{aligned}
\rho_{12}^{(+1)} =& \frac{i\Omega_p(\rho_{11}^{(0)} - \rho_{22}^{(0)})}{2(\gamma_{12} + i\delta)} + \frac{i\Omega_c(\rho_{11}^{(+1)} - \rho_{22}^{(+1)})}{2(\gamma_{12} + i\delta)}\\
& - \frac{i\Omega_{pu}\rho_{32}^{(+1)}}{2(\gamma_{12} + i\delta)},
\end{aligned} \tag{A.2}$$

where $(\rho_{11}^{(0)} - \rho_{22}^{(0)})$ is the saturation population inversion induces by the IR pump in the presence of the blue pump, $(\rho_{11}^{(+1)} - \rho_{22}^{(+1)})$ is the population oscillation difference induced by the beating of the fields on the IR transition and $\rho_{32}^{(+1)}$ is the coherence oscillation component. The Doppler broadened spectrum of Eq. A.2 is accounted for by thermal averaging over all the velocities of the atoms in the vapor cell.

A.0.2 Optical pumping system

Similarly, the dynamics of the atom-field interactions for the optical pumping configuration with VIPO effect at IR transtion is obtained from Eq. 6.4 and 6.2 which gives the following set of equations of motion with time-dependent coefficients:

$$\begin{aligned}
\dot{\rho}_{12} =& \frac{i}{2}(\Omega_c + \Omega_p e^{i\delta t})(\rho_{11} - \rho_{22}) - \gamma_{12}\rho_{12}, \\
\dot{\rho}_{13} =& -\frac{i}{2}(\Omega_c + \Omega_p e^{i\delta t})\rho_{23} + \frac{i\Omega_{pu}^*}{2}\rho_{14} - \gamma_{13}\rho_{13}, \\
\dot{\rho}_{14} =& -\frac{i}{2}(\Omega_c + \Omega_p e^{i\delta t})\rho_{24} + \frac{i\Omega_{pu}}{2}\rho_{13} - \gamma_{14}\rho_{14}, \\
\dot{\rho}_{22} =& \frac{i}{2}(\Omega_c + \Omega_p e^{i\delta t})\rho_{21} - \frac{i}{2}(\Omega_c^* + \Omega_p^* e^{-i\delta t})\rho_{12} \\
& - \Gamma_2\rho_{22}, \\
\dot{\rho}_{23} =& -\frac{i}{2}(\Omega_c^* + \Omega_p^* e^{-i\delta t})\rho_{13} - \gamma_{23}\rho_{23} + \frac{i\Omega_{pu}^*}{2}\rho_{24}, \\
\dot{\rho}_{24} =& -\frac{i}{2}(\Omega_c^* + \Omega_p^* e^{-i\delta t})\rho_{14} - \gamma_{24}\rho_{24} + \frac{i\Omega_{pu}}{2}\rho_{23}, \\
\dot{\rho}_{33} =& -\frac{i\Omega_{pu}}{2}\rho_{43} + \frac{i\Omega_{pu}^*}{2}\rho_{34} - \Gamma_3\rho_{33}, \\
\dot{\rho}_{34} =& -\frac{i\Omega_{pu}}{2}(\rho_{33} - \rho_{44}) - \gamma_{34}\rho_{34}, \\
\dot{\rho}_{44} =& -\frac{i\Omega_{pu}^*}{2}\rho_{34} + \frac{i\Omega_{pu}}{2}\rho_{43} + \Gamma_{34}\rho_{33} + \Pi_g(\rho_{11} - \rho_{44}),
\end{aligned} \tag{A.3}$$

where $\gamma_{12} = i\Delta_c + \gamma_{12}^{dec}$, $\gamma_{13} = \gamma_{13}^{dec}$, $\gamma_{14} = i\Delta_{pu} + \gamma_{14}^{dec}$, $\gamma_{23} = -i\Delta_c + \gamma_{23}^{dec}$, $\gamma_{24} = i(\Delta_{pu} - \Delta_c) + \gamma_{24}^{dec}$, $\gamma_{34} = i\Delta_{pu} + \gamma_{34}^{dec}$, and $\gamma_{ij}^{dec} = \frac{1}{2}(\Gamma_i + \Gamma_j)$.

The absorption of the probe field obtained by considering the steady state solution of Eq. A.3 to first order in the Floquet expansion is given by density matrix element $\rho_{12}^{(+1)}$ as

$$\rho_{12}^{(+1)} = \frac{i\Omega_p(\rho_{11}^{(0)} - \rho_{22}^{(0)})}{2(\gamma_{12} + i\delta)} + \frac{i\Omega_c(\rho_{11}^{(+1)} - \rho_{22}^{(+1)})}{2(\gamma_{12} + i\delta)}. \tag{A.4}$$

The Doppler broadened spectrum of the probe, is obtained by thermal averaging of Eq. A.4 over all the velocities of the atoms in the vapor cell.

Bibliography

[1] D. A. Steck, "Rubidium 85 D line data," 12 2010. [Online]. Available: http://steck.us/alkalidata

[2] ——, "Rubidium 87 D line data," 12 2010. [Online]. Available: http://steck.us/alkalidata

[3] C. Glaser, F. Karlewski, J. Kluge, J. Grimmel, M. Kaiser, A. Günther, H. Hattermann, M. Krutzik, and J. Fortágh, "Absolute frequency measurement of rubidium $5s{-}6p$ transitions," *Phys. Rev. A*, vol. 102, p. 012804, Jul 2020. [Online]. Available: https://link.aps.org/doi/10.1103/PhysRevA.102.012804

[4] S. E. Harris, J. E. Field, and A. Imamoğlu, "Nonlinear optical processes using electromagnetically induced transparency," *Phys. Rev. Lett.*, vol. 64, no. 10, pp. 1107–1110, Mar 1990.

[5] A. Lezama, S. Barreiro, and A. M. Akulshin, "Electromagnetically induced absorption," *Phys. Rev. A*, vol. 59, pp. 4732–4735, Jun 1999. [Online]. Available: https://link.aps.org/doi/10.1103/PhysRevA.59.4732

[6] E. Arimondo, "V coherent population trapping in laser spectroscopy," ser. Progress in Optics, E. Wolf, Ed. Elsevier, 1996, vol. 35, pp. 257 – 354. [Online]. Available: http://www.sciencedirect.com/science/article/pii/S0079663808705316

[7] G. S. Agarwal, "Inhibition of spontaneous emission noise in lasers without inversion," *Phys. Rev. Lett.*, vol. 67, no. 8, pp. 980–982, Aug 1991.

[8] S. E. Harris, "Lasers without inversion: Interference of lifetime-broadened resonances," *Phys. Rev. Lett.*, vol. 62, pp. 1033–1036, Feb 1989. [Online]. Available: https://link.aps.org/doi/10.1103/PhysRevLett.62.1033

[9] H. Wu, M. Xiao, and J. Gea-Banacloche, "Evidence of lasing without inversion in a hot rubidium vapor under electromagnetically-induced-transparency conditions," *Phys. Rev. A*, vol. 78, p. 041802, Oct 2008. [Online]. Available: https://link.aps.org/doi/10.1103/PhysRevA.78.041802

[10] D. F. Phillips, A. Fleischhauer, A. Mair, R. L. Walsworth, and M. D. Lukin, "Storage of light in atomic vapor," *Phys. Rev. Lett.*, vol. 86, pp. 783–786, Jan 2001. [Online]. Available: http://link.aps.org/doi/10.1103/PhysRevLett.86.783

[11] L. Karpa and M. Weitz, "A stern–gerlach experiment for slow light," *Nature Physics*, vol. 2, no. 5, pp. 332–335, May 2006. [Online]. Available: https://doi.org/10.1038/nphys284

[12] O. Kocharovskaya, Y. Rostovtsev, and M. O. Scully, "Stopping light via hot atoms," *Phys. Rev. Lett.*, vol. 86, pp. 628–631, Jan 2001. [Online]. Available: https://link.aps.org/doi/10.1103/PhysRevLett.86.628

[13] C. Goren, A. D. Wilson-Gordon, M. Rosenbluh, and H. Friedmann, "Atomic four-level N-systems," *Phys. Rev. A*, vol. 69, p. 053818, May 2004. [Online]. Available: http://link.aps.org/doi/10.1103/PhysRevA.69.053818

[14] Y. Zhang, U. Khadka, B. Anderson, and M. Xiao, "Temporal and spatial interference between four-wave mixing and six-wave mixing channels," *Physical Review Letters*, vol. 102, no. 1, p. 013601, 2009. [Online]. Available: http://link.aps.org/abstract/PRL/v102/e013601

[15] R. T. Willis, F. E. Becerra, L. A. Orozco, and S. L. Rolston, "Four-wave mixing in the diamond configuration in an atomic vapor," *Physical Review A (Atomic, Molecular, and Optical Physics)*, vol. 79, no. 3, p. 033814, 2009. [Online]. Available: http://link.aps.org/abstract/PRA/v79/e033814

[16] Y.-q. Li and M. Xiao, "Observation of quantum interference between dressed states in an electromagnetically induced transparency," *Phys. Rev. A*, vol. 51, pp. 4959–4962, Jun 1995. [Online]. Available: https://link.aps.org/doi/10.1103/PhysRevA.51.4959

[17] G. S. Agarwal, "Nature of the quantum interference in electromagnetic-field-induced control of absorption," *Phys. Rev. A*, vol. 55, pp. 2467–2470, Mar 1997. [Online]. Available: https://link.aps.org/doi/10.1103/PhysRevA.55.2467

[18] S. Khan, V. Bharti, and V. Natarajan, "Role of dressed-state interference in electromagnetically induced transparency," *Physics Letters A*, vol. 380, no. 48, pp. 4100–4104, 2016. [Online]. Available: https://www.sciencedirect.com/science/article/pii/S0375960116313433

[19] S. Jin, Y. Li, and M. Xiao, "Hyperfine spectroscopy of highly-excited atomic states based on atomic coherence," *Optics Communications*, vol. 119, no. 1-2, pp. 90 – 96, 1995. [Online]. Available: http://www.sciencedirect.com/science/article/B6TVF-3XWS0KM-3Y/2/6efbe70063717df4057852a0a3fc0221

[20] K. Motomura and M. Mitsunaga, "High-resolution spectroscopy of hyperfine zeeman components of the sodium d1 line by coherent population trapping," *J. Opt. Soc. Am. B*, vol. 19, no. 10, pp. 2456–2460, Oct 2002. [Online]. Available: http://opg.optica.org/josab/abstract.cfm?URI=josab-19-10-2456

[21] A. Krishna, K. Pandey, A. Wasan, and V. Natarajan, "High-resolution hyperfine spectroscopy of excited states using electromagnetically induced transparency," *EPL (Europhysics Letters)*, vol. 72, no. 2, pp. 221–227, 2005. [Online]. Available: http://stacks.iop.org/0295-5075/72/221

[22] S. Wielandy and A. L. Gaeta, "Coherent control of the polarization of an optical field," *Phys. Rev. Lett.*, vol. 81, no. 16, pp. 3359–3362, Oct 1998.

[23] K. Pandey, A. Wasan, and V. Natarajan, "Coherent control of magneto-optic rotation," *Journal of Physics B: Atomic, Molecular and Optical Physics*, vol. 41, no. 22, p. 225503 (8pp), 2008. [Online]. Available: http://stacks.iop.org/0953-4075/41/225503

[24] Y. Cui, X. Wang, B. Ren, and Y. Jiang, "Polarization-controlled electromagnetically induced transparency analogue based on multipolar resonances," *Opt. Mater. Express*, vol. 12, no. 9, pp. 3738–3748, Sep 2022. [Online]. Available: http://opg.optica.org/ome/abstract.cfm?URI=ome-12-9-3738

[25] H. Lee, M. Fleischhauer, and M. O. Scully, "Sensitive detection of magnetic fields including their orientation with a magnetometer based on atomic phase coherence," *Phys. Rev. A*, vol. 58, pp. 2587–2595, Sep 1998. [Online]. Available: https://link.aps.org/doi/10.1103/PhysRevA.58.2587

[26] M. Fleischhauer and M. O. Scully, "Quantum sensitivity limits of an optical magnetometer based on atomic phase coherence," *Phys. Rev. A*, vol. 49, pp. 1973–1986, Mar 1994. [Online]. Available: https://link.aps.org/doi/10.1103/PhysRevA.49.1973

[27] V. I. Yudin, A. V. Taichenachev, Y. O. Dudin, V. L. Velichansky, A. S. Zibrov, and S. A. Zibrov, "Vector magnetometry based on electromagnetically induced transparency in linearly polarized light," *Phys. Rev. A*, vol. 82, p. 033807, Sep 2010. [Online]. Available: https://link.aps.org/doi/10.1103/PhysRevA.82.033807

[28] D. Budker and M. Romalis, "Optical magnetometry," *Nat Phys*, vol. 3, p. 227, 2007. [Online]. Available: http://dx.doi.org/10.1038/nphys566

[29] M. Loretz, T. Rosskopf, and C. L. Degen, "Radio-frequency magnetometry using a single electron spin," *Phys. Rev. Lett.*, vol. 110, p. 017602, Jan 2013. [Online]. Available: http://link.aps.org/doi/10.1103/PhysRevLett.110.017602

[30] A. Horsley, G.-X. Du, M. Pellaton, C. Affolderbach, G. Mileti, and P. Treutlein, "Imaging of relaxation times and microwave field strength in a microfabricated vapor cell," *Phys. Rev. A*, vol. 88, p. 063407, Dec 2013. [Online]. Available: https://link.aps.org/doi/10.1103/PhysRevA.88.063407

[31] A. Horsley, G.-X. Du, and P. Treutlein, "Widefield microwave imaging in alkali vapor cells with sub-100 μ m resolution," *New Journal of Physics*, vol. 17, no. 11, p. 112002, 2015. [Online]. Available: http://stacks.iop.org/1367-2630/17/i=11/a=112002

[32] M. A. Guidry, E. Kuchina, I. Novikova, and E. E. Mikhailov, "Characterization of frequency stability in electromagnetically induced transparency-based atomic clocks using a differential detection scheme," *J. Opt. Soc. Am. B*, vol. 34, no. 10, pp. 2244–2249, Oct 2017. [Online]. Available: http://opg.optica.org/josab/abstract.cfm?URI=josab-34-10-2244

[33] Z. Chen, H. M. Lim, C. Huang, R. Dumke, and S.-Y. Lan, "Quantum-enhanced velocimetry with doppler-broadened atomic vapor," *Phys. Rev. Lett.*, vol. 124, p. 093202, Mar 2020. [Online]. Available: https://link.aps.org/doi/10.1103/PhysRevLett.124.093202

[34] M. M. Kash, V. A. Sautenkov, A. S. Zibrov, L. Hollberg, G. R. Welch, M. D. Lukin, Y. Rostovtsev, E. S. Fry, and M. O. Scully, "Ultraslow group velocity and enhanced nonlinear optical effects in a coherently driven hot atomic gas," *Phys. Rev. Lett.*, vol. 82, pp. 5229–5232, Jun 1999. [Online]. Available: https://link.aps.org/doi/10.1103/PhysRevLett.82.5229

[35] Y. Chen, X. G. Wei, and B. S. Ham, "Detuned slow light in the doppler broadened multi-level d2 line of rubidium," *Opt. Express*, vol. 17, no. 3, pp. 1781–1788, Feb 2009. [Online]. Available: http://opg.optica.org/oe/abstract.cfm?URI=oe-17-3-1781

[36] H. M. M. Alotaibi and B. C. Sanders, "Slowing the probe field in the second window of double-double electromagnetically induced transparency," *Phys. Rev. A*, vol. 91, p. 043817, Apr 2015. [Online]. Available: https://link.aps.org/doi/10.1103/PhysRevA.91.043817

[37] P. He, P. M. Tengdin, D. Z. Anderson, A. M. Rey, and M. Holland, "Sub-doppler laser cooling using electromagnetically induced transparency," *Phys. Rev. A*, vol. 95, p. 053403, May 2017. [Online]. Available: https://link.aps.org/doi/10.1103/PhysRevA.95.053403

[38] E. Urban, T. A. Johnson, T. Henage, L. Isenhower, D. D. Yavuz, T. G. Walker, and M. Saffman, "Observation of rydberg blockade between two atoms," *Nature Physics*, vol. 5, no. 2, pp. 110–114, Feb 2009. [Online]. Available: https://doi.org/10.1038/nphys1178

[39] D. Tiarks, S. Schmidt-Eberle, T. Stolz, G. Rempe, and S. Dürr, "A photon–photon quantum gate based on rydberg interactions," *Nature Physics*, vol. 15, no. 2, pp. 124–126, Feb 2019. [Online]. Available: https://doi.org/10.1038/s41567-018-0313-7

[40] O. Firstenberg, C. S. Adams, and S. Hofferberth, "Nonlinear quantum optics mediated by rydberg interactions," *Journal of Physics B: Atomic, Molecular and Optical Physics*, vol. 49, no. 15, p. 152003, jun 2016. [Online]. Available: https://doi.org/10.1088/0953-4075/49/15/152003

[41] M. Saffman, T. G. Walker, and K. Mølmer, "Quantum information with rydberg atoms," *Rev. Mod. Phys.*, vol. 82, pp. 2313–2363, Aug 2010. [Online]. Available: https://link.aps.org/doi/10.1103/RevModPhys.82.2313

[42] M. Moreno-Cardoner, D. Goncalves, and D. E. Chang, "Quantum nonlinear optics based on two-dimensional rydberg atom arrays," *Phys. Rev. Lett.*, vol. 127, p. 263602, Dec 2021. [Online]. Available: https://link.aps.org/doi/10.1103/PhysRevLett.127.263602

[43] S. Sevinçli and T. Pohl, "Microwave control of rydberg atom interactions," *New Journal of Physics*, vol. 16, no. 12, p. 123036, dec 2014. [Online]. Available: https://doi.org/10.1088/1367-2630/16/12/123036

[44] Z.-K. Liu, L.-H. Zhang, B. Liu, Z.-Y. Zhang, G.-C. Guo, D.-S. Ding, and B.-S. Shi, "Deep learning enhanced rydberg multifrequency microwave recognition," *Nature Communications*, vol. 13, no. 1, p. 1997, Apr 2022. [Online]. Available: https://doi.org/10.1038/s41467-022-29686-7

[45] M. T. Simons, A. B. Artusio-Glimpse, A. K. Robinson, N. Prajapati, and C. L. Holloway, "Rydberg atom-based sensors for radio-frequency electric field metrology, sensing, and communications," *Measurement: Sensors*, vol. 18, p. 100273, 2021. [Online]. Available: https://www.sciencedirect.com/science/article/pii/S2665917421002361

[46] D. A. Anderson, R. E. Sapiro, and G. Raithel, "Rydberg atoms for radio-frequency communications and sensing: Atomic receivers for pulsed rf field and phase detection," *IEEE Aerospace and Electronic Systems Magazine*, vol. 35, no. 4, pp. 48–56, 2020.

[47] S. Kumar, H. Fan, H. Kübler, A. J. Jahangiri, and J. P. Shaffer, "Rydberg-atom based radio-frequency electrometry using frequency modulation spectroscopy in room temperature vapor cells," *Opt. Express*, vol. 25, no. 8, pp. 8625–8637, Apr 2017. [Online]. Available: http://opg.optica.org/oe/abstract.cfm?URI=oe-25-8-8625

[48] K. H, S. P., BaluktsianT, LowR, and PfauT, "Coherent excitation of rydberg atoms in micrometre-sized atomic vapour cells," *Nat Photon*, vol. 4, p. 112, 2010. [Online]. Available: http://dx.doi.org/10.1038/nphoton.2009.260

[49] J. A. Sedlacek, A. Schwettmann, H. Kubler, LowR, PfauT, and J. P. Shaffer, "Microwave electrometry with rydberg atoms in a vapour cell using bright atomic resonances," *Nat Phys*, vol. 8, p. 819, 2012. [Online]. Available: http://dx.doi.org/10.1038/nphys2423

[50] J. A. Sedlacek, A. Schwettmann, H. Kübler, and J. P. Shaffer, "Atom-based vector microwave electrometry using rubidium rydberg atoms in a vapor cell," *Phys. Rev. Lett.*, vol. 111, p. 063001, Aug 2013. [Online]. Available: http://link.aps.org/doi/10.1103/PhysRevLett.111.063001

[51] Y. Jiao, X. Han, Z. Yang, J. Li, G. Raithel, J. Zhao, and S. Jia, "Spectroscopy of cesium rydberg atoms in strong radio-frequency fields," *Phys. Rev. A*, vol. 94, p. 023832, Aug 2016. [Online]. Available: http://link.aps.org/doi/10.1103/PhysRevA.94.023832

[52] S. Kumar, H. Fan, H. Kübler, A. J. Jahangiri, and J. P. Shaffer, "Rydberg-atom based radio-frequency electrometry using frequency modulation spectroscopy in room temperature vapor cells," *Opt. Express*, vol. 25, no. 8, pp. 8625–8637, Apr 2017. [Online]. Available: https://opg.optica.org/oe/abstract.cfm?URI=oe-25-8-8625

[53] Y. Jiao, L. Hao, X. Han, S. Bai, G. Raithel, J. Zhao, and S. Jia, "Atom-based radio-frequency field calibration and polarization measurement using cesium nD_J floquet states," *Phys. Rev. Applied*, vol. 8, p. 014028, Jul 2017. [Online]. Available: https://link.aps.org/doi/10.1103/PhysRevApplied.8.014028

[54] M. Jing, Y. Hu, J. Ma, H. Zhang, L. Zhang, L. Xiao, and S. Jia, "Atomic superheterodyne receiver based on microwave-dressed rydberg spectroscopy," *Nature Physics*, vol. 16, no. 9, pp. 911–915, Sep 2020. [Online]. Available: https://doi.org/10.1038/s41567-020-0918-5

[55] M. Kanda, "Standard probes for electromagnetic field measurements," *IEEE Transactions on Antennas and Propagation*, vol. 41, no. 10, pp. 1349–1364, 1993.

[56] ——, "Standard antennas for electromagnetic interference measurements and methods to calibrate them," no. 36, 1994-11-01 00:11:00 1994.

[57] S. S. Sriram, S. A. Kingsley, and J. T. Boyd, "Electro-optical sensor for detecting electric fields," November 30 US Patent 5,267,336 1993.

[58] H. Q. Fan, S. Kumar, R. Daschner, H. Kübler, and J. P. Shaffer, "Subwavelength microwave electric-field imaging using rydberg atoms inside atomic vapor cells," *Opt. Lett.*, vol. 39, no. 10, pp. 3030–3033, May 2014. [Online]. Available: http://opg.optica.org/ol/abstract.cfm?URI=ol-39-10-3030

[59] M. S. Shahriar and P. R. Hemmer, "Direct excitation of microwave-spin dressed states using a laser-excited resonance raman interaction," *Phys. Rev. Lett.*, vol. 65, pp. 1865–1868, Oct 1990. [Online]. Available: https://link.aps.org/doi/10.1103/PhysRevLett.65.1865

[60] W. Maichen, R. Gaggl, E. Korsunsky, and L. Windholz, "Observation of phase-dependent coherent population trapping in optically closed atomic systems," *Europhysics Letters (EPL)*, vol. 31, no. 4, pp. 189–194, aug 1995. [Online]. Available: https://doi.org/10.1209/0295-5075/31/4/001

[61] W. Maichen, F. Renzoni, I. Mazets, E. Korsunsky, and L. Windholz, "Transient coherent population trapping in a closed loop interaction scheme," *Phys. Rev. A*, vol. 53, pp. 3444–3448, May 1996. [Online]. Available: https://link.aps.org/doi/10.1103/PhysRevA.53.3444

[62] N. P. Georgiades, E. S. Polzik, and H. J. Kimble, "Frequency metrology by use of quantum interference," *Opt. Lett.*, vol. 21, no. 20, pp. 1688–1690, Oct 1996. [Online]. Available: http://opg.optica.org/ol/abstract.cfm?URI=ol-21-20-1688

[63] D. Anderson, R. Sapiro, L. Gonçalves, R. Cardman, and G. Raithel, "Optical radio-frequency phase measurement with an internal-state rydberg atom interferometer," *Phys. Rev. Applied*, vol. 17, p. 044020, Apr 2022. [Online]. Available: https://link.aps.org/doi/10.1103/PhysRevApplied.17.044020

[64] M. Bhattarai, S. Khan, V. Natarajan, and K. Pandey, "Laser interferometry based on atomic coherence," *Journal of Physics B: Atomic, Molecular and Optical Physics*, vol. 54, no. 7, p. 075401, apr 2021. [Online]. Available: https://doi.org/10.1088/1361-6455/abe67c

[65] D. P. Lake, M. Mitchell, B. C. Sanders, and P. E. Barclay, "Two-colour interferometry and switching through optomechanical dark mode excitation," *Nature Communications*, vol. 11, no. 1, p. 2208, May 2020. [Online]. Available: https://doi.org/10.1038/s41467-020-15625-x

[66] T. M. Brzozowski, M. Brzozowska, J. Zachorowski, and W. Gawlik, "High Resolution Spectroscopy of Cold, Trapped Atoms," *Acta Physica Polonica A*, vol. 112, no. 5, p. 783, Nov. 2007.

[67] A. D. Cronin, J. Schmiedmayer, and D. E. Pritchard, "Optics and interferometry with atoms and molecules," *Rev. Mod. Phys.*, vol. 81, pp. 1051–1129, Jul 2009. [Online]. Available: https://link.aps.org/doi/10.1103/RevModPhys.81.1051

[68] L. Zhou, S. Long, B. Tang, X. Chen, F. Gao, W. Peng, W. Duan, J. Zhong, Z. Xiong, J. Wang, Y. Zhang, and M. Zhan, "Test of equivalence principle at 10^{-8} level by a dual-species double-diffraction raman atom interferometer," *Phys. Rev. Lett.*, vol. 115, p. 013004, Jul 2015. [Online]. Available: https://link.aps.org/doi/10.1103/PhysRevLett.115.013004

[69] E. A. Cornell and C. E. Wieman, "Nobel lecture: Bose-einstein condensation in a dilute gas, the first 70 years and some recent experiments," *Rev. Mod. Phys.*, vol. 74, pp. 875–893, Aug 2002. [Online]. Available: https://link.aps.org/doi/10.1103/RevModPhys.74.875

[70] M. H. Anderson, J. R. Ensher, M. R. Matthews, C. E. Wieman, and E. A. Cornell, "Observation of bose-einstein condensation in a dilute atomic vapor," *Science*, vol. 269, no. 5221, pp. 198–201, 1995. [Online]. Available: https://www.science.org/doi/abs/10.1126/science.269.5221.198

[71] P. Kumar, A. Singh, V. Bharti, V. Natarajan, and K. Pandey, "Study of CPO resonances on the intercombination line in ^{173}Yb," *Journal of Physics B Atomic Molecular and Optical Physics*, vol. 51, p. 035502, 02 2018.

[72] T. Lauprêtre, S. Kumar, P. Berger, R. Faoro, R. Ghosh, F. Bretenaker, and F. Goldfarb, "Ultranarrow resonance due to coherent population oscillations in a Λ-type atomic system," *Phys. Rev. A*, vol. 85, p. 051805, May 2012. [Online]. Available: https://link.aps.org/doi/10.1103/PhysRevA.85.051805

[73] P. Neveu, M.-A. Maynard, R. Bouchez, J. Lugani, R. Ghosh, F. Bretenaker, F. Goldfarb, and E. Brion, "Coherent population oscillation-based light storage," *Phys. Rev. Lett.*, vol. 118, p. 073605, Feb 2017. [Online]. Available: https://link.aps.org/doi/10.1103/PhysRevLett.118.073605

[74] Nyakang'o, Elijah Ogaro and Pandey, Kanhaiya, "Role of velocity induced coherent population oscillation in saturated fluorescence spectroscopy," *Eur. Phys. J. D*, vol. 74, no. 5, p. 96, 2020. [Online]. Available: https://doi.org/10.1140/epjd/e2020-100519-0

[75] J. R. Boon, E. Zekou, D. J. Fulton, and M. H. Dunn, "Experimental observation of a coherently induced transparency on a blue probe in a doppler-broadened mismatched V-type system," *Phys. Rev. A*, vol. 57, pp. 1323–1328, Feb 1998. [Online]. Available: https://link.aps.org/doi/10.1103/PhysRevA.57.1323

[76] E. A. Chan, S. A. Aljunid, N. I. Zheludev, D. Wilkowski, and M. Ducloy, "Doppler-free approach to optical pumping dynamics in the $6S_{1/2}$˘$5D_{5/2}$ electric quadrupole transition of cesium vapor," *Opt. Lett.*, vol. 41, no. 9, pp. 2005–2008, May 2016. [Online]. Available: http://opg.optica.org/ol/abstract.cfm?URI=ol-41-9-2005

[77] E. O. Nyakang'o and K. Pandey, "Resolving closely spaced levels for doppler mismatched double resonance," *Phys. Rev. A*, vol. 103, p. 013107, Jan 2021. [Online]. Available: https://link.aps.org/doi/10.1103/PhysRevA.103.013107

[78] M. S. Z. Marlan O. Scully, *Quantum Optics*. Cambridge university press, 1997, p. 226.

[79] H. J. Metcalf and P. van der Straten, "Laser cooling and trapping of atoms," *J. Opt. Soc. Am. B*, vol. 20, no. 5, pp. 887–908, May 2003. [Online]. Available: http://opg.optica.org/josab/abstract.cfm?URI=josab-20-5-887

[80] S. H. Autler and C. H. Townes, "Stark effect in rapidly varying fields," *Phys. Rev.*, vol. 100, pp. 703–722, Oct 1955. [Online]. Available: https://link.aps.org/doi/10.1103/PhysRev.100.703

[81] C. Cohen-Tannoudji, J. Dupont-Roc, and G. Grynberg, "Atom–photon interactions: Basic processes and applications," *American Journal of Physics*, vol. 61, no. 6, pp. 572–572, 1993. [Online]. Available: https://doi.org/10.1119/1.17212

[82] J. Dalibard and C. Cohen-Tannoudji, "Laser cooling below the doppler limit by polarization gradients: simple theoretical models," *J. Opt. Soc. Am. B*, vol. 6, no. 11, pp. 2023–2045, Nov 1989. [Online]. Available: http://opg.optica.org/josab/abstract.cfm?URI=josab-6-11-2023

[83] D. J. Wineland, J. Dalibard, and C. Cohen-Tannoudji, "Sisyphus cooling of a bound atom," *J. Opt. Soc. Am. B*, vol. 9, no. 1, pp. 32–42, Jan 1992. [Online]. Available: http://opg.optica.org/josab/abstract.cfm?URI=josab-9-1-32

[84] A. T. Grier, I. Ferrier-Barbut, B. S. Rem, M. Delehaye, L. Khaykovich, F. Chevy, and C. Salomon, "Λ-enhanced sub-doppler cooling of lithium atoms in D_1 gray molasses," *Phys. Rev. A*, vol. 87, p. 063411, Jun 2013. [Online]. Available: https://link.aps.org/doi/10.1103/PhysRevA.87.063411

[85] G. D. Bruce, E. Haller, B. Peaudecerf, D. A. Cotta, M. Andia, S. Wu, M. Y. H. Johnson, B. W. Lovett, and S. Kuhr, "Sub-doppler laser cooling of ^{40}K with raman gray molasses on the D_2 line," *Journal of Physics B: Atomic, Molecular and Optical Physics*, vol. 50, no. 9, p. 095002, apr 2017. [Online]. Available: https://doi.org/10.1088/1361-6455/aa65ea

[86] H. F. Hess, "Evaporative cooling of magnetically trapped and compressed spin-polarized hydrogen," *Phys. Rev. B*, vol. 34, pp. 3476–3479, Sep 1986. [Online]. Available: https://link.aps.org/doi/10.1103/PhysRevB.34.3476

[87] A. Sargsyan, G. Hakhumyan, C. Leroy, Y. Pashayan-Leroy, A. Papoyan, D. Sarkisyan, and M. Auzinsh, "Hyperfine paschen-back regime in alkali metal atoms: consistency of two theoretical considerations and experiment," *J. Opt. Soc. Am. B*, vol. 31, no. 5, pp. 1046–1053, May 2014. [Online]. Available: https://opg.optica.org/josab/abstract.cfm?URI=josab-31-5-1046

[88] J. L. Hall, "Nobel lecture: Defining and measuring optical frequencies," *Rev. Mod. Phys.*, vol. 78, pp. 1279–1295, Nov 2006. [Online]. Available: http://link.aps.org/doi/10.1103/RevModPhys.78.1279

[89] K. Pandey, D. Rathod, A. Singh, and V. Natarajan, "Atomic fountain of laser-cooled yb atoms for precision measurements," *Physical Review A*, vol. 82, pp. 043 429–1, 10 2010.

[90] Klinger, Emmanuel, Sargsyan, Armen, Tonoyan, Ara, Hakhumyan, Grant, Papoyan, Aram, Leroy, Claude, and Sarkisyan, David, "Magnetic field-induced modification of selection rules for rb d2 line monitored by selective reflection from a vapor nanocell," *Eur. Phys. J. D*, vol. 71, no. 8, p. 216, 2017. [Online]. Available: https://doi.org/10.1140/epjd/e2017-80291-6

[91] D. Höckel, M. Scholz, and O. Benson, "A robust phase-locked diode laser system for eit experiments in cesium," *Applied Physics B*, vol. 94, no. 3, p. 429, 2008. [Online]. Available: http://dx.doi.org/10.1007/s00340-008-3313-y

[92] R. J. King and Y. H. Yen, "Probing amplitude, phase, and polarization of microwave field distributions in real time," *IEEE Transactions on Microwave Theory and Techniques*, vol. 29, no. 11, pp. 1225–1231, Nov 1981.

[93] E. N. Ivanov, M. E. Tobar, and R. A. Woode, "Microwave interferometry: application to precision measurements and noise reduction techniques," *IEEE Transactions on Ultrasonics, Ferroelectrics, and Frequency Control*, vol. 45, no. 6, pp. 1526–1536, Nov 1998.

[94] E. N. Ivanov and M. E. Tobar, "Microwave phase detection at the level 10^{-11} rad," *Review of Scientific Instruments*, vol. 80, no. 4, p. 044701, 2009. [Online]. Available: http://dx.doi.org/10.1063/1.3115206

[95] N. S. Mallick, T. N. Dey, and K. Pandey, "Microwave assisted transparency in an m-system," *Journal of Physics B: Atomic, Molecular and Optical Physics*, vol. 50, no. 19, p. 195502, sep 2017. [Online]. Available: https://dx.doi.org/10.1088/1361-6455/aa8a35

[96] U. Volz and H. Schmoranzer, "Precision lifetime measurements on alkali atoms and on helium by beam–gas–laser spectroscopy," *Physica Scripta*, vol. T65, pp. 48–56, jan 1996. [Online]. Available: https://doi.org/10.1088%2F0031-8949%2F1996%2Ft65%2F007

[97] K. Pandey, "Role of different types of subsystems in a doubly driven Λ system in ^{87}rb," *Phys. Rev. A*, vol. 87, p. 043838, Apr 2013. [Online]. Available: http://link.aps.org/doi/10.1103/PhysRevA.87.043838

[98] J. Gea-Banacloche, Y.-q. Li, S.-z. Jin, and M. Xiao, "Electromagnetically induced transparency in ladder-type inhomogeneously broadened media: Theory and experiment," *Phys. Rev. A*, vol. 51, pp. 576–584, Jan 1995. [Online]. Available: https://link.aps.org/doi/10.1103/PhysRevA.51.576

[99] C. C. Kwong, T. Yang, M. S. Pramod, K. Pandey, D. Delande, R. Pierrat, and D. Wilkowski, "Cooperative emission of a coherent superflash of light," *Phys. Rev. Lett.*, vol. 113, p. 223601, Nov 2014. [Online]. Available: https://link.aps.org/doi/10.1103/PhysRevLett.113.223601

[100] S. Khan, V. Bharti, and V. Natarajan, "Role of dressed-state interference in electromagnetically induced transparency," *Physics Letters A*, vol. 380, no. 48, pp. 4100–4104, 2016. [Online]. Available: https://www.sciencedirect.com/science/article/pii/S0375960116313433

[101] A. K. Mohapatra, T. R. Jackson, and C. S. Adams, "Coherent optical detection of highly excited rydberg states using electromagnetically induced transparency," *Phys. Rev. Lett.*, vol. 98, p. 113003, Mar 2007. [Online]. Available: http://link.aps.org/doi/10.1103/PhysRevLett.98.113003

[102] Y.-S. Lee, H.-R. Noh, and H. S. Moon, "Relationship between two- and three-photon coherence in a ladder-type atomic system," *Opt. Express*, vol. 23, no. 3, pp. 2999–3009, Feb 2015. [Online]. Available: http://www.opticsexpress.org/abstract.cfm?URI=oe-23-3-2999

[103] S. M. Iftiquar and V. Natarajan, "Line narrowing of electromagnetically induced transparency in Rb with a longitudinal magnetic field," *Phys. Rev. A*, vol. 79, p.

013808, Jan 2009. [Online]. Available: http://link.aps.org/doi/10.1103/PhysRevA.79.013808

[104] K. Pandey, C. C. Kwong, M. S. Pramod, and D. Wilkowski, "Linear and nonlinear magneto-optical rotation on the narrow strontium intercombination line," *Phys. Rev. A*, vol. 93, p. 053428, May 2016. [Online]. Available: http://link.aps.org/doi/10.1103/PhysRevA.93.053428

[105] C. G. Wade, M. Marcuzzi, E. Levi, J. M. Kondo, I. Lesanovsky, C. S. Adams, and K. J. Weatherill, "A terahertz-driven non-equilibrium phase transition in a room temperature atomic vapour," *Nature Communications*, vol. 9, no. 1, p. 3567, Sep 2018. [Online]. Available: https://doi.org/10.1038/s41467-018-05597-4

[106] D. Shylla, E. N. Ogaro, and K. Pandey, "Highly sensitive atomic based mw interferometry," *Scientific Reports*, vol. 8, p. 8692, 2018. [Online]. Available: https://doi.org/10.1038/s41598-018-27011-1

[107] L. Muanzuala, H. Ravi, K. Sylvan, and V. Natarajan, "Measuring the linewidth of a stabilized diode laser," *CURRENT SCIENCE*, vol. 109, no. 4, pp. 765–767, August 2015. [Online]. Available: http://www.currentscience.ac.in/Volumes/109/04/076...

[108] D. A. Smith and I. G. Hughes, "The role of hyperfine pumping in multilevel systems exhibiting saturated absorption," *American Journal of Physics*, vol. 72, no. 5, pp. 631–637, 2004. [Online]. Available: https://doi.org/10.1119/1.1652039

[109] S. Chu, "Nobel lecture: The manipulation of neutral particles," *Rev. Mod. Phys.*, vol. 70, pp. 685–706, Jul 1998. [Online]. Available: https://link.aps.org/doi/10.1103/RevModPhys.70.685

[110] Y. Castin, H. Wallis, and J. Dalibard, "Limit of doppler cooling," *J. Opt. Soc. Am. B*, vol. 6, no. 11, pp. 2046–2057, Nov 1989. [Online]. Available: http://opg.optica.org/josab/abstract.cfm?URI=josab-6-11-2046

[111] R. Chang, A. L. Hoendervanger, Q. Bouton, Y. Fang, T. Klafka, K. Audo, A. Aspect, C. I. Westbrook, and D. Clément, "Three-dimensional laser cooling at the doppler limit," *Phys. Rev. A*, vol. 90, p. 063407, Dec 2014. [Online]. Available: https://link.aps.org/doi/10.1103/PhysRevA.90.063407

[112] E. L. Raab, M. Prentiss, A. Cable, S. Chu, and D. E. Pritchard, "Trapping of neutral sodium atoms with radiation pressure," *Phys. Rev. Lett.*, vol. 59, pp. 2631–2634, Dec 1987. [Online]. Available: https://link.aps.org/doi/10.1103/PhysRevLett.59.2631

[113] A. Micheli, G. K. Brennen, and P. Zoller, "A toolbox for lattice-spin models with polar molecules," *Nature Physics*, vol. 2, no. 5, pp. 341–347, May 2006.

[114] D. DeMille, "Quantum computation with trapped polar molecules," *Phys. Rev. Lett.*, vol. 88, p. 067901, Jan 2002. [Online]. Available: https://link.aps.org/doi/10.1103/PhysRevLett.88.067901

[115] S. F. Yelin, K. Kirby, and R. Côté, "Schemes for robust quantum computation with polar molecules," *Phys. Rev. A*, vol. 74, p. 050301, Nov 2006. [Online]. Available: https://link.aps.org/doi/10.1103/PhysRevA.74.050301

[116] A. André, D. Demille, J. M. Doyle, M. D. Lukin, S. E. Maxwell, P. Rabl, R. J. Schoelkopf, and P. Zoller, "A coherent all-electrical interface between polar molecules and mesoscopic superconducting resonators," *Nature Physics*, vol. 2, no. 9, pp. 636–642, Sep. 2006.

[117] R. C. Das, D. Shylla, A. Bera, and K. Pandey, "Narrow-line cooling of ^{87}Rb using $5S_{1/2} \rightarrow 6P_{3/2}$ open transition at 420 nm," *arXiv:2205.04054*, 2022. [Online]. Available: https://arxiv.org/abs/2205.04054

[118] E. Arimondo, M. Inguscio, and P. Violino, "Experimental determinations of the hyperfine structure in the alkali atoms," *Rev. Mod. Phys.*, vol. 49, pp. 31–75, Jan 1977. [Online]. Available: https://link.aps.org/doi/10.1103/RevModPhys.49.31

[119] M. S. Safronova and U. I. Safronova, "Critically evaluated theoretical energies, lifetimes, hyperfine constants, and multipole polarizabilities in ^{87}Rb," *Phys. Rev. A*, vol. 83, p. 052508, May 2011. [Online]. Available: https://link.aps.org/doi/10.1103/PhysRevA.83.052508

[120] M. J. Snadden, R. B. M. Clarke, and E. Riis, "Injection-locking technique for heterodyne optical phase locking of a diode laser," *Opt. Lett.*, vol. 22, no. 12, pp. 892–894, Jun 1997. [Online]. Available: http://opg.optica.org/ol/abstract.cfm?URI=ol-22-12-892

[121] X. Wang, X. Chen, J. Hou, D. Yang, and Y. Wang, "Side-mode injection locking characteristics of 150 mw algaas semiconductor lasers," *Optics Communications*, vol. 178, no. 1, pp. 165–173, 2000. [Online]. Available: https://www.sciencedirect.com/science/article/pii/S0030401800006179

[122] E. A. Donley, T. P. Heavner, F. Levi, M. O. Tataw, and S. R. Jefferts, "Double-pass acousto-optic modulator system," *Review of Scientific Instruments*, vol. 76, no. 6, p. 063112, 2005. [Online]. Available: https://doi.org/10.1063/1.1930095

[123] H. D. Do, G. Moon, and H.-R. Noh, "Polarization spectroscopy of rubidium atoms: Theory and experiment," *Phys. Rev. A*, vol. 77, p. 032513, Mar 2008. [Online]. Available: https://link.aps.org/doi/10.1103/PhysRevA.77.032513

[124] V. V. Yashchuk, D. Budker, and J. R. Davis, "Laser frequency stabilization using linear magneto-optics," *Rev. Sci. Instrum.*, vol. 71, pp. 341–346, 2000.

[125] K. Pandey and V. Natarajan, "Splitting of electromagnetically induced transparency under strong-probe conditions due to doppler averaging," *Journal of Physics B: Atomic, Molecular and Optical Physics*, vol. 41, no. 18, p. 185504 (4pp), 2008. [Online]. Available: http://stacks.iop.org/0953-4075/41/185504

[126] M. L. Harris, S. L. Cornish, A. Tripathi, and I. G. Hughes, "Optimization of sub-doppler DAVLL on the rubidium d2 line," *Journal of Physics B: Atomic, Molecular and Optical Physics*, vol. 41, no. 8, p. 085401, apr 2008. [Online]. Available: https://doi.org/10.1088/0953-4075/41/8/085401

[127] M. M. Yee, "Magnetic trapping and transport of ultracold atoms," *University of Toronto*, 2009.

[128] H. Weaver, "Creating and controlling magnetic fields to trap ultracold atoms," *niversity of Colorado, Boulder Physics REU*, 2013.

[129] A. Vorozcovs, M. Weel, S. Beattie, S. Cauchi, and A. Kumarakrishnan, "Measurements of temperature scaling laws in an optically dense magneto-optical trap," *J. Opt. Soc. Am. B*, vol. 22, no. 5, pp. 943–950, May 2005. [Online]. Available: http://opg.optica.org/josab/abstract.cfm?URI=josab-22-5-943

[130] W. Demtroder, *Laser Spectroscopy*. Springer, 1998.

[131] K.-B. Im, H.-Y. Jung, C.-H. Oh, S.-H. Song, P.-S. Kim, and H.-S. Lee, "Saturated absorption signals for the cs D_2 line," *Phys. Rev. A*, vol. 63, p. 034501, Feb 2001. [Online]. Available: https://link.aps.org/doi/10.1103/PhysRevA.63.034501

[132] M. S. Safronova and U. I. Safronova, "Critically evaluated theoretical energies, lifetimes, hyperfine constants, and multipole polarizabilities in ^{87}Rb," *Phys. Rev. A*, vol. 83, p. 052508, May 2011. [Online]. Available: https://link.aps.org/doi/10.1103/PhysRevA.83.052508

[133] C.-B. Li, Y.-M. Yu, and B. K. Sahoo, "Relativistic coupled-cluster-theory analysis of energies, hyperfine-structure constants, and dipole polarizabilities of Cd^+," *Phys. Rev. A*, vol. 97, p. 022512, Feb 2018. [Online]. Available: https://link.aps.org/doi/10.1103/PhysRevA.97.022512

[134] Y.-J. Huang, Y.-C. Guan, Y.-C. Huang, T.-H. Suen, J.-L. Peng, L.-B. Wang, and J.-T. Shy, "Frequency measurement of the 2^1S_0–3^1D_2 two-photon transition in atomic ^{4}He," *Phys. Rev. A*, vol. 97, p. 032516, Mar 2018. [Online]. Available: https://link.aps.org/doi/10.1103/PhysRevA.97.032516

[135] W.-K. Lee and H. S. Moon, "Measurement of absolute frequencies and hyperfine structure constants of $4D_{5/2}$ and $4D_{3/2}$ levels of ^{87}Rb and ^{85}Rb using an optical frequency comb," *Phys. Rev. A*, vol. 92, p. 012501, Jul 2015. [Online]. Available: https://link.aps.org/doi/10.1103/PhysRevA.92.012501

[136] A. Banerjee and V. Natarajan, "Absolute-frequency measurements of the d2 line and fine-structure interval in 39k," *Phys. Rev. A*, vol. 70, p. 052505, 2004.

[137] H. Levine, A. Keesling, A. Omran, H. Bernien, S. Schwartz, A. S. Zibrov, M. Endres, M. Greiner, V. Vuletić, and M. D. Lukin, "High-fidelity control and entanglement of rydberg-atom qubits," *Phys. Rev. Lett.*, vol. 121, p. 123603, Sep 2018. [Online]. Available: https://link.aps.org/doi/10.1103/PhysRevLett.121.123603

[138] E. Baldit, K. Bencheikh, P. Monnier, J. A. Levenson, and V. Rouget, "Ultraslow light propagation in an inhomogeneously broadened rare-earth ion-doped crystal," *Phys. Rev. Lett.*, vol. 95, p. 143601, Sep 2005. [Online]. Available: https://link.aps.org/doi/10.1103/PhysRevLett.95.143601

[139] R. W. Boyd, "Slow and fast light: fundamentals and applications," *Journal of Modern Optics*, vol. 56, no. 18-19, pp. 1908–1915, 2009. [Online]. Available: https://doi.org/10.1080/09500340903159495

[140] G. Piredda and R. Boyd, "Slow light by means of coherent population oscillations: laser linewidth effects," *Journal of the European Optical Society - Rapid publications*, vol. 2, no. 0, 2007. [Online]. Available: http://www.jeos.org/index.php/jeos_rp/article/view/07004

[141] V. S. Zapasskiĭ and G. G. Kozlov, "A saturable absorber, coherent population oscillations, and slow light," *Optics and Spectroscopy*, vol. 100, no. 3, pp. 419–424, Mar 2006. [Online]. Available: https://doi.org/10.1134/S0030400X06030192

[142] M. S. Bigelow, N. N. Lepeshkin, and R. W. Boyd, "Observation of ultraslow light propagation in a ruby crystal at room temperature," *Phys. Rev. Lett.*, vol. 90, p. 113903, Mar 2003. [Online]. Available: https://link.aps.org/doi/10.1103/PhysRevLett.90.113903

[143] P. Kumar, A. K. Singh, V. Bharti, V. Natarajan, and K. Pandey, "Study of cpo resonances on the intercombination line in 173 yb," *Journal of Physics B: Atomic, Molecular and Optical Physics*, vol. 51, no. 3, p. 035502, 2018. [Online]. Available: http://stacks.iop.org/0953-4075/51/i=3/a=035502

[144] M. Mrozek, A. M. Wojciechowski, D. S. Rudnicki, J. Zachorowski, P. Kehayias, D. Budker, and W. Gawlik, "Coherent population oscillations with nitrogen-vacancy color centers in diamond," *Phys. Rev. B*, vol. 94, p. 035204, Jul 2016. [Online]. Available: https://link.aps.org/doi/10.1103/PhysRevB.94.035204

[145] B. C. Das, D. Bhattacharyya, A. Das, S. Chakrabarti, and S. De, "Simultaneous observations of electromagnetically induced transparency (EIT) and absorption (EIA) in a multi-level V-type system of ^{87}Rb and theoretical simulation of the observed spectra using a multi-mode approach," *The Journal of Chemical Physics*, vol. 145, no. 22, p. 224312, 2016. [Online]. Available: https://doi.org/10.1063/1.4971241

[146] C. R. Higgins and I. G. Hughes, "Electromagnetically induced transparency in a v-system with 87rb vapour in the hyperfine paschen-back regime," *Journal of Physics B: Atomic, Molecular and Optical Physics*, vol. 54, no. 16, p. 165403, sep 2021. [Online]. Available: https://dx.doi.org/10.1088/1361-6455/ac20be

[147] F. Silva, J. Mompart, V. Ahufinger, and R. Corbalán, "Electromagnetically induced transparency with a standing-wave drive in the frequency up-conversion regime," *Phys. Rev. A*, vol. 64, p. 033802, Aug 2001. [Online]. Available: https://link.aps.org/doi/10.1103/PhysRevA.64.033802

[148] D. J. Whiting, E. Bimbard, J. Keaveney, M. A. Zentile, C. S. Adams, and I. G. Hughes, "Electromagnetically induced absorption in a nondegenerate three-level ladder system," *Opt. Lett.*, vol. 40, no. 18, pp. 4289–4292, Sep 2015. [Online]. Available: http://opg.optica.org/ol/abstract.cfm?URI=ol-40-18-4289

[149] S. A. Babin, D. V. Churkin, E. V. Podivilov, V. V. Potapov, and D. A. Shapiro, "Splitting of the peak of electromagnetically induced transparency by the higher-order spatial harmonics of the atomic coherence," *Phys. Rev. A*, vol. 67, p. 043808, Apr 2003. [Online]. Available: http://link.aps.org/doi/10.1103/PhysRevA.67.043808

[150] C. E. Theodosiou, "Lifetimes of alkali-metal—atom rydberg states," *Phys. Rev. A*, vol. 30, pp. 2881–2909, Dec 1984. [Online]. Available: https://link.aps.org/doi/10.1103/PhysRevA.30.2881

[151] E. O. Nyakang'o, D. Shylla, V. Natarajan, and K. Pandey, "Hyperfine measurement of the 6p1/2 state in 87rb using double resonance on blue and IR transition," *Journal of Physics B: Atomic, Molecular and*

Optical Physics, vol. 53, no. 9, p. 095001, mar 2020. [Online]. Available: https://doi.org/10.1088%2F1361-6455%2Fab7670

[152] Nyakang´o, Elijah Ogaro, Shylla, Dangka, Indumathi, Kirthanaa, and Pandey, Kanhaiya, "Nature of interference between autler-townes peaks in generic multi-level system," *Eur. Phys. J. D*, vol. 74, no. 9, p. 187, 2020. [Online]. Available: https://doi.org/10.1140/epjd/e2020-10187-3

[153] D. Das and V. Natarajan, "Hyperfine spectroscopy on the 6 p 3/2 state of 133 cs using coherent control," *EPL (Europhysics Letters)*, vol. 72, no. 5, p. 740, 2005. [Online]. Available: http://stacks.iop.org/0295-5075/72/i=5/a=740

[154] S. Menon and G. S. Agarwal, "Gain components in the autler-townes doublet from quantum interferences in decay channels," *Phys. Rev. A*, vol. 61, p. 013807, Dec 1999. [Online]. Available: https://link.aps.org/doi/10.1103/PhysRevA.61.013807

[155] M. S. Feld, M. M. Burns, T. U. Kühl, P. G. Pappas, and D. E. Murnick, "Laser-saturation spectroscopy with optical pumping," *Opt. Lett.*, vol. 5, no. 2, pp. 79–81, Feb 1980. [Online]. Available: http://ol.osa.org/abstract.cfm?URI=ol-5-2-79

[156] D. A. Smith and I. G. Hughes, "The role of hyperfine pumping in multilevel systems exhibiting saturated absorption," *American Journal of Physics*, vol. 72, no. 5, pp. 631–637, 2004. [Online]. Available: https://doi.org/10.1119/1.1652039

[157] H. R. Noh, "Effect of optical pumping in saturated absorption spectroscopy: an analytic study for two-level atoms," *European Journal of Physics*, vol. 30, no. 5, p. 1181, 2009. [Online]. Available: http://stacks.iop.org/0143-0807/30/i=5/a=025

[158] Y.-q. Li and M. Xiao, "Observation of quantum interference between dressed states in an electromagnetically induced transparency," *Phys. Rev. A*, vol. 51, pp. 4959–4962, Jun 1995. [Online]. Available: https://link.aps.org/doi/10.1103/PhysRevA.51.4959

[159] D. J. Fulton, S. Shepherd, R. R. Moseley, B. D. Sinclair, and M. H. Dunn, "Continuous-wave electromagnetically induced transparency: A comparison of v, Λ, and cascade systems," *Phys. Rev. A*, vol. 52, pp. 2302–2311, Sep 1995. [Online]. Available: https://link.aps.org/doi/10.1103/PhysRevA.52.2302

[160] V. B. Tiwari, S. Singh, H. S. Rawat, M. P. Singh, and S. C. Mehendale, "Electromagnetically induced transparency in cold85rb atoms trapped in the ground hyperfineF= 2 state," *Journal of Physics B: Atomic, Molecular and Optical Physics*, vol. 43, no. 9, p. 095503, apr 2010. [Online]. Available: https://doi.org/10.1088%2F0953-4075%2F43%2F9%2F095503

[161] R. W. Boyd, M. G. Raymer, P. Narum, and D. J. Harter, "Four-wave parametric interactions in a strongly driven two-level system," *Phys. Rev. A*, vol. 24, pp. 411–423, Jul 1981. [Online]. Available: https://link.aps.org/doi/10.1103/PhysRevA.24.411